

AD_____

Award Number: W81XWH-04-1-0446

TITLE: Comparison of the Specificity of MREIT and Dynamic Contrast-Enhanced MRI in Breast Cancer

PRINCIPAL INVESTIGATOR: Ozlem Birgul, Ph.D.

CONTRACTING ORGANIZATION: University of California, Irvine
Irvine, CA 92697-7600

REPORT DATE: May 2007

TYPE OF REPORT: Final

PREPARED FOR: U.S. Army Medical Research and Materiel Command
Fort Detrick, Maryland 21702-5012

DISTRIBUTION STATEMENT: Approved for Public Release;
Distribution Unlimited

The views, opinions and/or findings contained in this report are those of the author(s) and should not be construed as an official Department of the Army position, policy or decision unless so designated by other documentation.

REPORT DOCUMENTATION PAGE				Form Approved OMB No. 0704-0188	
Public reporting burden for this collection of information is estimated to average 1 hour per response, including the time for reviewing instructions, searching existing data sources, gathering and maintaining the data needed, and completing and reviewing this collection of information. Send comments regarding this burden estimate or any other aspect of this collection of information, including suggestions for reducing this burden to Department of Defense, Washington Headquarters Services, Directorate for Information Operations and Reports (0704-0188), 1215 Jefferson Davis Highway, Suite 1204, Arlington, VA 22202-4302. Respondents should be aware that notwithstanding any other provision of law, no person shall be subject to any penalty for failing to comply with a collection of information if it does not display a currently valid OMB control number. PLEASE DO NOT RETURN YOUR FORM TO THE ABOVE ADDRESS.					
1. REPORT DATE (DD-MM-YYYY) 01-05-2007		2. REPORT TYPE Final		3. DATES COVERED (From - To) 16 Apr 2004 – 15 Apr 2007	
4. TITLE AND SUBTITLE Comparison of the Specificity of MREIT and Dynamic Contrast-Enhanced MRI in Breast Cancer				5a. CONTRACT NUMBER	
				5b. GRANT NUMBER W81XWH-04-1-0446	
				5c. PROGRAM ELEMENT NUMBER	
6. AUTHOR(S) Ozlem Birgul, Ph.D. E-Mail: obirgul@uci.edu				5d. PROJECT NUMBER	
				5e. TASK NUMBER	
				5f. WORK UNIT NUMBER	
7. PERFORMING ORGANIZATION NAME(S) AND ADDRESS(ES) University of California, Irvine Irvine, CA 92697-7600				8. PERFORMING ORGANIZATION REPORT NUMBER	
9. SPONSORING / MONITORING AGENCY NAME(S) AND ADDRESS(ES) U.S. Army Medical Research and Materiel Command Fort Detrick, Maryland 21702-5012				10. SPONSOR/MONITOR'S ACRONYM(S)	
				11. SPONSOR/MONITOR'S REPORT NUMBER(S)	
12. DISTRIBUTION / AVAILABILITY STATEMENT Approved for Public Release; Distribution Unlimited					
13. SUPPLEMENTARY NOTES					
14. ABSTRACT It is possible to detect locations of lesions accurately in breast cancer using techniques such as x-ray mammogram accurately; however, the specificity of current techniques is low. Since the conductivity values of malignant, benign, and normal tissues are significantly different, this information can be used in classification. Current conductivity imaging techniques can only provide low-resolution images and fail in extreme cases. Magnetic resonance-electrical impedance tomography (MREIT) is a new modality that can reconstruct high-resolution conductivity images. In this study, we propose the use of MREIT for improving accuracy of breast cancer classification. In this project, MREIT system for 3D data acquisition was implemented. Mesh generation and image reconstruction algorithms in 3D were developed. 3D phantom studies were carried out successfully. Preliminary animal experiments that demonstrate conductivity contrast for R3230 tumor models were carried out. Data acquisition system was generalized for imaging at different field strengths. Preliminary images were acquired using fast imaging sequences that is crucial in in vivo imaging. During this period, PI acquired training in tumor biology and different imaging modalities in tumor imaging.					
15. SUBJECT TERMS electrical impedance tomography (EIT), dynamic contrast-enhanced magnetic resonance imaging (DCE-MRI), breast cancer					
16. SECURITY CLASSIFICATION OF:			17. LIMITATION OF ABSTRACT	18. NUMBER OF PAGES	19a. NAME OF RESPONSIBLE PERSON
a. REPORT	b. ABSTRACT	c. THIS PAGE			USAMRMC
U	U	U	UU	81	19b. TELEPHONE NUMBER (include area code)

Table of Contents

Introduction.....	4
Body.....	5
Reportable Outcomes.....	22
Key Research Accomplishments.....	24
Conclusions.....	24
Appendices.....	25

INTRODUCTION

Background

Breast cancer is the leading cause of cancer deaths among women in many parts of the world and currently no single imaging modality has both high sensitivity and specificity for breast cancer. Although x-ray mammography, the current gold standard for breast imaging, has high sensitivity, false-positive mammograms have a substantial cumulative risk. New imaging modalities with better specificity will reduce these risks.

Electrical properties of malignant tissues are significantly different from the properties of normal and benign tissues. It has been reported that the electrical impedance of malignant tumors decreases by a factor of 20 to 40 with respect to the normal or benign tissue [1]. Therefore, electrical conductivity information, which is inversely related to impedance, may be used in tumor detection and characterization. At the present time, well-established breast screening methods have high sensitivity but suffer from poor specificity. Specifically, x-ray mammography, which is accepted as gold standard for breast cancer screening, provides high sensitivity but has a high rate of false-positives [2-4]. Similarly, although the sensitivity of breast MRI has been extremely high, the specificity for the detection of abnormalities is variable [5, 6]. In addition, these techniques fail to detect the breast cancer in some cases, such as dense breast tissue, which is common among younger patients, and patients undergoing hormone replacement therapy during post-menopausal period [7]. Accurate measurements of conductivity can be used to detect tumors and achieve higher specificity rates compared to the currently used techniques.

Electrical Impedance Tomography (EIT) has been developed in 1980s to reconstruct the conductivity distribution inside a volume conductor. In this method, a current distribution inside the object is generated by injection or induction and peripheral voltage measurements are acquired to find the internal conductivity distribution [8]. Although it is widely used for dynamic imaging, it has been reported that the technique has potential application in breast cancer detection [9].

Electrical Impedance Spectroscopy (EIS) is a similar technique developed to diagnose malignant breast tumors [10-14]. There is an FDA approved device that employs this technique [15]. However, conductivity images reconstructed using this technique are of low spatial resolution and are insensitive to cases where tumor is located 3-3.5cm away from the surface or just under the nipple. Moreover, the spatial resolution is not uniform throughout the imaging region.

MREIT is a recently developed method for conductivity imaging [16-21]. It uses the magnetic flux density measurements acquired from MR phase images in conductivity reconstruction. Magnetic flux density generated due to applied currents can be measured with high and space independent spatial resolution using MRI for DC [22], AC [23, 24] and RF [25] currents. Note that, only the component of the magnetic flux density in the direction of the main field of the MRI system can be measured. Then, the inverse problem of finding conductivity or current density from magnetic flux density can be solved. Only relative conductivity values can be reconstructed if the magnetic flux density measurements are used alone. In order to find the absolute conductivity values, at least one voltage measurement from the boundary is required. The reconstruction algorithms can also be divided into two groups depending on the data type required. First group uses magnetic flux density directly whereas in second one, current density distribution is required in the image reconstruction. Algorithms that uses current density distribution requires the measurement of all three components of the magnetic flux density, thus, rotation of the object inside the magnet is required.

BODY

In this multidisciplinary post-doctoral training grant, five specific aims were proposed.

Aim 1. Training stage: In order to be able to carry out the study proposed, principal investigator will receive training in tumor biology and DCE-MRI.

Aim 2. Development of 3D reconstruction algorithms for MREIT: In parallel with the training stage, new studies to improve the MREIT images will be carried out.

Aim 3. Test of 3D reconstruction using phantoms: Phantom experiments will be carried out for the 3D case.

Aim 4. Performing animal experiments using both techniques: Comparative animal experiments using ENU (N-Ethyl-N-Nitrosourea) induced malignant and benign breast tumors in rats will be carried out.

Aim 5. Statistical analysis: Efficacy of MREIT and comparison with DCE-MRI will be evaluated by ROC analysis of the acquired data and results from the pathological examination.

Statement of Work

The tasks to achieve the specific aims listed above are covered in the statement of work as outlined below.

Task 1. Acquire the necessary training in tumor biology and dynamic contrast-enhanced magnetic resonance imaging (Months 0-24)

- a) Auditing courses and attending seminars on tumor biology (Months 0-12).
- b) Training in DCE-MRI and preparation of animals for the training experiments (Months 13-16).
- c) Experimental training in DCE-MRI (Months 17-21).
- d) Statistical analysis of DCE-MRI data (Months 22-24).

Task 2. Implement a 3D-reconstruction algorithm for MREIT and test with simulations (Months 0-18).

- a) 3D Mesh generation from MR slice images (Months 0-2).
- b) Implementation of 3D FEM algorithm for arbitrary meshes (Months 3-6).
- c) Implementation of the reconstruction algorithms and testing with simulation data (Months 6-10).
- d) Incorporation of a priori anatomical information in image reconstruction (Months 11-12).
- e) Determination of optimal electrode locations for arbitrary meshes (Months 13-14).
- f) Making necessary updates in the algorithm (if necessary) by assessing the performance with the preliminary experimental results (Months 15-18).

Task 3. Modify existing hardware and pulse-sequences and test 3D reconstruction with phantoms and animals (Months 13-24).

- a) Construction of 3D conductivity phantoms (Month 13).
- b) Modifying and testing the pulse sequence for multi-slice imaging (Months 14-15).
- c) Testing the system and adjusting the imaging parameters using phantoms (16-18).
- d) Carrying out animal experiments using MREIT to determine the optimal parameters and electrode locations (Months 19-24).

Task 4. Perform animal experiments using both techniques.

- a) Carrying out experiments on 50 ENU induced rats using both techniques for hypothesis testing. (Months 25-32).

Task 5. Receiver Operating Characteristics (ROC) analysis.

- a) Analysis of MREIT and DCE-MRI data (Months 25-32).
- b) Comparison with pathology results and ROC analysis (32-36).

Task 1 Training in tumor biology and dynamic contrast-enhanced magnetic resonance imaging

As stated in the description of the research training section of the proposal, the principal investigator attended a basic cancer biology course (UCI, BioSci 125 Molecular Biology of Cancer) offered by her co-mentor Dr. Eva Lee.

For training in tumor biology and applications of different imaging modalities in breast cancer imaging, the principal investigator attended several seminars. One of the comments in the peer review panel summary was the lack of expansion of the training in tumor biology in other imaging modalities. This comment was taken into account in the selection of seminars attended. The detailed list of seminars were given in previous reports.

Experimentation and analysis methods in dynamic contrast enhanced-magnetic resonance imaging (DCE-MRI) were also part of the training in the second year of the award. Principal investigator acquired training in data acquisition (adjustment of dynamic pulse sequences, synchronization with contrast agent injection) and performed experiments herself.

Task 2. Implementation a 3D-reconstruction algorithm for MREIT and test with simulations

Forward Problem Formulation

Calculation of surface potential values and inner magnetic flux density distribution for a known conductivity distribution and boundary conditions is called the *forward problem* of MREIT. The relation between conductivity and potential distributions in the object is given by the Laplace's equation,

$$\nabla(\sigma(x, y, z)\nabla\phi(x, y, z)) = 0 \quad (x, y, z) \in V$$

where $\sigma(x, y, z)$ is electrical conductivity distribution, $\phi(x, y, z)$ is the electrical potential distribution and V is the domain representing the object to be imaged. For the case of current injected on the surface via two current electrodes Neumann boundary condition holds, which is,

$$\sigma(x, y, z)\frac{\partial\phi(x, y, z)}{\partial n} = \begin{cases} j & \text{positive electrode} \\ -j & \text{negative electrode} \\ 0 & \text{elsewhere} \end{cases}$$

where j is the magnitude of the applied current and $\partial\phi/\partial n$ is the change in electrical potential in the direction of the outward normal. In order to calculate the magnetic flux density distribution, $\vec{B}(x, y, z)$ inside the object, current density distribution, $\vec{J}(x, y, z)$ must be calculated first. Since the conductivity is assumed to be known in the forward problem, electric field intensity distribution, $\vec{E}(x, y, z)$, and the corresponding $\vec{J}(x, y, z)$ are found using

$$\vec{E}(x, y, z) = -\nabla\phi(x, y, z) \text{ and } \vec{J}(x, y, z) = \sigma(x, y, z)\vec{E}(x, y, z)$$

Finally, $\vec{B}(x, y, z)$ is calculated using the Biot-Savart relation:

$$\vec{B}(x, y, z) = \frac{\mu_0}{4\pi} \int \frac{\vec{J}(x, y) dV \times \hat{a}_R}{R^2}$$

where $\vec{B}(x, y, z)$ is the magnetic flux density at measurement points, μ_0 is the permeability of free space, R is the distance between source and field points, and \hat{a}_R is the unit vector pointing from source, (x', y', z') , to the field point, (x, y, z) . Only the z -component of the magnetic flux density is measured using MRI and is used in image reconstruction and it is given by

$$B_z(x, y, z) = \frac{\mu_0}{4\pi} \int \frac{J_x(x', y', z')(y - y') - J_y(x', y', z')(x - x')}{R^3} dV$$

Note that only x and y components of the current will create a magnetic field in the z -direction and therefore are required in the formulation.

For most irregular geometries and complex conductivity distributions, it is not possible to solve above equations analytically. Finite element method (FEM) is used to solve the boundary value problem defined. [26]. First order elements are used to discretize the imaging volume, V . Each element is assumed to have uniform conductivity, and potential distribution in each element is approximated to vary linearly within the element. Consequently, electric field and current density inside each element are constant. In the calculation of magnetic flux density from current density using the Biot-Savart relation, each finite element is taken to act as a current source located at its center of gravity, and the measurement points are also selected as the elements centers. Although magnetic flux values are calculated at element centers, practically magnetic flux density is measured on a rectangular grid, therefore, an interpolation is required before reconstruction.

Mesh Generation

The accuracy of the image reconstruction algorithms highly depends on the quality of the match between the true physical properties and the corresponding model. Earlier attempts for using exact boundary information in reconstruction included some transformations from simple geometries that were still coarse approximations. Another approach is to force the structure into a more regular shape, such as placing a rat in a cylinder or compress breast between plates, in which the anatomical structures shift from their true locations. In cases where multi-slice anatomical images are available, it is possible to generate true geometry from these images.

In MREIT, although we only use the phase maps acquired during current injection for conductivity imaging, it is possible to record a set of high-resolution anatomical images and use this information for geometry formation. Another advantage is that the subject is kept exactly in the same position during both experiments therefore movement errors are minimum. High-resolution anatomical images are used not only for geometry extraction but also for the determination of exact boundary conditions using MR visible markers.

In Figure 1, a set of rat MR images with markers is given. First, the boundary points (dotted red line) are manually selected for the first slice. The number of points in all slices is kept constant and determined by shifting the locations from the previous slice. After the boundary points for each slice are determined, they are coupled through slices and using the loft function of FEMLAB, the 3D geometry in Figure 2a is formed. The important step in geometry formation is the selection of appropriate weights and coupling of edges in each slice so that a valid geometry can be formed. Once the geometry is defined, a finite element mesh with tetrahedral elements is generated as shown in Figure 2b.

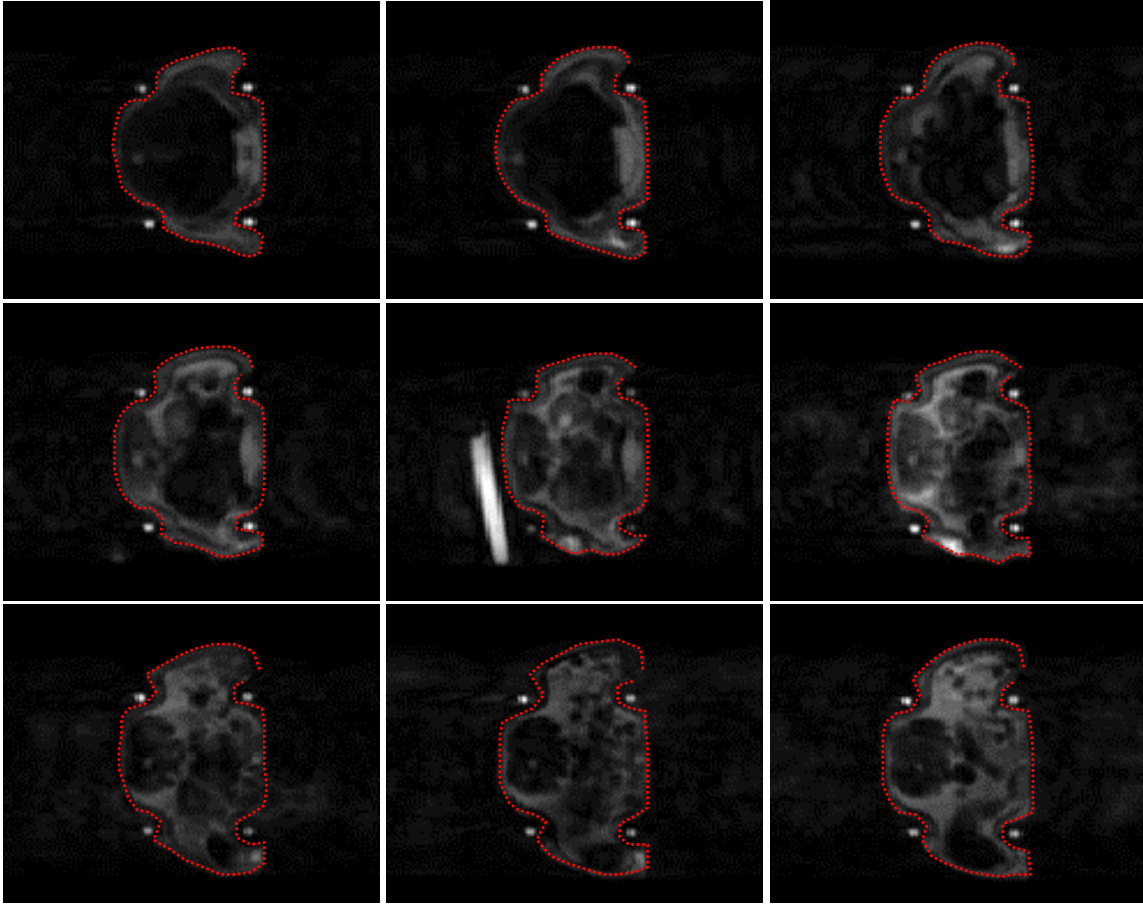


Figure 1. Multi-slice anatomical MR images and boundary points selected to generated the 3D geometry

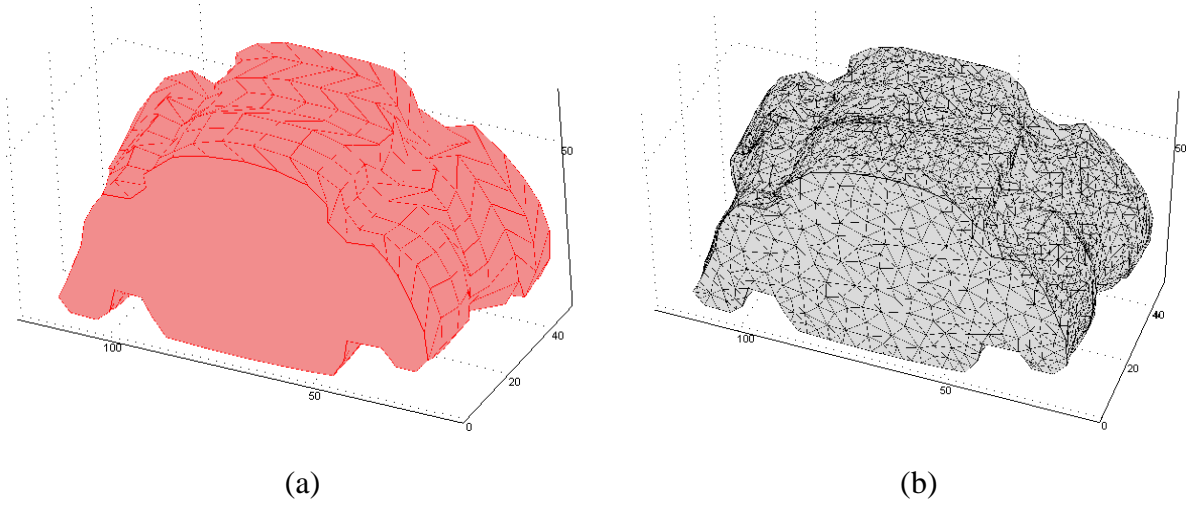


Figure 2. (a) 3D geometry formed using boundary points defined in Figure 1. (b) Corresponding finite element mesh with 24617 tetrahedrons.

After the formation of the 3D geometry and the corresponding finite element mesh, next step is the solution of the forward problem using the method explained in the formulation section. In Figure 3a, the simulated electrical potential distribution for a pair of electrodes placed oppositely on top left and bottom right of the geometry is given. As expected, a high potential is observed under the positive electrode and a low potential is observed above the negative electrode. In Figure 3b, gradient of potential distribution is seen. Note that due to the negative sign in equation (3), the current flow lines will be in the opposite direction and currents are flowing from positive electrode to the negative electrode.

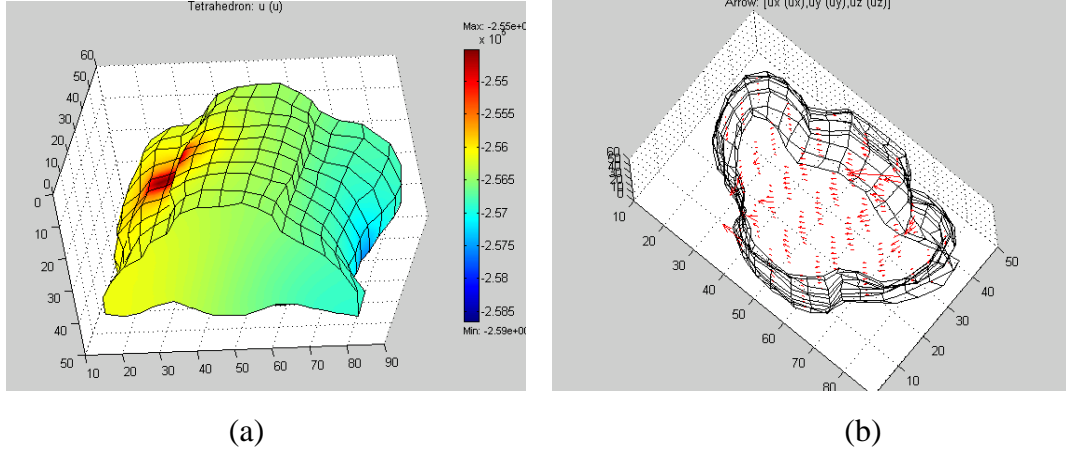


Figure 3. (a) Electric field distribution for a single pair of electrodes. (b) Electrical current density distribution.

Iterated Sensitivity matrix reconstruction using Tikhonov regularization

In the reconstruction process, a uniform conductivity is assumed as the initial distribution and the forward relation between conductivity and magnetic flux density is linearized around this conductivity distribution as explained in detail in Birgul *et.al* [20]. Resulting matrix equation that approximates the relation between conductivity and magnetic flux density perturbations is given by:

$$\Delta \mathbf{b} = \mathbf{S} \Delta \sigma$$

where $\Delta \mathbf{b}$ is the difference between measured magnetic flux density and the magnetic flux density corresponding to initial distribution, $\Delta \sigma$ is the change with respect to initial conductivity distribution and \mathbf{S} is the sensitivity matrix that gives the relation between changes in magnetic flux density and conductivity. The sensitivity matrix is calculated using semi-analytical method [20]. The sensitivity matrix is ill-posed in general and due to noise in the data, some form of regularization is required to be able to solve the system in above equation. Including Tikhonov regularization parameter,

$$(\mathbf{S}^T \mathbf{S} + \lambda \mathbf{I}) \Delta \sigma = \mathbf{S}^T \Delta \mathbf{b}$$

where \mathbf{I} is the identity matrix. In the first two years of this study, to choose the optimum regularization parameter, the matrix equation was solved for different values of λ using the built-in `cgs` function of MATLABTM with default settings (10^{-6} tolerance level, 20 iterations, and no pre-conditioning) and the optimum regularization value is selected as the one minimizing the difference,

$$\min_{\lambda} \sum_{i=1}^m \|B_{meas,i} - B_{calc,i}(\lambda)\|$$

where m is the total number of measurement points, B_{meas} is the measured magnetic flux density, and B_{calc} is the flux density calculated using reconstructed conductivity. We have observed that the regularization parameter chosen with this approach was sometimes not the optimum, especially for the irregular outside boundary cases and we started using the following criteria for the selection of λ

$$\lambda = \text{trace}(\mathbf{S}^T \mathbf{S})/n$$

where trace is the sum of the diagonal elements of the matrix product and n is the dimension of the matrix product. For iterations, calculated conductivity distribution is assigned as the initial value and the steps starting with sensitivity matrix calculation are repeated until the change in conductivity two consecutive iterations are below a defined threshold. The flowchart of the algorithm is given in Figure 4.

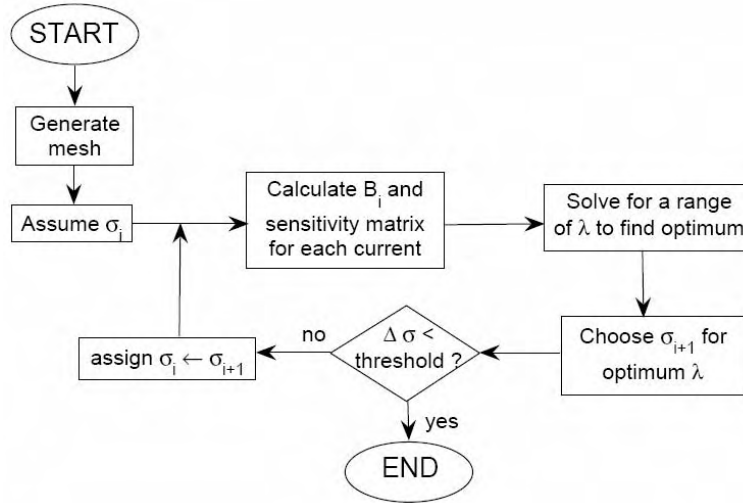


Figure 4. Flowchart of the reconstruction algorithm

Compared to sensitivity based reconstruction algorithms reported before, the major differences of the algorithm used in this study are:

- using conjugate gradient solver (CGS) instead of truncated SVD. This eliminated the requirement of large decomposition matrices, which enables faster and memory efficient reconstruction.
- introducing Tikhonov regularization instead of truncation. This eliminates operator dependence.
- iterating the algorithm to improve accuracy even for large conductivity perturbations.

It is known that only relative conductivity values can be reconstructed using magnetic field measurements alone. Using the non-linear reconstruction outlined above, the conductivity distribution can be found with a scale and peripheral voltage measurements can be used to calculate this scaling factor [20]. In this study, voltages are not measured and only relative conductivity distributions are found.

Effects of Limited Volume Coverage on Accuracy of MREIT

The goal of this study was to investigate the effects of limited volume coverage on the accuracy of conductivity reconstruction in MREIT. Since the currents injected into an object will be distributed in the whole volume, limited volume coverage in data acquisition or reconstruction will impact the accuracy of resulting conductivity maps. On the other hand, the magnitude of current density will decrease rapidly as the distance from the injecting electrodes increases. Moreover, if one is interested in a particular volume of interest (VOI), the magnetic fields generated by currents away from the VOI could be negligible. Therefore, we investigated the decrease in magnitude of current density as the distance from the electrodes increases. We also investigated the contribution of these weaker currents to the magnitude of the magnetic fields generated within the VOI.

We performed several simulation studies to calculate the current density and magnetic fields inside a cylindrical volume ($d = 4.5\text{cm}$ $h = 7\text{cm}$) with uniform conductivity distribution. Two electrodes were placed at 135° and 315° around the central transaxial slice (slice 0). In 3D FEM model 13773 nodes and 73452 of tetrahedral elements were used. Figure 5a shows the magnitude of the transverse current density $(J_x(\mathbf{r})^2 + J_y(\mathbf{r})^2)^{1/2}$ across 15 slices for regions labeled 13-19 in Figure 5b. $b_z(\mathbf{r})$ was calculated for five cases on these 15 transverse planes that were 5mm apart. For each case, the current density only within a transverse slab of various thicknesses was used for $b_z(\mathbf{r})$ calculations as given in Table 1.

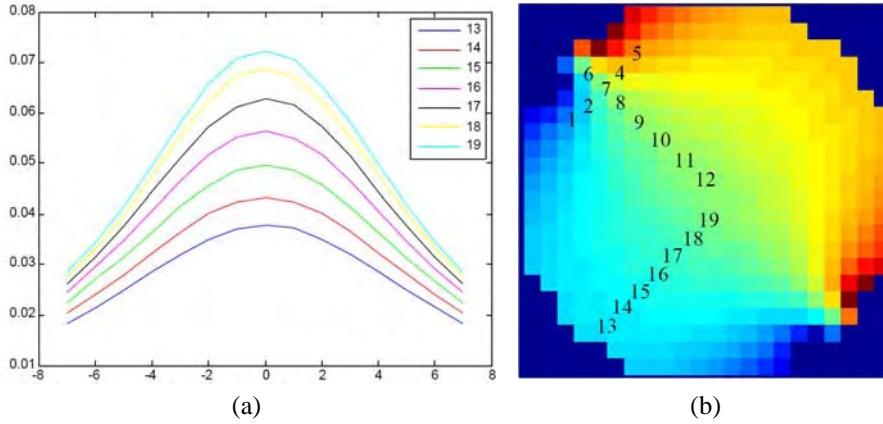


Figure 5. (a) magnitude of current density across slices in selected regions shown in the field map

Table 1. Description of cases.

	Case 1	Case 2	Case 3	Case 4	Case5
Slab thickness	4.2cm	3cm	2.4cm	1.8cm	1.2cm

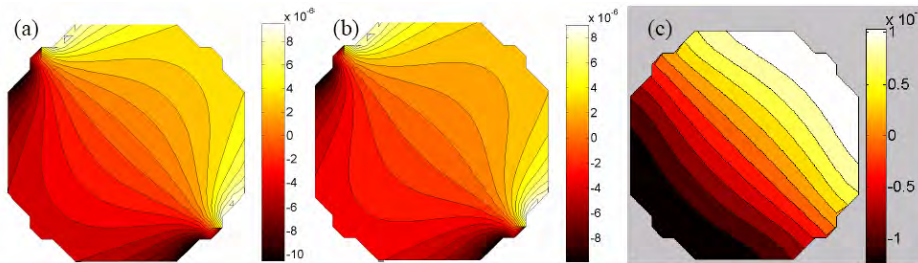


Figure 6. $b_z(\mathbf{r})$ contour maps for case 1 (a), case 5 (b) are illustrated. The difference of the two $b_z(\mathbf{r})$ maps is shown in (c). Current was injected between electrodes placed at 135° and 315° .

Figure 6 shows the $b_z(\mathbf{r})$ contour maps in slice 0. Figure 6a is the resulting magnetic field when the transverse current density in 4.2cm thick slab was used (Case 1). Similarly, Figure 6b is the $b_z(\mathbf{r})$ for Case 5. Figure 6c is the difference field when 6b is subtracted from 6a. When Case 1 is taken as the reference, the field difference maps ($\Delta b_z(\mathbf{r})$) between Case 1 and others give us a measure of the errors made in the calculation of $b_z(\mathbf{r})$ when the current density outside the selected slab is ignored. Therefore, we defined a region of interest (ROI) that encompassed the white contour band in the upper right hand corner of Figure 6. The mean $b_z(\mathbf{r})$ inside the ROI for Case 1 is taken as the reference and the mean of $\Delta b_z(\mathbf{r})$ for each case is calculated and divided by this reference mean. Results are summarized in Table 2.

Table 2. Normalized mean valued with respect to Case 1.

	Case 2	Case 3	Case 4	Case5
$\frac{\text{mean}(\Delta b_z(\mathbf{r}))}{\text{mean}(\text{case1})} \times 100$	4.8	9	17	29

The result in Figure 5 shows that the current density in the plane that is 21mm away from the electrodes has significant magnitude. (e.g. in region 19, the magnitude of the current is roughly 40% of that of slice 0). Moreover, the magnetic field in the ROI in slice 0 is underestimated by almost 30% if only currents within a 12mm slab are taken into account. This will lead to underestimation of conductivity maps in this slice. Therefore, one has to acquire MREIT data that covers sufficiently large volume to obtain accurate conductivity maps. On the other hand, reconstruction of conductivity maps from large data sets may require 18-20 hours of computing time. Therefore, optimum volume coverage has to be found to obtain a balance between acceptable accuracy and computational efficiency by carrying out simulations and experiments. The results presented here were obtained from a uniform conductivity phantom. The results from objects of nonuniform conductivity will be different and models should be developed accordingly to find the optimum volume coverage for studies such as *in vivo* experiments.

Conductivity Maps Reconstructed with Partial B-field Coverage in MREIT

In MREIT, ideally, the whole 3D volume should be imaged and current density and resulting magnetic fields have to be calculated within this whole volume; however, due to the limitations of data acquisition and computationally expensive 3D numerical models for reconstruction, calculations are done within a limited volume, especially for large objects. In previous section, we investigated the effects of calculating current density in a limited volume on the accuracy of conductivity maps. We also investigated the impact of reconstruction of conductivity maps from magnetic fields calculated within a limited slab. If one is interested in a particular VOI, the currents are injected through electrodes placed around the VOI. The current density and resulting magnetic fields will be most dominant inside the VOI and diminish further away. Therefore, one has to find the optimum volume coverage and field calculations to find the best trade-off between accuracy and efficiency. This will complement our previous study where optimum volume coverage for current density calculations were sought, because optimum volume coverage for current density calculations and magnetic field calculations could be different and both will have impact on accuracy differently.

We performed several simulation studies to reconstruct the conductivity maps inside a cylindrical volume ($d=4.5\text{cm}$ $h=4\text{cm}$) with two inserted objects, ($d=1.5\text{cm}$ $h=1.2\text{cm}$ each, one is placed at $z=0$, the other at $z=1.2$). Four electrodes were placed 90° apart, around the central transaxial slice. Same 3D FEM mesh defined in previous section is used. Current density calculation was made inside a transaxial slab that extended from -1.2cm to 1.2 cm. For all cases reported here, the current in all 7 slices were used to calculate $b_z(\mathbf{r})$ so that the variability introduced by changing the current density volume was eliminated;

but various subsets of the $b_z(\mathbf{r})$ were used in reconstruction and its impact on resulting conductivity maps was investigated.

The first row of images in Figure 7 shows the magnitude of the actual conductivity distribution in 6 of the 7 slices within the 24mm slab. Current was injected into the third slice from left. The second row shows the case where only $b_z(\mathbf{r})$ inside three slices was used in conductivity image reconstruction; similarly, the third row is the conductivity map when the fields in all 7 slices were used.

It is observed from the second row of Figure 7 that if the fields inside a limited volume is used, the high conductivity object in the current injection slice becomes dominant and replicates itself in all surrounding slices and the second object (seen in slices 5 and 6 in the top row) becomes almost completely invisible. When magnetic fields inside a larger volume are used in reconstruction, both objects reconstruct reasonably well. Although we used the current density and the magnetic field in only a 24mm portion of the whole volume of 40mm, both high conductivity objects are detected. This has important implications in applications such as tumor imaging with MREIT because one focuses in the tumor area to obtain the conductivity distribution inside the tumor and surrounding tissues, but possible metastasis or multiple tumor foci might be missed if sufficiently large volume is not modeled in reconstruction. Although substantial gain in reconstruction speed will be obtained with limited volume coverage, critical lesions could be missed. Moreover, a lesion might appear larger than it actually is (see Figure 7, row 2). Considering that reconstruction of conductivity maps from data sets of even 10-12 slices may require 18-20 hours of computing time, speed in reconstruction becomes an important issue. Therefore, one has to acquire MREIT data that covers sufficiently large volume to obtain accurate conductivity maps. Moreover, optimum volume coverage used in the numerical model of reconstruction has to be found to obtain a balance between acceptable accuracy and computational efficiency by carrying out simulations and experiments.

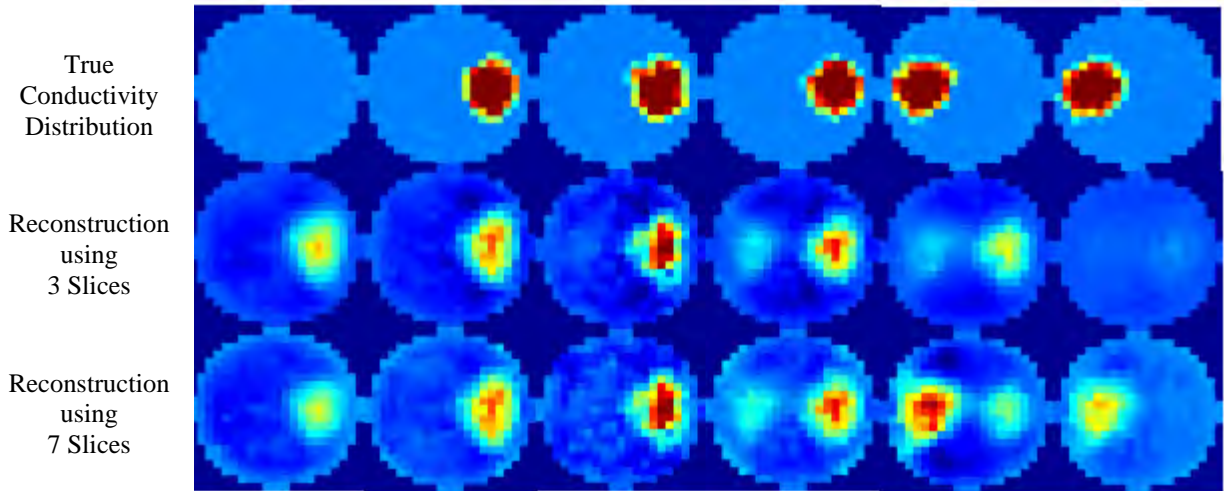


Figure 7. Top row: actual conductivity distribution. One high conductivity object is at 3 o'clock position (slices 2-4) and the other at 9 o'clock position (slices 5-6). 2nd and 3rd rows show the reconstructed map using $b_z(\mathbf{r})$ only in 3 and 7 slices, respectively.

Task 3. Modification of existing hardware and pulse-sequences and test 3D reconstruction with phantoms and animals

In order to be able to measure magnetic flux density at low amplitude currents, we implemented various modifications in our hardware and pulse sequence and carried out various phantom experiments for optimization. In our earlier studies, we were using sine wave current synchronized with the first RF pulse in a conventional spin echo sequence, Figure 8a. In this scheme, the pulse sequence was triggering an external function generator to output a burst sine wave, making it more susceptible to small timing errors. In the new scheme, instead of using sine wave we used a train of pulses, Figure 8b, where pulse sequence directly controls polarity and timing of each pulse sequence, which provides more accurate synchronization. Another modification in the pulse sequence is that no current is applied during RF refocusing pulses. In older sequence, RF pulses were applied during application of the burst sine wave and it was suspected that the small currents during application of RF pulses were leading slight shifts in the slice selection location. We also maintained slice selection gradient for refocusing pulses throughout the current application. This functions as crusher gradient, dephasing unwanted secondary/stimulated echoes generated from multiple RF pulses. Without larger crushers, resulting images exhibited significant interference patterns. Our original sequence collected single slice images only, therefore, we extended the base sequence for multi-slice acquisition for 3D data collection. We tested various echo time, T_E , values and number of cycles of injected current to determine optimum SNR. Optimum T_E is found at T_2 value of imaged object, which is consistent with findings in the literature [22].

In addition to these modifications in the pulse sequence, we also constructed an upgraded current source/multiplexer circuit. In the new current source, selection of the injection profile and pulse polarity is controlled by the pulse sequence, allowing more precise timing and synchronization.

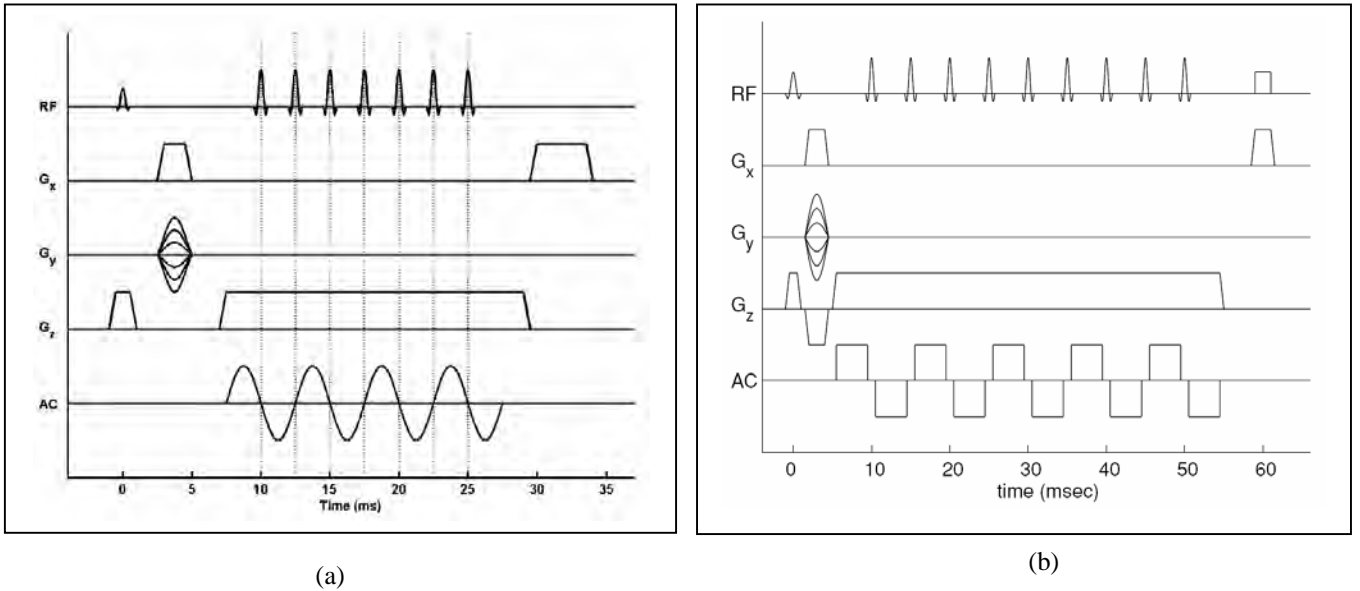


Figure 8. (a) Pulse sequence using AC current (b) Pulse sequence using train of pulses.

3D Reconstruction Example

A 3D phantom was prepared using agarose powder (1gr/100mL) as background and a spherical shell filled with the same agarose gel. Due to insulator shell, the whole sphere acted as a nonconducting object. Four electrodes of size 0.5cm x 0.5cm were placed at the center of the cylinder every 90° as shown in Figure 9. Opposite pairs were used, giving two current injection profiles. A FEM mesh with 2399 nodes and 11781 tetrahedral elements was constructed. The magnetic flux density is calculated at a rectangular grid of 24x24x5, where 2300 of grid points falling into the cylindrical region. A total of 4600 measurements were used in image reconstruction. MR structural images for the 5 slices used are given in Figure 10 (top row). Corresponding reconstructed conductivity images are presented in bottom row, dark region corresponding to insulating object.

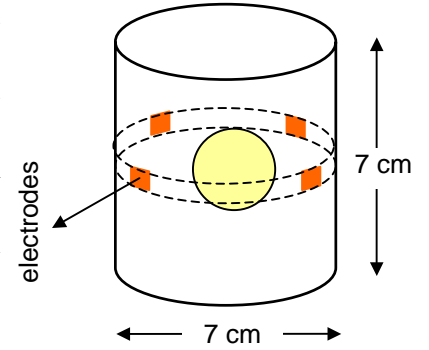


Figure 9. Phantom Description

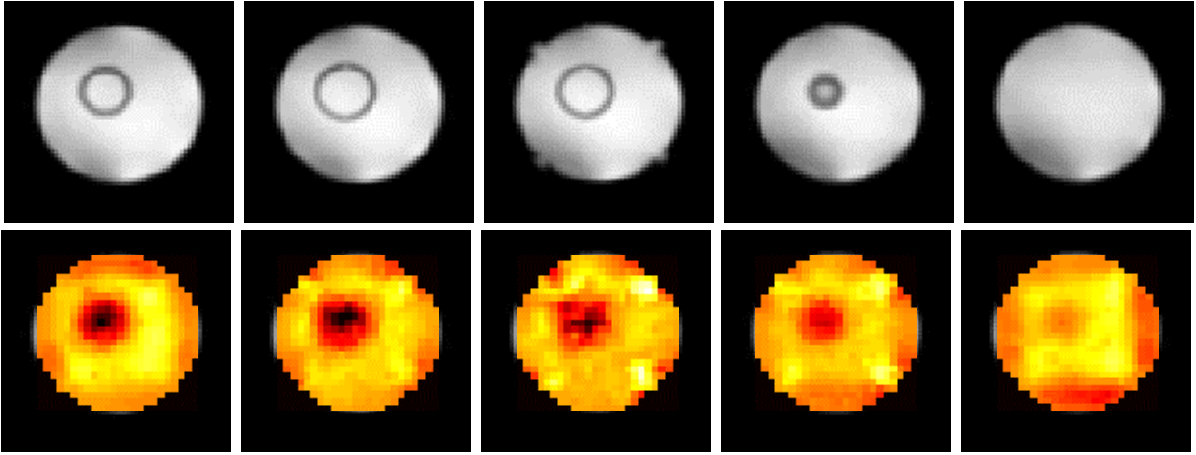


Figure 10. MR anatomical images (top row) and corresponding reconstructed conductivity images (bottom row)

With this study, we demonstrated the feasibility of using 3D sensitivity matrix reconstruction in multi-slice magnetic resonance electrical impedance imaging. Although sensitivity matrix based reconstruction methods are computationally expensive, they perform well in the presence of noise. Previously, we used sensitivity matrix based reconstruction using 2D FEM. That approach ignores the contributions of currents in off-center slices leading to various artifacts in the conductivity images; conductivity values in the reconstructed slice could be under or overestimated, spatial resolution and point spread function could be compromised. In some cases the ‘ghosts’ of objects in other slices may even appear in the reconstructed slice depending on how the conductivity and resulting 3D current density is distributed in the object.

4T versus 7T Experiments

The magnetic flux density is extracted from MRI phase images and one of the challenges in MREIT is acquiring phase information with sufficient SNR while maintaining the injected currents at safe levels. Sadleir et. al. carried out noise analysis in magnetic flux density measurements at 3T and 11T and they suggest that the noise level in magnetic flux density is reduced as field strength is increased by a factor approximately proportional to the increase in the field strength [27]. We carried out experiments at 4T and 7T field strengths to compare the effect of increased magnetic flux density SNR in the final reconstructed conductivity images.

MREIT experiments were carried out using two phantoms with the same distribution in 4T and 7T systems. Since ion diffusion alters the initial conductivity distribution [28], we prepared the phantom immediately before each experiment to minimize these effects in the comparison. The pulse sequence parameters for both experiments were as: TR = 500ms, TE = 60ms FOV = 7cm, slice thickness = 2mm, field image matrix = 64x64, NEX = 4. The sampling bandwidth was set to 33.3KHz and 1.25MHz for 4T and 7T systems, respectively. The amplitude of the injected current was 1mA and the duration of the positive and negative cycles were 27.3ms and 27.7ms. Reconstructed conductivity images and profiles along p-line (as defined in Figure 11) at both field strengths are given in Figure 12. Although the phantom is slightly rotated between two cases, this does not affect the relative positions of the objects with respect to each other. We calculated full-width-at-half-maximum (FWHM) for both objects through x and y cross-sections and also we looked at peak contrast in the object. Note that the SMM reconstructs relative conductivity values if magnetic flux density measurements are used alone and the values presented here are normalized to the background conductivity. The peak reconstructed contrast and FWHM values are summarized in Table 3 for both field strengths and objects. The objects were not fully resolved in the p-line profile for 4T case but more separable in the 7T case. For all cases, the constructed contrasts are lower than the expected ones, especially for the object located at the center.

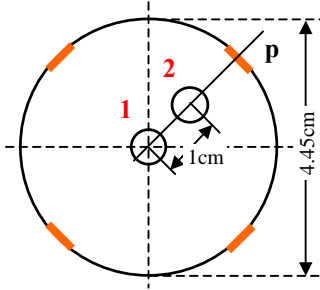


Figure 11. Phantom definitions

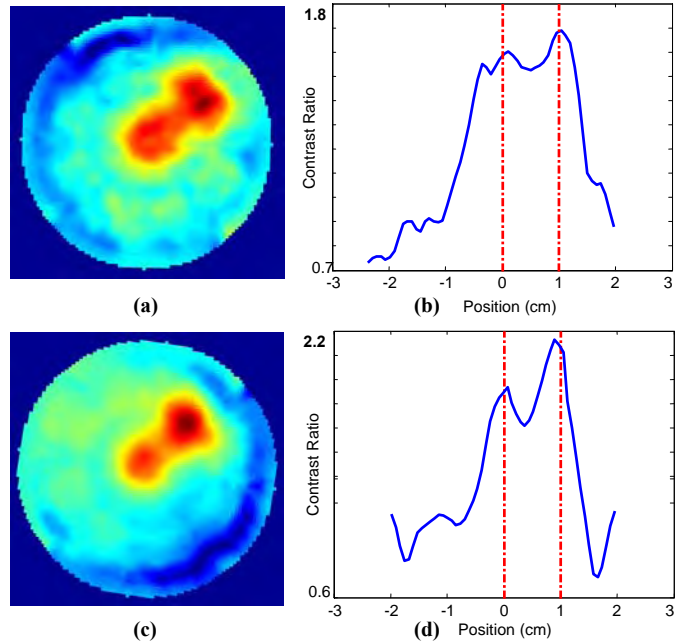


Figure 12. (a) image at 4T (b) 4T profile (along p-line) (c) image at 7T (d) 7T profile (along p-line)

Table 3. Comparison of reconstructed peak contrast and FWHM

	peak contrast		FWHM-x (cm)		FWHM-y (cm)	
	O1	O2	O1	O2	O1	O2
True	3.3	3.3	0.6	0.6	0.6	0.6
4T	1.6	1.8	1.3	1.0	1.4	0.9
7T	1.8	2.2	1.0	0.8	1.1	0.8

When the reconstructed images are compared, it is seen that given the same amount of experimentation time, the accuracy and the spatial resolution of the conductivity images at 7T is better compared to 4T. Although the reconstructed contrast values are lower than the expected values due to ion diffusion in all cases, the comparison between different field strengths shows 13%-22% improvement at 7T compared to the 4T case.

Tasks 4 & 5 Animal experiments and ROC analysis

Preliminary Animal Experiments

After testing our new system with phantom studies, we performed experiments using tumor bearing rats. These tumors were either induced by the carcinogen ENU or R3230 AC tumor grafts. Before starting the animal experiments for hypothesis testing, we scanned 14 animals in order to setup the system and define imaging parameters. Since R3230 tumors take a couple of weeks to grow, we preferred that line line in development stage instead of ENU line, which is expected to grow in 3-4 months. For animal imaging, a special animal holder was prepared from acrylic sheets. In this holder electrodes were placed on acrylic hollow tubes filled with $CuSO_4$ solution mark the electrode positions precisely in the images. The precise localization of electrode positions is critical for accurate assignment of boundary conditions and thus, effects the reconstruction performance. Current carrying wires ran along these tubes, which were in z-direction. This is essential to minimize interference from the magnetic fields generated by current in the wires. The animal was anesthetized by injection of ketamine and xylazine and placed inside the holder. The skin areas of contact were shaved to guarantee good contact. An anatomical image was collected using FSE sequence prior to the MREIT images. A single slice with 6mm thickness was collected from the same anatomical location as the MREIT image. The data matrix was 256×256 , FOV = 10cm, $T_R = 4\text{sec}$, $T_E = 40\text{msec}$, and NEX = 4 (signal averages). MREIT images were collected using the pulse sequence in Figure 9a with $T_R = 500\text{ms}$, $T_E = 30\text{msec}$, NEX = 8, 64×64 data matrix, field of view, FOV = 10cm, 6mm slice thickness, with an AC current of 1mA peak, 100Hz and 4 cycles. Reconstructed images from six animals are shown in Figure 13.

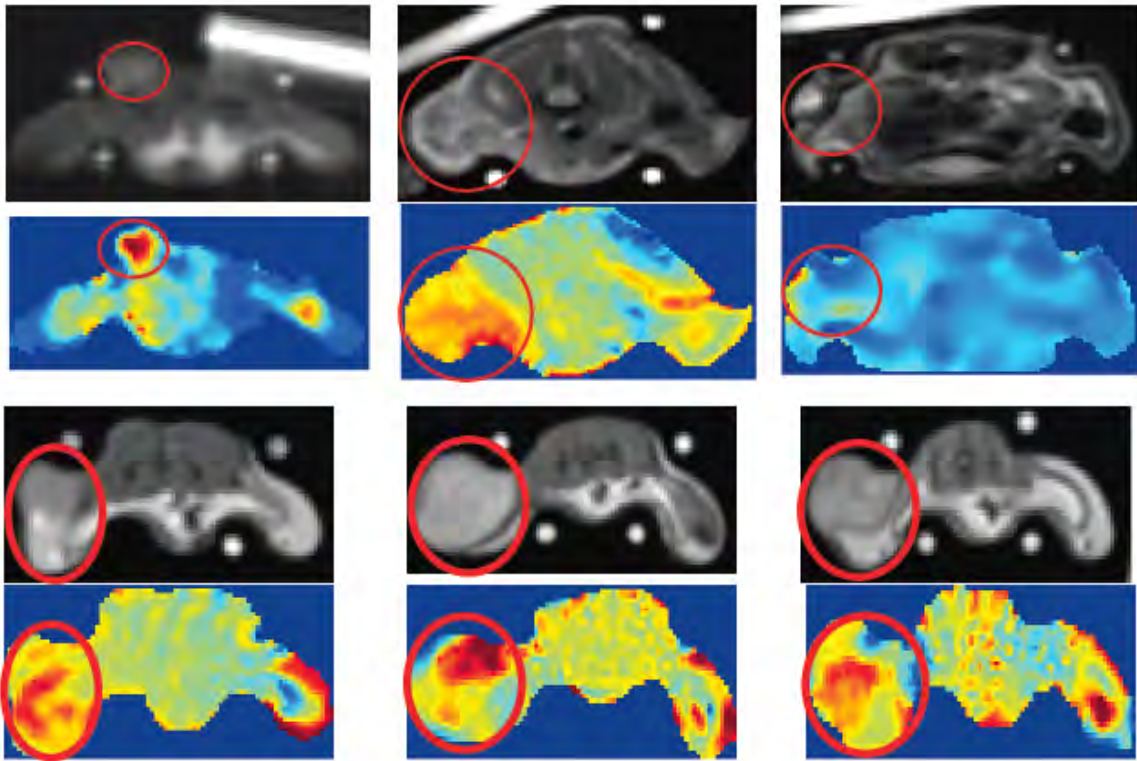


Figure 13. Anatomical MR and corresponding conductivity images for six different animals.

In each image pair, top image shows the anatomical MR image and bottom image shows the corresponding conductivity image. Circled areas show the tumor location. For each animal, region of interests were selected over the tumor region and over the rest of the body. Since these images provide only relative conductivity measures, the ratio of mean conductivity in the tumor divided by the mean conductivity in normal tissue was calculated for each animal. The mean of these ratios across all animals

was $\mu = 2.26$, $\sigma = 0.62$. In other words, the mean conductivity was, on the average, 2.26 times higher than the conductivity in normal regions.

The major challenge we encountered in animal experiments was the errors in the magnetic flux density measurements due to motion artifacts. The motion artifact in the MR image is clearly seen in top left image pair in Figure 13. For some cases, this effect was worse and the data had to be discarded.

ENU Animal Preparation for Comparative Studies

Due to motion artifact problems we have encountered in animal imaging, there has been some delay in tumor induction in animals for comparative studies. In order to avoid unnecessary animal experiments, we first injected ENU into 15 SD rats i.p. on August 9, 2006. Tumors are usually expected to show up 3~4 months after injection. The first tumor appeared on January 5, 2007. Tumors grew up around upper chest area. In R3230 cases, the tumor location can be controlled and all were in the flank area and therefore imaging was less susceptible to the motion due to breathing. For the ENU cases, however, tumor location cannot be controlled and motion artifacts were elevated. Moreover, air cavities introduced some additional problems and we could not acquire any good magnetic flux density map in the 7 animals that has grown tumors using any of the spin echo sequences given in Figure 8 that yielded successful conductivity distribution. At that stage, since we didn't have a large set of ENU animals where we can choose a subset from that would model our ultimate application of breast cancer imaging better, we concentrated on improving the data acquisition scheme by searching faster imaging alternatives that would reduce the problems rising from motion artifacts. Faster imaging would be beneficial in both our model and in our real application in not only reducing the motion artifacts but also giving the option of using higher number of averaging that would make imaging using lower currents possible. In the next section, the idea and the preliminary results for EPI based image reconstruction for MREIT are presented.

EPI Sequence

As an alternative to the established SE-based pulse sequence, we are now investigating the use of a modified single-shot, spin-echo, echo-planar-imaging (SS-SEPI) pulse sequence for measuring the current-generated magnetic flux density (Figure 14). SS-SEPI acquires data for an entire image in a single scan, and thus has the potential to drastically reduce the total data acquisition time, which will resolve the problems encountered in animal studies.

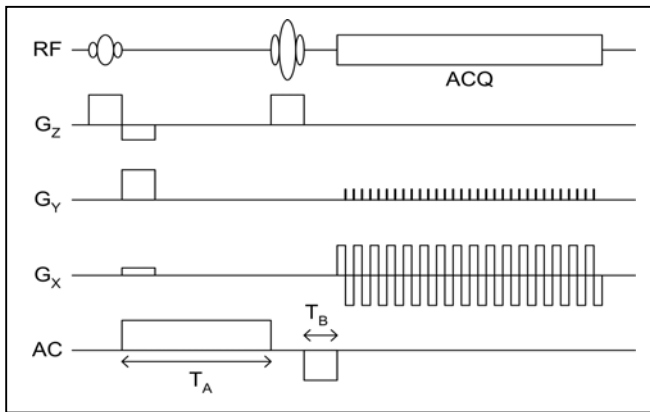


Figure 14. SS-SEPI Pulse Sequence for MREIT

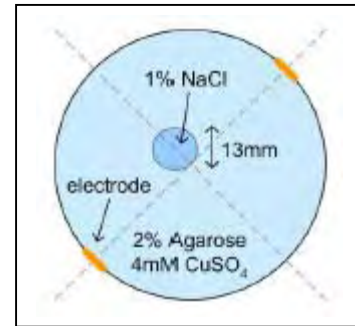


Figure 15. Phantom Description

We tested the sequence using an agar phantom first. For the test phantom, a hollow acrylic disk with an inner diameter of 7cm and thickness of 1cm was filled with 2% agarose and 4mM CuSO₄. Within this disk, a smaller cylindrical region of 13mm diameter was filled with 1% NaCl, 2% agarose, and 4mM CuSO₄ to generate a high conductivity region (Figure 15). The plane of the disk was placed perpendicular to the main static MRI field. Two copper electrodes each 6mm wide were placed opposite of each other

along the inner acrylic wall and used to inject currents into the interior region. A 4mA bipolar current pulse was injected into the phantom and the resulting magnetic flux density distribution measured using a modified SS-SEPI pulse sequence (Figure 14). The component of current-generated magnetic flux density parallel to the main static MRI field (z-component) introduced a phase shift in the MR image given as: $\phi(\mathbf{r}) = \gamma(T_A + T_B)B_Z(\mathbf{r})$. The scan parameters were: $T_A = 35\text{ms}$, $T_B = 10\text{ms}$, $T_R = 3\text{s}$, $T_E = 60\text{ms}$, matrix = 64×64 , FOV = 20cm, and single slice thickness = 5mm. Data was collected twice, each with opposite polarities in the applied current waveform. The resulting phase maps were subtracted then divided by two, so as to cancel out any additional phase contributions, such as those arising from small imperfections in the hardware timing.

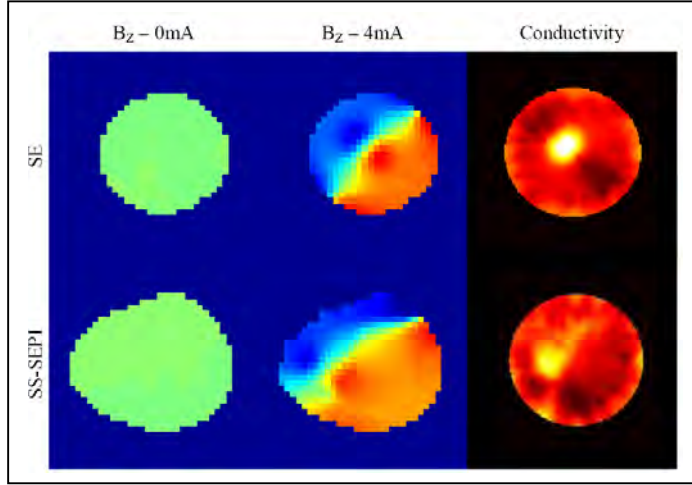


Figure 16. Magnetic flux density and reconstructed conductivity distributions

Relative conductivity maps reconstructed using 5 iterations sensitivity matrix reconstruction are given in Figure 16. Comparison of the 0mA and 4mA cases shows that the SS-SEPI pulse sequence was able to detect the magnetic flux density generated by the injected current. Comparison with the SE results shows that the SS-SEPI pulse sequence was also able to map out the general variation in the magnetic flux density due to the high conductivity perturbation. However, the SS-SEPI images suffer from geometric distortions resulting from the low sampling bandwidth in the phase encode direction inherent in EPI based pulse sequences. As a result, the reconstructed conductivity distribution also suffers from some geometric distortion. Nevertheless, the high conductivity perturbation could still be reconstructed from the SS-SEPI data. We could further improve reconstruction by applying some sort of geometric correction to the MRI data. An advantage of the SS-SEPI pulse sequence is the significant reduction in data acquisition time. A typical imaging experiment takes about 4 minutes when spin echo based pulse sequence was used whereas this reduces to about 12sec when EPI pulse sequence is used. This could allow for increased signal averaging in an allotted study time, which may be required for improving the SNR when using low amplitude injected currents. Single shot pulse sequences are less susceptible to motion artifacts, which will be of significance when applying MREIT to *in vivo* studies.

Although imaging time is considerably shorter for EPI-based sequences, they are prone to geometric distortions caused by inhomogeneity of the main static MRI field. This is due to the extended data acquisition period and corresponding low sampling bandwidth in the phase encode direction. Sources of inhomogeneity include inherent imperfections of the main magnet, perturbations caused by the object to be imaged, and differences in magnetic susceptibility of various regions including the object/air interface. Different correction methods such as higher order shimming, pixel shifting, or partial k-space imaging should be investigated from the standpoint of improving conductivity reconstruction.

References

- [1] A. J. Surowiec, S. S. Stuchly, J. R. Barr, and A. Swarup, "Dielectric Properties of Breast Carcinoma and the Surrounding Tissues," *IEEE Trans. on BME*, vol.35, no. 4, pp. 257- 263, 1988.
- [2] J. G. Elmore, M. B. Barton, V. M. Mocerri, S. Polk, P. J. Arena, and S. W. Fletcher, "Ten-year Risk of False Positive Screening Mammograms and Clinical Breast Examinations," *The New England Journal of Medicine*, vol. 338, no. 16, pp. 1089-1096, 1998.
- [3] C. L. Christiansen, F. Wang, M. B. Barton, W. Kreuter, J. G. Elmore, A. E. Gelfand, and W. Fletcher, "Predicting the Cumulative Risk of False-Positive Mammograms," *Journal of the National Cancer Institute*, vol. 92, no. 20, pp. 1657-1666, 2000.
- [4] J. G. Elmore, D. L. Miglioretti, L. M. Reisch, M. B. Barton, W. Kreuter, C. L. Christiansen, and S. W. Fletcher, "Screening Mammograms by Community Radiologists: Variability in False-Positive Rates," *Journal of the National Cancer Institute*, vol. 94, no. 18, pp. 1373-1380, 2002.
- [5] S. K. Moore, "Better Breast Cancer Detection," *IEEE Spectrum*, vol.38, no.5, pp.50-54, 2001.
- [6] T. A. Coons, "MRI's Role in Assessing and Managing Breast Disease," *Radiological Technology*, vol. 67, no. 4, pp. 311-336, 1996.
- [7] A. Malich, T. Boehm, M. Facius, M. G. Freesmeyer, M. Fleck, R. Anderson, and W. A. Kaiser, "Differentiation of Mammographically Suspicious Lesions: Evaluation of Breast Ultrasound, MRI Mammography and Electrical Impedance Scanning as Adjunctive Technologies in Breast Cancer Detection," *Clinical Radiology*, vol. 56, pp. 278-283, 2001.
- [8] K. Boone, D. Barber, and B. Brown, "Imaging with Electricity: Report of the European Concerted Action on Impedance Tomography," *Journal of Medical Engineering and Technology*, vol. 21, no. 6, pp. 201-232, 1997.
- [9] V. Cherepenin, A. Karpov, A. Korjnevsky, V. Kornienko, A. Mazaletskaya, D. Mazourov, and D Meister, "A 3D Electrical Impedance Tomography (EIT) System for Breast Cancer Detection," *Physiological Measurement*, vol.22, pp. 9-18, 2001.
- [10] J. Estrela da Silva, J. P. Marques de Sá, and J. Jossinet, "Classification of Breast Tissue by Electrical Impedance Spectroscopy," *Medical and Biological Engineering and Computing*, vol. 38, pp. 26-30, 2000.
- [11] A. Malich, T. Fritsch, R. Anderson, T. Boehm, M. G. Freesmeyer, M. Fleck, and W. A. Kaiser, "Electrical Impedance Scanning for Classifying Suspicious Breast Lesions: First Results," *Eur. Radiol.*, vol. 10, pp. 1555-1561, 2000.
- [12] A. Malich, T. Fritsch, C. Mauch, T. Boehm, M. Freesmeyer, M. Fleck, R. Anderson, and W. A. Kaiser, "Electrical impedance scanning: A new technique in the diagnosis of lymph nodes in which malignancy suspected on ultrasound," *The British Journal of Radiology*, vol. 74, pp. 42-47, 2001.
- [13] A. Malich, T. Boehm, M. Facius, M. Freesmeyer, M. Fleck, R. Anderson, and W. A. Kaiser, "Additional value of electrical impedance scanning: experience of 240 histologically-proven breast lesions," *European Journal of Cancer*, vol. 37, pp. 2324-2330, 2001.
- [14] T. E. Kerner, K. D. Paulsen, A. Hartov, S. K. Soho, and S. P. Poplack, "Electrical Impedance Spectroscopy of the Breast: Clinical Imaging Results in 26 Subjects," *IEEE Trans. on Medical Imaging*, vol. 21, no. 6, pp. 638-645, 2002.

- [15] M. Assenheimer, O. Laver-Mokovitz, D. Malonek, D. Manor, U. Nahaliel, R. Nitzan, and A. Saad, "The T-SCANTM technology: electrical impedance as a diagnostic tool for breast cancer detection," *Physiological Measurement*, vol. 22, pp. 1-8, 2001.
- [16] Y. Z. Ider and O. Birgul, "Use of the magnetic field generated by the internal distribution of injected currents for Electrical Impedance Tomography (MR-EIT)," *Elektrik, Turkish Journal of Electrical Engineering and Computer Sciences*, 6, no 3, 215-225, 1998.
- [17] O. Birgul, M Eyuboglu, and Y. Z. Ider, "A New Technique for High Resolution Absolute Conductivity Imaging Using Magnetic Resonance-Electrical Impedance Tomography (MR-EIT)," *Proceedings of SPIE - the International Society for Optical Engineering, Medical Imaging*, vol. 4320, pp.880-888, 2001.
- [18] H. S. Khang, B. I. Lee, S. H. Oh, E. J. Woo, S. Y. Lee, M. H. Cho, O. Kwon, J. R. Yoon, and J. K. Seo, "J-Substitution Algorithm in Magnetic Resonance Electrical Impedance Tomography (MREIT): Phantom Experiment for Static Resistivity Images," *IEEE Trans. on Medical Imaging*, vol. 21, no. 6, pp. 695-702, 2002.
- [19] O. Birgul, B. M. Eyuboglu, and Y. Z. Ider, "Current constrained voltage scaled reconstruction (CCVSR) algorithm for MR-EIT and its performance with different probing current patterns," *Physics in Medicine and Biology*, vol. 48, no.5, pp. 653-671, 2003.
- [20] O. Birgul, B. M. Eyuboglu, and Y. Z. Ider, "Experimental results for 2D magnetic resonance-electrical impedance tomography (MR-EIT) using magnetic flux density in one direction," *Physics in Medicine and Biology*, vol. 48, no.21, pp. 3485-3504, 2003.
- [21] S. H. Oh, J. Y. Han, S. Y. Lee, M. H. Cho, B. I. Lee, and E. J. Woo, "Electrical Conductivity Imaging by Magnetic Resonance Electrical Impedance Tomography (MREIT)," *Magnetic Resonance in Medicine*, vol. 50, pp 875-878, 2003.
- [22] G. C. Scott, M. L. G. Joy, R. L. Armstrong, and R. M Hankelman, "Measurement of Non-uniform Current Density by Magnetic Resonance," *IEEE Trans on Medical Imaging*, vol. 10, pp 362-374, 1991.
- [23] Y. Z. Ider and L. M. Muftuler "Measurement of AC Magnetic Field Distribution using Magnetic Resonance Imaging," *IEEE Trans. on Medical Imaging*, vol. 16, pp. 617-622, 1997.
- [24] U. Mikac, F. Demsar, K. Beravs, and I. Sersa, "Magnetic Resonance Imaging of Alternating Electric Currents," *Magnetic Resonance Imaging*, vol. 19, pp. 845-56.
- [25] G. C. Scott, M. L. G. Joy, R. L. Armstrong, and R. M. Hankelman, "Electromagnetic Considerations for RF Current Density Imaging," *IEEE Trans. on Medical Imaging*, vol. 14, no. 3, 1995.
- [26] P. P. Silvester and R. L. Ferrari, "Finite Elements for Electrical Engineering," *Cambridge University Press*, 1996.
- [27] R. Sadleir, S. Grant, S. U. Zhang, B. I. Lee, H. C. Pyo, S. H. Oh, C. Park, E. J. Woo, S. Y. Lee, O. Kwon, and J. K. Seo, "Noise analysis in magnetic resonance electrical impedance tomography at 3 and 11T field strengths," *Physiological Measurement*, vol. 26, pp. 875-884, 2005.
- [28] M J Hamamura, T M Muftuler, O Birgul, and O Nalcioğlu, "Measurement of ion diffusion using magnetic resonance electrical imaging tomography," *Physics in Medicine and Biology*, vol 51, pp 2753-2762.

REPORTABLE OUTCOMES

Journal Papers

1. **Birgul O**, Hamamura M J, Muftuler L T, and Nalcioğlu O, “Contrast and spatial resolution in MREIT using low amplitude currents” *Physics in Medicine and Biology*, vol. 51, pp. 5035–5049, 2006.
2. Muftuler L T, Hamamura M J, **Birgul O**, and Nalcioğlu O, “In vivo MRI Electrical Impedance Tomography (MREIT) of tumors” *Technology in Cancer Research and Treatment*, vol. 5, no. 4, pp. 381-387, 2006.
3. Hamamura M J, Muftuler L T, **Birgul O**, and Nalcioğlu O, “Measurement of ion diffusion using magnetic resonance electrical impedance tomography,” *Physics in Medicine and Biology*, Vol.51, No.11, pp.2753-2762, 2006.
4. Muftuler T, Hamamura M, **Birgul O**, and Nalcioğlu O, “Resolution and Contrast in Magnetic Resonance Electrical Impedance Tomography (MREIT) and Its Application to Cancer Imaging, ” *Technology in Cancer Research and Treatment*, vol. 3, no. 6, pp. 599-609, 2004.

Invited Talks

1. **Birgul O**, Hamamura M J, Muftuler L T, and Nalcioğlu O, “Magnetic Resonance-Electrical Impedance Tomography in Breast Cancer Imaging,” *IEEE, International Symposium on Biomedical Imaging*, Arlington VI, 2006.

Conference Papers

1. **Birgul O**, Muftuler T M Hamamura M J, Nalcioğlu O, “3D Magnetic Resonance Electrical Impedance Tomography at 4T using Sensivity Matrix based Reconstruction,” *ISMRM 15th Scientific Meeting and Exhibition Germany*, May 2007.
2. **Birgul O**, Hamamura M J, Muftuler L T, and Nalcioğlu O, “Comparison of Magnetic Resonance Electrical Impedance Tomography at 4T and 7T Field Strengths,” *ISMRM 15th Scientific Meeting and Exhibition Germany*, May 2007.
3. Hamamura M J, Muftuler L T, **Birgul O**, and Nalcioğlu O, “Fast Imaging for Magnetic Resonance Electrical Impedance Tomography,” *ISMRM 15th Scientific Meeting and Exhibition Germany*, May 2007.
4. Hamamura M J, Muftuler M J, **Birgul O**, and Nalcioğlu O, “Magnetic Resonance Electrical Impedance Tomography Using Biologically Safe Injected Current Levels,” *ISMRM 15th Scientific Meeting and Exhibition Germany*, May 2007.
5. Chen G, Muftuler L T, **Birgul O**, Hamamura M J, and Nalcioğlu O, “Mutual Information Based MREIT Reconstruction Using MR Anatomical Data,” *ISMRM 15th Scientific Meeting and Exhibition Germany*, May 2007.
6. Muftuler M J, **Birgul O**, Hamamura M J, and Nalcioğlu O, “Effects of Limited Volume Coverage on Accuracy of MR-Electrical Impedance Tomography”, *ISMRM 15th Scientific Meeting and Exhibition Germany*, May 2007.
7. **Birgul O**, Muftuler L T, Hamamura M J, and Nalcioğlu O, “Reconstruction of Irregular Conductivity Distributions using MREIT at Low Current Levels,” *ISMRM 14th Scientific Meeting and Exhibition Seattle, Washington*, May 2006.
8. Hamamura M J, Muftuler L T, **Birgul O**, and Nalcioğlu O, “Dynamic Magnetic Resonance Electrical Impedance Tomography Using Sub-Milliamp Injected Currents,” *ISMRM 14th Scientific Meeting and Exhibition Seattle, Washington*, May 2006.
9. Hamamura M J, Muftuler L T, **Birgul O**, and Nalcioğlu O, “Electrode Misalignment Correction Algorithms In Magnetic Resonance Electrical Impedance Tomography,” *ISMRM 14th Scientific Meeting and Exhibition Seattle, Washington*, May 2006.

10. Hamamura M J, Muftuler L T, **Birgul O**, and Nalcioglu O, "Multiple Current Injection Schemes In Magnetic Resonance Electrical Impedance Tomography," *ISMRM 14th Scientific Meeting and Exhibition Seattle, Washington*, May 2006.
11. Muftuler L T, Hamamura M J, **Birgul O**, and Nalcioglu O, "In Vivo MRI Based Electrical Impedance Tomography of Malignant Tumors," *ISMRM 14th Scientific Meeting and Exhibition Seattle, Washington*, May 2006.
12. Muftuler L T, Hamamura M, **Birgul O**, and Nalcioglu O, "MRI Based Electrical Impedance Imaging of Tumors with Iterated Sensitivity Reconstruction using Regularization," *ISMRM 13th Scientific Meeting*, 2005.
13. Hamamura M, Muftuler T, **Birgul O**, and Nalcioglu O, "Tracking of Sodium Changes Using MR-EIT," *ISMRM 13th Scientific Meeting*, 2005.

Conference Abstracts and Posters

1. **Birgul O**, Muftuler L T, Hamamura M J, and Nalcioglu O "Magnetic Resonance - Electrical Impedance Tomography (MREIT) Using Iterated Sensitivity Reconstruction Algorithm," IEEE AIPR 2005 Workshop, Multi-modal Imaging Session, Washington, DC, October 19-21, 2005.
2. **Birgul O**, Muftuler L T, Hamamura M, and Nalcioglu O, "Iterated Sensitivity Algorithm for Magnetic Resonance Electrical Impedance Tomography," *Era of Hope DOD Breast Cancer Research Program Meeting*, Philadelphia PA, June 8-11, 2005.
3. Muftuler L T, Hamamura M, **Birgul O**, and Nalcioglu O, "MRI Based Electrical Impedance Imaging of Tumors," *Era of Hope DOD Breast Cancer Research Program Meeting*, Philadelphia PA, June 8-11, 2005.

(Journal and conference papers are included in the appendix section)

PERSONNEL SUPPORTED THROUGHOUT THE GRANT

BIRGUL Ozlem, PhD	Principal Investigator- Dr Birgul worked in all stages of this grant. She got training in first two years, developed reconstruction algorithms and coordinated the experimental and image reconstruction phases of the study. She became an Assistant Researcher in this period.
NALCIOGLU Orhan, PhD	Co-mentor- Dr. Nalcioğlu is a physicist who has done seminal work in many areas of medical imaging especially in MR. He also has considerable experience in tumor pharmacokinetics and imaging. He guided the PI in especially MR experimentation stage of the study.
LEE Eva, MD	Co-mentor- Dr. Lee is a Professor in Department of Biological Chemistry and extensive experience in breast cancer models in animals. She guided the training of the PI in tumor biology.
SU Min-Ying, PhD	Investigator- Dr. Su has substantial experience in breast cancer imaging and specifically on dynamic contrast-enhanced MRI. She assisted the PI in developing techniques for animal imaging and experimenting using DCE-MRI.
HAMAMURA Mark, PhD	Graduate Researcher/Post Doctoral Researcher- Mark Hamamura was a graduate student at UCI, Physics department at the beginning of the project and completed his thesis during this period. He was responsible for the implementation and the testing of the pulse sequences and necessary circuits for the improvement of the MREIT technique.
ZHANG Liquan, BSc	Animal Technician- Ms Zhang was responsible for animal preparation and handling during the last two years of the project.

KEY RESEARCH ACCOMPLISHMENTS

- MREIT system for 3D data acquisition was implemented.
- Mesh generation and image reconstruction algorithms in 3D were developed.
- 3D phantom studies were carried out successfully.
- Preliminary animal experiments that demonstrate conductivity contrast for R3230 tumor models were carried out.
- Data acquisition system was generalized for imaging at different field strengths.
- Preliminary images were acquired using fast imaging sequences that is critical in *in vivo* imaging.
- PI acquired training in tumor biology and different imaging modalities in tumor imaging.

CONCLUSIONS

- We demonstrated the feasibility of using 3D sensitivity matrix reconstruction in multi-slice magnetic resonance electrical impedance imaging. Although sensitivity matrix based reconstruction methods are computationally expensive, they perform well in the presence of noise.
- MREIT imaging is possible at current levels around 1mA and even lower currents can be achieved using faster imaging sequences and averaging.
- MREIT is capable of detecting objects as small as 3mm using low amplitude currents.
- The comparison of MREIT experiments carried out at two different field strengths suggests a slight improvement in higher field strengths.
- In vivo animal images shows that there is an increase in conductivity of tumors and further investigation in improvement of existing hardware and pulse sequences would overcome the motion artifacts.

APPENDICES

Reprints of the documents listed in reportable outcomes section.

Contrast and spatial resolution in MREIT using low amplitude current

**Ozlem Birgul, Mark J Hamamura, L Tugan Muftuler
and Orhan Nalcioğlu**

Tu and Yuen Center for Functional Onco Imaging, University of California Irvine,
California, USA

E-mail: obirgul@uci.edu

Received 9 March 2006, in final form 8 August 2006

Published 19 September 2006

Online at stacks.iop.org/PMB/51/5035

Abstract

Magnetic resonance–electrical impedance tomography employs low amplitude currents injected or induced inside an object. The additional magnetic field due to these currents results in a phase in the MR images. In this study, a modified fast spin–echo sequence was used to measure this magnetic field, which is obtained by scaling the MR phase image. A finite element method with first order triangular elements was used for the solution of the forward problem. An iterated sensitivity matrix-based algorithm was developed for the inverse problem. The resulting ill-conditioned matrix equation was regularized using the Tikhonov method and solved using a conjugate gradient solver. The spatial and contrast resolution of the technique was tested using agarose gel phantoms. A circular phantom with 7 cm diameter and 1 cm thickness is used in the phantom experiments. The amplitude of the injected current was 1 mA. 3, 5 and 8 mm diameter insulators and high conductor objects are used for the spatial resolution study and an average full-width half-maximum value of 4.7 mm is achieved for the 3 mm insulator case. For the contrast analysis, the conductivity of a 15 mm object is varied between 44% and 500% with respect to the background and results are compared to the ideal reconstruction.

(Some figures in this article are in colour only in the electronic version)

1. Introduction

MREIT (magnetic resonance–electrical impedance tomography) is a recently developed imaging modality that reconstructs conductivity images from the magnetic flux density generated due to a current distribution in a volume conductor. The main advantages of MREIT are the non-invasive measurement of the field from inside the object (that increases the sensitivity to inner regions), higher number of measurements without being limited to

detection probes (that improves the resolution), and availability of the MR image for accurate modelling of the geometry and boundary conditions.

Although it is possible to detect locations of lesions in breast cancer using techniques such as x-ray mammography, due to problems of specificity, many women undergo unnecessary biopsies. Therefore, new highly specific techniques are needed to decrease the false positive results while maintaining the high sensitivity (Elmore *et al* 2002). Since the conductivity values of malignant, benign and normal tissues are significantly different, this information can be used in tumour classification (Surowiec *et al* 1988) to improve specificity.

MREIT reconstruction algorithms can be grouped into two depending on the type of data they use. Earlier algorithms generated current density maps from the measurements as an intermediate step towards conductivity reconstruction. The J -substitution method (Khang *et al* 2002), current-constrained–voltage-scaled reconstruction (CCVSR) (Birgul *et al* 2003a) and equipotential projection-based reconstruction (Ozdemir *et al* 2004) are examples of this type of algorithm. The disadvantage of these algorithms is the need for two or three components of the magnetic flux density, which requires rotation of the object inside the magnet. Other algorithms use magnetic flux density measurements directly and the measurement of only one component is sufficient. Sensitivity-based reconstruction (IDER and Birgul 1998, Birgul *et al* 2003b, Muftuler *et al* 2004), the algebraic reconstruction technique (IDER and Onart 2004), variational gradient B_z algorithm (Park *et al* 2004a), gradient B_z decomposition algorithm (Park *et al* 2004b) and response surface methodology (RSM) algorithm (Gao *et al* 2006) fall into the second group of algorithms.

The main advantage of the MREIT technique is the availability of the volume data. In conventional EIT, the number of peripheral voltage measurements are physically limited and therefore it is a highly ill-conditioned problem. In contrast, the magnetic flux density can be measured from within the object with a resolution sufficient to match the number of unknowns in the discretized problem resulting in a better-conditioned problem compared to the conventional EIT technique.

Several studies have been carried out experimentally using phantoms to evaluate the performance of MREIT (Birgul *et al* 2003b, Lee *et al* 2003, Oh *et al* 2004). The major limitation in practice is the amplitude of the current required to achieve an acceptable signal-to-noise ratio. Lee *et al* (2003) reported relative L^2 -errors of 25.5% and 32.3% with denoising and without denoising with an injected current of 28 mA. Birgul *et al* (2003a) carried out experiments with 25 mA peak current and reconstructed conductivity images with 13–17% error without using any denoising techniques at 0.15 T. Oh *et al* (2004) reported 11–35% error when the current was 24 mA. Muftuler *et al* (2004) presented results for phantoms and an *in vivo* tumour bearing animal with current levels that are as low as 2–4 mA using a 3 T magnet. In their study, the ratio of the conductivity of a region of interest to a reference was investigated; therefore, no voltage measurements were acquired resulting in relative conductivity images. In their recent study, Sadleir *et al* (2006) acquired MREIT images using an 11 T MRI system. They have used current levels changing between 5 and 20 mA and presented images for tissue phantoms of different sizes (60 mm and 40 mm both in diameter and height). Recently, Hamamura *et al* (2006) demonstrated measurement of ion diffusion using the MREIT technique in a 70 mm diameter phantom with 900 μ A at 4 T. It must be noted that the field strengths, phantom sizes and imaging parameters are different for all the studies listed above. Therefore, it is not possible to make a direct comparison in terms of an achievable minimum applied current level. A better measure of comparison would be the current density inside the object.

In this study, we used an iterative version of the reconstruction algorithm outlined by Muftuler *et al* (2004) with Tikhonov regularization. This reduces noise sensitivity of

reconstruction and enables one to use lower current levels, which is critical for human applications. The pulse sequence used in data acquisition was also improved so that the noise in the magnetic flux density measurements for low current levels were acceptable. Several agarose phantoms were prepared to characterize the contrast and spatial resolution performance. The details of data acquisition, image reconstruction and reconstructed images are presented in the following sections.

2. Methods

Reconstruction of conductivity involves two basic steps. The first step is the measurement of magnetic flux density using magnetic resonance imaging. This step involves MRI data acquisition using a modified spin-echo pulse sequence and generation of magnetic flux density images from the MRI phase images using scaling. In the second step, these images are used as input data in the inverse problem of finding conductivity from the magnetic flux density information. In this section the components of the hardware and pulse sequence used for data acquisition are presented first. Then, the reconstruction algorithm based on the sensitivity matrix is explained.

2.1. Experimental set-up

The acquisition system for the MREIT consists of a conventional whole body MRI system and a current source that is synchronized with the RF pulses generated by the MRI system.

The MRI system has a 4 T whole body Magnex magnet with a whole body gradient coil set that provides up to 3 G cm^{-1} gradient fields. A 13 channel room-temperature high-order shim coil set was used to minimize field inhomogeneities. This system was interfaced with a MRRS console (magnetic resonance research systems, Guildford, UK) that has broadband RF transmit and receive channels. A 16 leg, quadrature, high-pass birdcage coil with 10 cm diameter and 18 cm length was designed and built in-house for the MREIT experiments.

The current source uses pulses generated by the MRI console and a voltage-to-current converter that uses three LM741 OPAMPs. This current source was triggered by a TTL pulse generated by the scanner computer. The current cables were connected to the object through several RF chokes and low pass filters to suppress RF coupling. These cables were fixed on an acrylic structure that also supports the phantom. The orientation of the cables is critical so that only the effect of current flowing through the object creates a phase in the MR image. The rigid support guarantees that external currents flow parallel to the main magnetic field (z -direction) so that their effect is zero.

2.2. Pulse sequence

The MREIT data were collected using the pulse sequence shown in figure 1. In this pulse sequence, if the RF pulses are not synchronized with the current pulses, the phases generated in positive and negative cycles would cancel each other out. By synchronizing successive π pulses to half cycles of the current, the phase shift accumulates; however, it is superimposed onto the phase component due to main and gradient field inhomogeneities. To extract the current-only component, the experiment is repeated twice with opposite current polarities. When the difference is taken, system-dependent phase shifts cancel out and current-dependent phase, Φ_I , is obtained as

$$\Phi_I(r) = 2\gamma N T_{\text{pulse}} B_z(r), \quad (1)$$

where γ is the gyromagnetic ratio, N is the number of cycles of injected current, $B_z(r)$ is the amplitude of the z -component of the current-generated magnetic field at point r and T_{pulse} is the

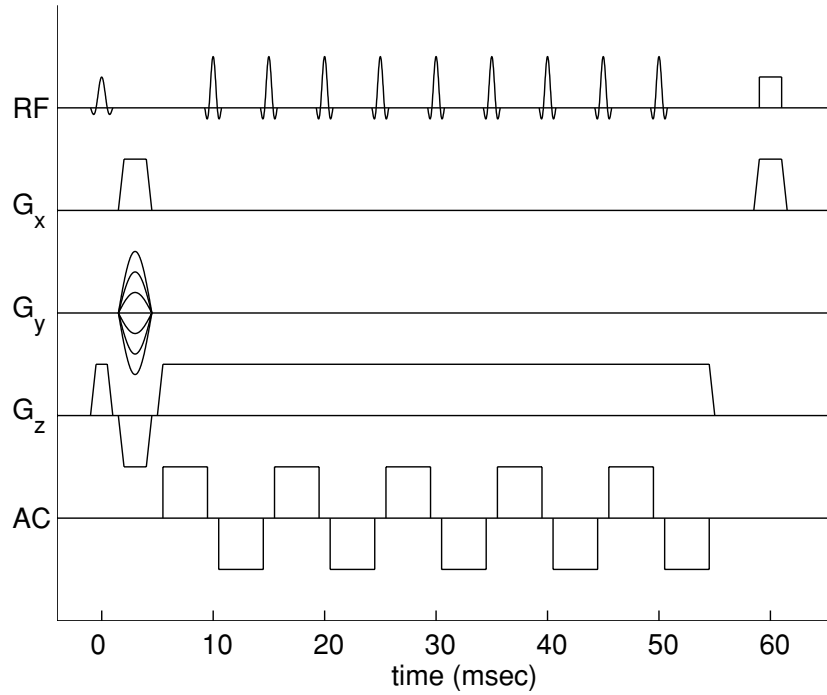


Figure 1. Sample pulse sequence used in the MREIT experiments (parameters used are given in the results section).

duration of each current pulse. Measurement of this phase shift allows for calculation of the z -component of magnetic field distribution. More information about extraction of magnetic flux density from MR images can be found in Muftuler *et al* (2004).

2.3. Forward problem and image reconstruction

The forward problem for MREIT is the calculation of peripheral surface voltage values and the magnetic flux density distribution for known conductivity distribution and boundary conditions. The nonlinear relation between conductivity and potential field is given by the boundary value problem (BVP) defined by Poisson's relation as

$$\nabla \cdot (\sigma(x, y) \nabla \phi(x, y)) = 0 \quad (x, y) \in S \quad (2)$$

for a two-dimensional case, where $\sigma(x, y)$ and $\phi(x, y)$ are the electrical conductivity and potential field distributions in the imaging plane, S . The boundary conditions must be specified together with the above BVP for the solution of the electric field. The electric current on the boundary of the imaging region is specified for the MREIT problem and is imposed as the Neumann boundary condition:

$$-\sigma(x, y) \frac{\partial \phi(x, y)}{\partial n} = \begin{cases} J & \text{on positive current electrode} \\ -J & \text{on negative current electrode} \\ 0 & \text{elsewhere.} \end{cases} \quad (3)$$

Once the potential field distribution is found, the electrical field distribution can be calculated as

$$\vec{E}(x, y) = -\nabla \phi(x, y) \quad (4)$$

and the corresponding current density distribution is obtained using Ohm's relation in field quantities as

$$\vec{J}(x, y) = \sigma(x, y) \vec{E}(x, y). \quad (5)$$

The magnetic flux density at the imaging slice generated due to the current density distribution found in equation (5) is given by the Biot–Savart relation

$$\vec{B}(x, y) = \frac{\mu_0}{4\pi} \int \frac{\vec{J}(x, y) dS \times \hat{a}_R}{R^2}, \quad (6)$$

where μ_0 is the permeability of the free space, \vec{R} is the vector from source point (x', y') to the field point (x, y) and \hat{a}_R is the unit vector in that direction. The finite element method (FEM) with first order triangular elements is used for the discretization of the forward problem.

In the reconstruction process, a uniform conductivity is assumed as the initial distribution and the forward relation between conductivity and magnetic flux density is linearized around this conductivity distribution as explained in detail in Birgul *et al* (2003b). The resulting matrix equation that approximates the relation between conductivity and magnetic flux density perturbations is given by

$$\Delta \mathbf{b} = \mathbf{S} \Delta \sigma, \quad (7)$$

where $\Delta \mathbf{b}$ is the difference between measured magnetic flux density and the magnetic flux density corresponding to initial distribution, $\Delta \sigma$ is the change with respect to initial conductivity distribution and \mathbf{S} is the sensitivity matrix that gives the relation between changes in magnetic flux density and conductivity. The sensitivity matrix is calculated using the semi-analytical method (Birgul *et al* 2003b). The sensitivity matrix is ill-posed in general, and due to noise in the data, some form of regularization is required to be able to solve the system in equation (7). Including the Tikhonov regularization parameter, λ , the matrix equation becomes

$$(\mathbf{S}^T \mathbf{S} + \lambda \mathbf{I}) \Delta \sigma = \mathbf{S}^T \Delta \mathbf{b}, \quad (8)$$

where \mathbf{I} is the identity matrix. The matrix equation is solved for different values of λ using the built-in cgs function of MATLABTM with default settings ($1e^{-6}$ tolerance level, 20 iterations and no pre-conditioning). The optimum regularization value is selected as the one minimizing the difference,

$$\min_{\lambda} \sum_{i=1}^m \|B_{\text{meas},i} - B_{\text{calc},i}(\lambda)\| \quad (9)$$

where m is the total number of measurement points, B_{meas} is the measured magnetic flux density and B_{calc} is the flux density calculated using reconstructed conductivity. For iterations, the calculated conductivity distribution is assigned as the initial value and the steps starting with sensitivity matrix calculation are repeated until the change in conductivity for two consecutive iterations is below a defined threshold. The flowchart of the algorithm is given in figure 2.

Compared to sensitivity-based reconstruction algorithms reported before (Birgul *et al* 2003b, Muftuler *et al* 2004), the major differences of the algorithm used in this study are the following:

- (i) Using conjugate gradient solver (CGS) instead of truncated SVD. This eliminated the requirement of large decomposition matrices, which enables a faster and memory efficient reconstruction.
- (ii) Introducing Tikhonov regularization instead of truncation. The criterion used in selection of the optimum regularization parameter has been explained before in this section. This eliminates operator dependence.
- (iii) Iterating the algorithm to improve accuracy even for large conductivity perturbations.

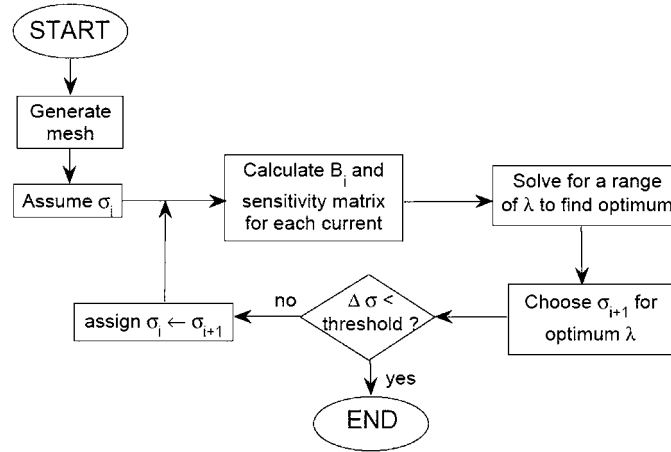


Figure 2. Flowchart of the sensitivity-based iterative reconstruction algorithm.

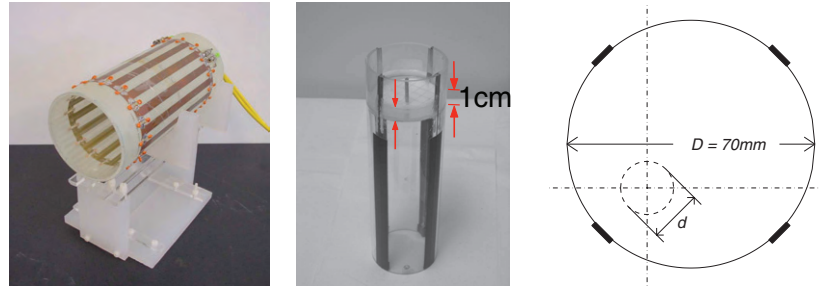


Figure 3. (a) Home-built RF coil. (b) Phantom. (c) Phantom description.

It is known that only relative conductivity values can be reconstructed using magnetic field measurements alone. Using the nonlinear reconstruction outlined above, the conductivity distribution can be found with a scale and peripheral voltage measurements can be used to calculate this scaling factor (Birgul *et al* 2003b). In this study, voltages are not measured and only relative conductivity distributions are found. In the results section, we scaled the conductivity values assuming known voltages to provide readers a basis for comparison.

3. Results

3.1. Phantom preparation

Various agarose gel phantoms were used for the experiments. The agarose powder (OmniPur brand) was mixed with different concentrations of NaCl to generate different conductivity values. 2 g of agarose powder was used per 100 ml of water. Gels were poured into an acrylic cylinder with an inner diameter of 7 cm and height of 1 cm (figure 3). Four electrodes made from 6 mm wide copper tape with conducting glue were placed at $\{\frac{\pi}{4}, \frac{3\pi}{4}, \frac{5\pi}{4}, \frac{7\pi}{4}\}$ along the inner wall, that could provide up to six different current injection pairs. It has been shown that at least two independent current injection profiles are required for the uniqueness of the

Table 1. Measured conductivity values for different NaCl concentrations.

NaCl (g/100 mL)	0.25	1.00	1.20	2.00	4.00	7.00	10.00
Conductivity (S m ⁻¹)	0.43	1.61	1.88	3.02	5.68	9.08	11.22

solution (IDER *et al* 2003) and we selected two current injection set-ups that used opposite electrode pairs. Current carrying wires were placed precisely in the z -direction to eliminate any contribution from the currents flowing in those wires. Wires were mounted on acrylic support beams to establish rigidity.

For all cases, 1 g NaCl/100 g water was used as the background solution. Different amounts of NaCl were used to create different object values. Although NaCl amounts were chosen as multiples of the background reference, due to nonlinearity the conductivity values were not linearly scaled. For the accurate evaluation of the reconstruction values, we measured the conductivity of all solutions independently using a four-electrode conductivity measurement cell. The measured values are given in table 1.

3.2. Pulse sequence and current parameters

The pulse sequence in figure 1 was used with the following parameters:

repetition time	T_R	500 ms
echo time	T_E	58 ms
field of view	FOV	100 mm
number of averages	NEX	4
slice thickness	Δw	5 mm
image matrix		64×64
number of current cycles	N	5
current peak	I_p	1 mA
current frequency	f	100 Hz
number of profiles		2.

The magnetic flux density B_z is measured on a 5 mm slice centred in the 1 cm agar slab defined in figure 1(b). Note that although NEX is listed as four, since the pulse sequence was applied twice with opposite polarities, the effective number of averages was equivalent to eight. The current was applied at 100 Hz with 1 mA peak. The current pulse can be expanded as a summation of infinite sine waves with frequencies corresponding to odd harmonics of the main frequency. Due to timing of the π pulses, only the component at the main harmonic frequency will accumulate additional phase and this scale must be included in the calculations. For each current profile, data acquisition took about 4 min with the above parameters resulting in 8 min total acquisition time. For phantom studies, we did not acquire high resolution anatomical images prior to the MREIT experiment and magnitude images of the MREIT experiment were used for mesh generation. For cases with irregular boundaries, such as small animal imaging, an accompanying high resolution anatomical image would increase the accuracy of the forward solution.

3.3. Reconstruction parameters

A finite element mesh with 1089 nodes and 2048 triangular elements was generated for the forward solver. 6 mm electrode covers two elements with three nodes at the boundary. Phase

Table 2. Spatial resolution analysis.

case	FWHM _x (mm)	FWHM _y (mm)	Peak object (S m ⁻¹)	Mean background (S m ⁻¹)
3 mm ins	4.2	5.3	0.78	1.58
3 mm cond	8.3	7.0	3.01	1.50
5 mm ins	6.0	6.0	0.44	1.61
5 mm cond	8.7	7.4	5.68	1.42
8 mm ins	7.9	8.2	0.27	1.59
8 mm cond	10.6	9.5	6.00	1.37

measurements were acquired on a rectangular grid of 64×64 for the whole field of view and approximately 1000–1100 of these fell into the object region in the mask. Note that the number of measurements, m , depends on the mask specific to each case defined by the signal-to-noise ratio. The highest noise in magnetic field measurements is observed at the phantom–air interface. In iterated sensitivity matrix reconstruction, it is possible to reconstruct conductivity values at points even if the magnetic flux density at that specific location is not available. In order to avoid the errors that can be introduced due to high noise, measurements near the boundary are masked out and are not included in reconstruction. The mask is determined by the noise level in the MR images and can be different for each case. For most cases, out of 1576 pixels of the magnetic field images, 1000–1100 pixels are used in image reconstruction. The sensitivity matrices for each current profile were stacked to have the combined sensitivity matrix, which is indicated by \mathbf{S} in equation (8), of size $2m \times 2048$. For the first iteration the maximum singular value, σ_{\max} , and condition number, $\sigma_{\max}/\sigma_{\min}$, of $\mathbf{S}^T \mathbf{S}$ are 1.13×10^{-12} and 5.2×10^{19} , respectively, when the units of distance, conductivity and current amplitude are cm, S cm⁻¹ and mA, respectively, with an initial conductivity distribution of 0.016 S cm⁻¹. For a typical case, the Tikhonov regularization parameter, λ , is in the order of 10^{-14} for the first iteration which is in the order of 1/100 of the maximum singular value. These values were not fixed for all reconstructions and the Tikhonov regularization parameter was recalculated for each sensitivity matrix using the criterion given in equation (9). Above numbers were only provided to give a reader an idea about the order of these parameters for a typical experiment in this study. The iterations are stopped when the change in overall conductivity is below 3% of the previous iteration and this corresponds to 4–6 iterations.

3.4. Spatial resolution

In order to understand the spatial resolution for low amplitude currents, phantoms that contain objects with different diameters (3 mm, 5 mm and 8 mm) and extreme conductivity cases (insulator (ins) and high conductivity (cond)) were reconstructed. For the insulator cases, hollow cylinders filled with the same agarose–NaCl solution as the background were used. For the high conductivity cases, a solution with 10 g NaCl/100 g water, which gives a 6.70:1 contrast with respect to background, was used.

In figure 4, images reconstructed for conductor cases are given together with corresponding profiles. Profile lines are as defined in figure 3. The full-width at half-maximum (FWHM) values were calculated in two orthogonal profiles passing through the centre of the object (FWHM_x for the x -direction and FWHM_y for the y -direction). In figure 4(d)–(f), profiles, baseline, and half-maximum levels for the measurement are shown. FWHM values for all cases are summarized in table 2.

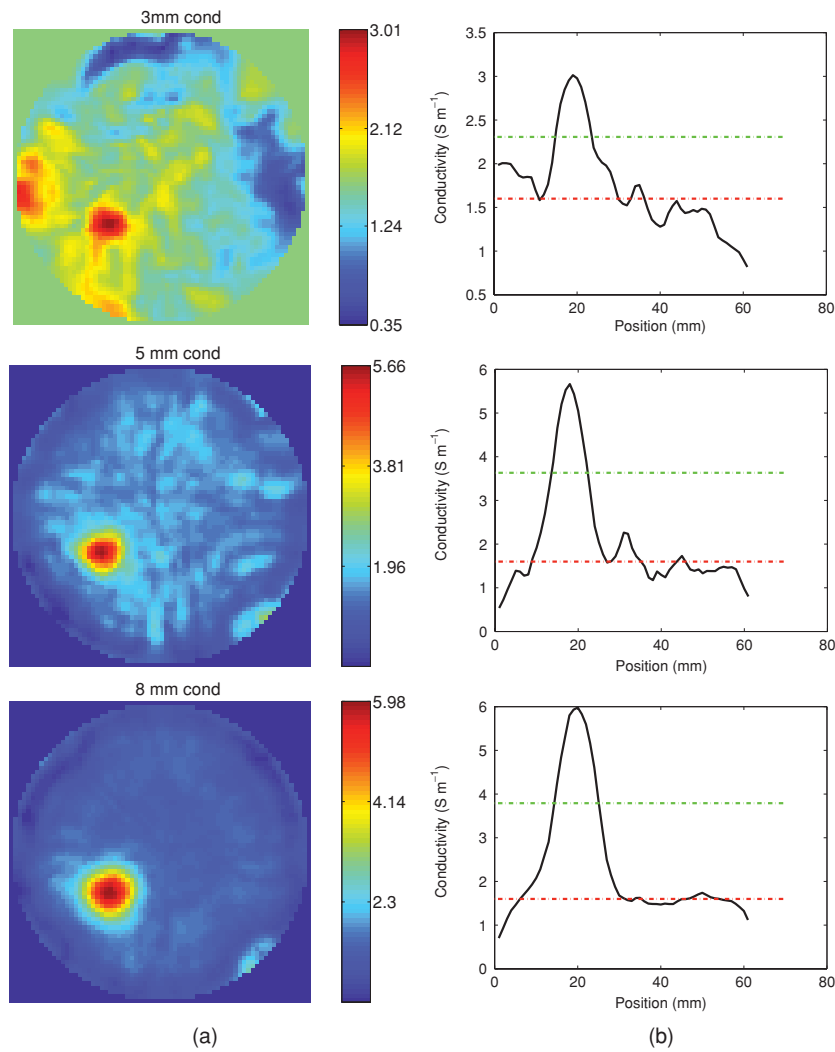


Figure 4. Reconstructed conductivity images for 3, 5 and 8 mm conductor objects and corresponding profiles.

From these values, it is seen that for all cases, the spread is more for the conductor case than the insulator case. Ideally, the spread functions are to be obtained using extreme conductivity cases using a perfect conductor (∞ conductivity) and a perfect insulator (zero conductivity). The experimental insulator case matches this condition closest but the conductor case phantom uses finite conductivity values. Since the NaCl concentrations in the object and background are different, the conductivity of the object decreases with time due to diffusion (Hamamura *et al* 2006). Hamamura *et al* (2006) carried out extensive analysis on diffusion effects in agarose phantoms over a 12 h period by reconstructing images at 11 different time points. After 1 h, the FWHM value of a 12 mm diameter object increases from 11.98 mm to 12.44 mm. This may explain the difference between the spread functions for ins

Table 3. Contrast resolution analysis.

NaCl (g)	True ratio	Reconstructed ratio	True peak	Reconstructed peak	True background	Reconstructed background
0.25	0.36	0.44	0.43	0.70	1.61	1.60
1.2	1.17	1.32	1.88	2.09	1.61	1.58
2	1.88	1.70	3.02	2.61	1.61	1.54
4	3.53	3.45	5.68	4.71	1.61	1.36
7	5.64	5.03	9.08	6.00	1.61	1.19

and cond cases. For example, the 8 mm ins case is equal to the object size whereas for the 5 mm ins case, it is 20% more than the object size.

Another difference between the conductor and insulator cases is the background noise in the reconstructed images. For all cases, conductor images are less noisy compared to the insulator cases of the same size object case. The main reason for this difference is the loss in the measured signal amplitude in perfect insulator regions. The highest change in magnetic flux density occurs at the object boundary; however, due to the insulator shell, this cannot be accurately measured using MRI. Especially for the 3 mm case, where the total volume of the insulator shell becomes significant compared to the object volume, the signal level drops significantly, resulting in low SNR. Therefore, this limit may partially be imposed by the phantom preparation.

We also looked at the peak reconstructed values (maximum/minimum conductivity for conductor/insulator cases) in the object and mean conductivity in the background and these values are also listed in table 2. Note that the significant measure for spatial resolution analysis is the FWHM value; however, the numerical conductivity values are also listed to provide readers an idea. For all cases, expected background conductivity is 1.61 S cm^{-1} . For the insulator cases, the expected object conductivity is zero. For the high conductor case, although the true conductivity value is 11.22 S m^{-1} , reconstructed values are much lower, which could be expected due to diffusion and small object size (PSF effect). If the peak values for different cases are compared, it is seen that as the object size increases, the value increases, towards the true conductivity value.

3.5. Contrast resolution

In order to understand the system performance at different contrast levels, 15 mm diameter objects with five different conductivity values between the two extreme cases used in the spatial resolution analysis were selected. The true conductivity and ratio values and reconstructed peak object and mean background values are summarized in table 3. In the first case, the object conductivity is set lower than the background conductivity (0.36:1 contrast case, case I). In the top row of figure 5, reconstructed image and one of the profiles is plotted. Due to high errors at the boundary, the object is not clearly visible in the image; however, it is well resolved in the profile image. Next, we used a low contrast conductor object where the object conductivity was 17% more than the background (case II). For this case, the noise effects are dominant in the image (figure 5, second row) and the object can hardly be seen in the profile images. Then we increased the conductivity further using three contrast levels, 1.88:1, 3.53:1 and 5.64:1 (cases III, IV and V, respectively), and results are presented in figure 5 and table 3. The noise in the background becomes less significant as the object contrast increases.

For the conductor cases III, IV and V, the peak reconstructed values are lower than the true values which is expected due to the diffusion effect explained in the previous section.

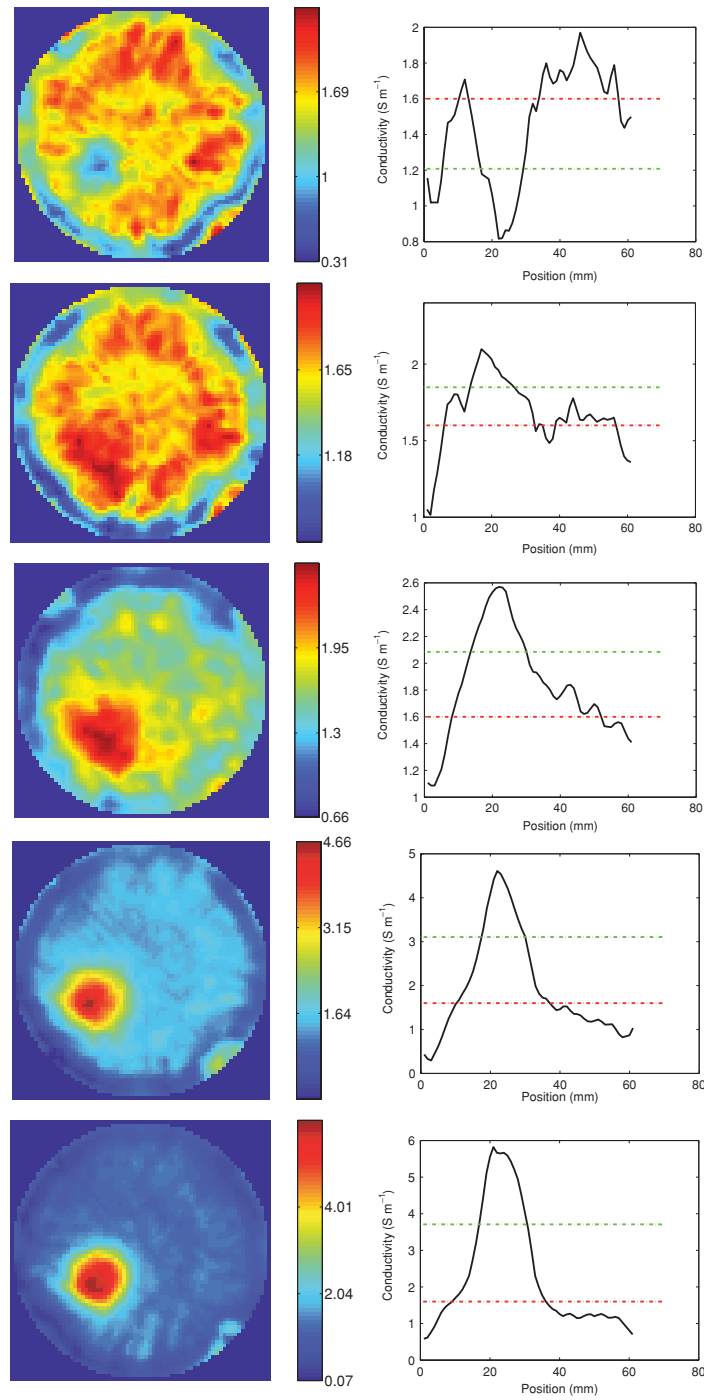


Figure 5. Reconstructed images and corresponding profiles for different contrast objects. From top to bottom (I) 0.36:1, (II) 1.17:1, (III) 1.88:1, (IV) 3.53:1, (V) 5.64:1 contrast cases. Values are listed in table 3.

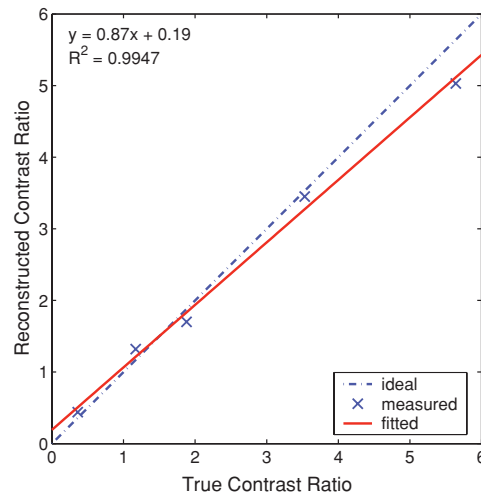


Figure 6. Comparison of experimental contrast ratios obtained to the ideal case.

The same effect results in a higher conductivity peak in the object when the object has lower conductivity (case I) and the direction of diffusion is reversed.

In figure 6, the graph for true contrast ratio versus reconstructed conductivity ratio is presented. In this plot, the dashed line corresponds to ideal reconstruction. It is seen that the deviation from the theoretical case is more for higher conductivity values, which could be due to the nonlinear nature of the governing differential equation.

4. Discussion

In this study, contrast and spatial resolution limits in MREIT are investigated using low level ac currents. We used 1 mA peak current in our experiments and generated conductivity images with better resolution and accuracy compared to other conductivity imaging techniques. Current levels comparable to those in our study are used in Muftuler's (Muftuler *et al* 2004) preliminary study where a couple of phantom results and a small animal result were presented. Since the pulse sequence and reconstruction algorithm are improved, noise performance is also improved.

Small objects with extreme conductivity values were prepared for understanding the spatial resolution limits. 3 mm, 5 mm and 8 mm insulator and high conductor objects were used. Our results suggest that the spatial resolution is 3 mm or better. Due to diffusion effects, for high conductivity cases, the object starts spreading in the conductivity map and an accurate spread measurement is not possible. The FWHM of the 3 mm ins object was measured to be 4.2 mm. Therefore, we can state that the resolution is around 3 mm or better in a 7 cm object when 1 mA current is used. MRI resolution for magnetic flux density measurements was 64×64 for a field of view (FOV) of 100 mm. For this image matrix and FOV, the pixel size in magnetic field images is $1.56 \text{ mm} \times 1.56 \text{ mm}$ and therefore, this is the theoretical spatial resolution that can be achieved with this set of imaging parameters. In order to understand the exact resolution limit, we tried using smaller insulator objects, however, since we cannot get enough MRI signal from inside such a small insulator object, it was not possible to take

measurements from such phantoms. For *in vivo* applications, there may be air spaces such as the air in the lung and in the intestines with low conductivity regions which cause similar problems. Recently, Lee *et al* (2006) proposed a method for conductivity reconstruction from defective data in MREIT to handle such situations.

Several phantoms with different conductivity values were prepared to understand the contrast resolution limits of the low current MREIT. Conductivity values ranging from approximately one fourth of the background to six times the background were used. For the low conductivity case, although the object was clearly resolved, the background error, especially at the boundary, was very high. For the low contrast conductor object, where conductivity of the object was 17% higher than the background, a similar result was obtained and the object was not resolved. It has been reported by several groups that the highest error in measurements is observed at the boundary. In a recent study, Hamamura (2005) suggested several masking and correction algorithms to eliminate these problems. For higher conductivity contrast cases, the boundary effects are not as significant. Diffusion of NaCl from higher to lower concentration also affects the reconstruction here. For low conductivity cases, diffusion is from the background towards the object and reconstructed object conductivity is higher. For higher conductivity cases, the direction of diffusion is reversed and the reconstructed values are lower than the expected values as can be seen from figure 6.

In this study, in order to reduce total data acquisition time, we only used two current injection profiles, which is the minimum required for uniqueness and was sufficient. The total data acquisition time was 8 min for this case. Depending on the application, more current injection profiles may be required. If the data acquisition time is limited, trade off between current profiles and number of the averages must be investigated for optimum SNR.

The first step in the image reconstruction is the selection of the initial conductivity distribution. Theoretically, as long as a uniform conductivity distribution is chosen, the magnetic flux density is independent of its value. When we did reconstruction using real data, however, we observed that initial conductivity distribution affects the convergence speed. For the cases presented here, the results converged in 4–6 iterations if the initial conductivity distribution was equal to or lower than the background and a higher number of iterations was required if the initial conductivity distribution was higher (approximately ten-fold) than the background. Also note that reconstruction results provide relative conductivity values, which is a scaled version of the true values, due to the fact that only the magnetic flux density measurements are used. For breast cancer, the relative conductivity value of tumour with respect to background or a reference organ would provide the necessary information. However, if the absolute conductivity values are required, the scaling factor can be determined using a single voltage measurement.

Recently, several researchers have studied the use of MRI in breast cancer research. MRI is highly sensitive and can detect the location and sizes of the tumours precisely; however, its specificity is low and variable (Su *et al* 1998). Our main motivation in proposing the use of MREIT in breast cancer research is its potential to increase the specificity using the conductivity information. It is reported that the conductivity of malignant tissues maybe 20–40 times higher than benign tissues in some forms of cancer (Surowiec *et al* 1988). Therefore, we expect both the spatial and the contrast resolution achieved in this study are sufficient for applicability of the technique in breast cancer. The main limitation in clinical application of this technique is the safe current amplitude for patient safety. In the future work, *a priori* anatomical MRI information, which is available for any MREIT experiment, can be included in MREIT reconstruction for the improvement of the accuracy of the conductivity with lower current levels towards the aim of translation of the technique to clinical applications.

5. Conclusions

Results presented here are critical in understanding the limits of MREIT at lower currents which is required for translation of the study to animal and ultimately to human applications. Comparison of our results with the literature suggests that using multiple current pulses provides better signal to noise in measurements, and sensitivity-based reconstruction is less susceptible to noise in measurements compared to the gradient-based algorithms.

Acknowledgments

This work was supported in parts by The US Army Medical Research and Materiel Command under W81XWH-04-1-0446 grant and NIH /NCI Award R01-114210.

References

- Birgul O, Eyuboglu B M and Ider Y Z 2003a Current constrained voltage scaled reconstruction (CCVSR) algorithm for MREIT and its performance with different probing current performance *Phys. Med. Biol.* **48** 653–71
- Birgul O, Eyuboglu B M and Ider Y Z 2003b Experimental results for 2d magnetic resonance electrical impedance tomography (MREIT) using magnetic flux density in one direction *Phys. Med. Biol.* **48** 3485–504
- Elmore J G, Barton M B, Moceris V M, Polk S, Arena P J and Fletcher S W 2002 Screening mammograms by community radiologists: variability in false-positive rates *J. Natl. Cancer Inst.* **94** 1376–80
- Gao N, Zhu S A and He B A 2006 New magnetic resonance electrical impedance tomography (MREIT) algorithm: the RSM-MREIT algorithm with applications to estimation of human head conductivity *Phys. Med. Biol.* **51** 3067–83
- Hamamura M J 2005 Electrical impedance tomography using magnetic resonance imaging *PhD Thesis* University of California at Irvine
- Hamamura M J, Muftuler L T, Birgul O and Nalcioglu O 2006 Measurement of ion diffusion using magnetic resonance electrical impedance tomography *Phys. Med. Biol.* **51** 2753–62
- Ider Y Z and Birgul O 1998 Use of magnetic field generated by the internal distribution of injected currents for electrical impedance tomography (MREIT) *Elektr. Turk. J. Electr. Eng. Comput. Sci.* **6** 215–25
- Ider Y Z, Onart S and Lionheart W R B 2003 Uniqueness and reconstruction in magnetic resonance–electrical impedance tomography (MREIT) *Physiol. Meas.* **24** 591–604
- Khang H S, Lee B I, Oh S H, Woo E J, Lee S Y, Cho M H, Kwon O, Yoon J R and Seo J K 2002 J-substitution algorithm in magnetic resonance electrical impedance tomography (MREIT): Phantom experiments for static resistivity images *IEEE Trans. Med. Imaging* **21** 695–702
- Kim Y J, Kwon O, Seo J K and Woo E J 2003 Uniqueness and convergence of conductivity image reconstruction in magnetic resonance electrical impedance tomography *Inverse Problems* **19** 1213–25
- Lee B I, Oh S H, Woo E J, Lee S Y, Cho M H, Kwon O, Seo J K and Baek W S 2003 Static resistivity image of a cubic saline phantom in magnetic resonance electrical impedance tomography *Physiol. Meas.* **24** 579–89
- Lee J Y 2004 A reconstruction formula and uniqueness of conductivity in MREIT using two internal current distributions *Inverse Problems* **20** 847–58
- Lee S H, Seo J K, Park C, Lee B I, Woo E J, Lee S Y, Kwon O and Hahn J 2006 Conductivity image reconstruction from defective data in MREIT: numerical simulation and animal experiment *IEEE Trans. Med. Imaging* **25** 168–76
- Muftuler L T, Hamamura M J, Birgul O and Nalcioglu O 2004 Resolution and contrast in magnetic resonance electrical impedance tomography (MREIT) and its application to cancer imaging *Technol. Cancer Res. Treat.* **3** 599–609
- Oh S H, Lee B I, Park T S, Lee S Y, Woo E J, Cho M H, Seo J K and Kwon O 2004 Magnetic resonance electrical impedance tomography at 3tesla field strength *Magn. Reson. Med.* **51** 1291–6
- Oh S H, Lee B I, Woo E J, Lee S Y, Cho M H, Kwon O and Seo J K 2003 Conductivity and current density image reconstruction using harmonic B_z algorithm in magnetic resonance electrical impedance tomography *Phys. Med. Biol.* **48** 3101–16
- Ozdemir M S, Eyuboglu B M and Ozbek O 2004 Equipotential projection-based magnetic resonance electrical impedance tomography and experimental realization *Phys. Med. Biol.* **49** 4765–83
- Park C, Park E J, Woo E J and Kwon O 2004a Static conductivity imaging using variational gradient bz algorithm in magnetic resonance electrical impedance tomography *Physiol. Meas.* **25** 257–69

- Park C, Kwon O, Woo E J and Seo J K 2004b Electrical conductivity imaging using gradient bz decomposition algorithm in magnetic resonance electrical impedance tomography (MREIT) *IEEE Trans. Med. Imaging* **23** 388–94
- Sadleir R, Grant S, Zhang S U, Oh S H, Lee B I and Woo E J 2006 High field MREIT: setup and tissue phantom imaging at 11T *Physiol. Meas.* **27** S261–70
- Su M Y, Muhler A, Lao X and Nalcioglu O 1998 Tumor characterization with dynamic contrast-enhanced MRI Using MR contrast agents of various molecular weights *Magn. Reson. Med.* **39** 259–69
- Surowiec A J, Stuchly S S, Barr J R and Swarup A 1988 Dielectric properties of breast carcinoma and the surrounding tissues *IEEE Trans. BME* **35** 257–63

***In Vivo* MRI Electrical Impedance Tomography (MREIT) of Tumors**

www.tcrt.org

L. Tugan Muftuler, Ph.D.
Mark J. Hamamura, Ph.D.
Ozlem Birgul, Ph.D.
Orhan Nalcioğlu, Ph.D.

A significant increase in electrical conductivity of neoplasticities compared to healthy tissues and benign formations has been reported in several studies. We previously reported preliminary results with MR based Electrical Impedance Tomography (MREIT) on several phantoms and a single animal. In the presented study, we applied the technique on ten tumor-bearing rats and collected MREIT images to investigate the potential of MREIT for characterizing malignant tumors. Results show that the tumors had significantly higher mean conductivity compared to the mean of conductivity in the rest of the body. Although heterogeneity of conductivity was observed in the tumor, the mean was still higher than the background.

Keywords: MREIT; Electrical Impedance Tomography; MRI; and Cancer imaging.

Introduction

Several *in vitro* studies have shown that the electrical impedance of malignant tissues is significantly higher than those of normal and benign tissues (1, 2). Therefore, *in vivo* impedance imaging of suspicious lesions has the potential to improve the sensitivity and specificity of detecting malignant tumors. Imaging of conductivity distribution can be achieved by Electrical Impedance Tomography (EIT) in which weak electrical currents are injected into or induced in the body and surface voltage measurements are made to reconstruct a conductivity image (3). However, in this technique a limited number of measurement electrodes are placed on the outer surface. This results in poor, non-uniform spatial resolution due to low sensitivity of the voltages to conductivity changes in the interior regions (4).

Imaging conductivity distribution for diagnosing cancer has been proposed by several researchers (5, 6). Cherepenin *et al.* proposed a conventional EIT system for breast cancer screening, while Malich *et al.* used a newly developed instrument called Electrical Impedance Scanning (EIS). In EIS, electrical currents are injected to the body by a single probe held by the patient and an electrode array placed over the breast is used to measure the distribution of currents on the surface of the breast. This information is used to estimate the distribution of conductivity under the electrode array. Although these techniques proved to be useful, both suffer from poor spatial resolution and poor sensitivity to deeper structures.

Magnetic Resonance-Electrical Impedance Tomography (MREIT) has been recently introduced, in which weak electrical currents are injected into the tissue

John Tu & Thomas Yuen Center for
Functional Onco-Imaging
University of California
164 Irvine Hall
Irvine, CA 92697-5020, USA

*Corresponding Author:
L. Tugan Muftuler, Ph.D.
Email: muftuler@uci.edu

Abbreviations: MRI, Magnetic Resonance Imaging; EIT, Electrical Impedance Tomography; MREIT, Magnetic Resonance Electrical Impedance Tomography; FEM, Finite Element Method; EIS, Electrical Impedance Scanning; OPAMP, Operational Amplifier; SVD, Singular Value Decomposition; NEX, Number of Excitations; SMM, Sensitivity Matrix Method

and the resulting perturbations in the magnetic flux density are measured using phase information in MR images. The conductivity distribution inside the body is reconstructed from these magnetic flux density measurements (7-9). Unlike conventional EIT, the MREIT technique provides measurements from inside the object on a uniform, high resolution grid. This provides uniformly distributed high spatial resolution conductivity images.

Several MREIT studies using biological tissue phantoms have been previously reported (10-12). However, these studies were done on *in vitro* samples using injected current levels of 12 mA and above. For any *in vivo* study, these current levels are substantially higher than biologically safe current limits and will certainly cause involuntary muscle twitching even if they do not harm the animal. In some of our experiments, we have observed involuntary muscle twitching even at current levels as low as 2mA, if the electrodes are placed near a major nerve bundle by coincidence. In those cases the experiment is immediately stopped and electrodes are relocated to avoid any discomfort to the animal.

We have recently reported our preliminary studies with phantoms as well as one *in vivo* experiment (13). Here, we present the results of MREIT performed on ten animals. Parameters like variance and mean in the tumor versus the rest of the body were investigated. The goal is to verify the potential of MREIT to aid in the diagnosis of tumors.

Methods

Data were collected using a 4T whole body MRI magnet (Magnex Scientific Inc., UK), which is interfaced with a MRRS console (Magnetic Resonance Research Systems, Guildford, UK) that has broadband RF transmit and receive channels. The system is equipped with a whole body gradient coil set (Tesla Eng. UK), which provides up to 3G/cm gradient fields. The clear bore of the magnet is 650mm in diameter with the gradient tube. The system also includes a 13 channel room-temperature high-order shim system with MXA-13-4 shim power supply (Resonance Research, Billerica, MA) to minimize field inhomogeneities. A 16 leg, quadrature, high-pass birdcage coil was designed and built in-house for the MREIT experiments. This coil has 10 cm diameter and 18 cm length, which is suitable to image large size sprague-dawley rats used in the experiments.

Pulse Sequence

The pulse sequence used for the MREIT experiments employs a train of 180° RF pulses following a 90° RF pulse (Fig. 1). No spatial encoding gradients were applied between the 180° RF pulses and the data was collected with a single read-out gradient only after the last 180° RF pulse. Alternating

electrical currents were injected to the animals in the form of burst sine wave pulses in synchrony with the RF pulse train where polarity of current changed after each 180° RF pulse. The duration of each 180° RF pulse was 1.3ms. A similar sequence was proposed by Mikac *et al.* to obtain an image of electric currents inside an object (14).

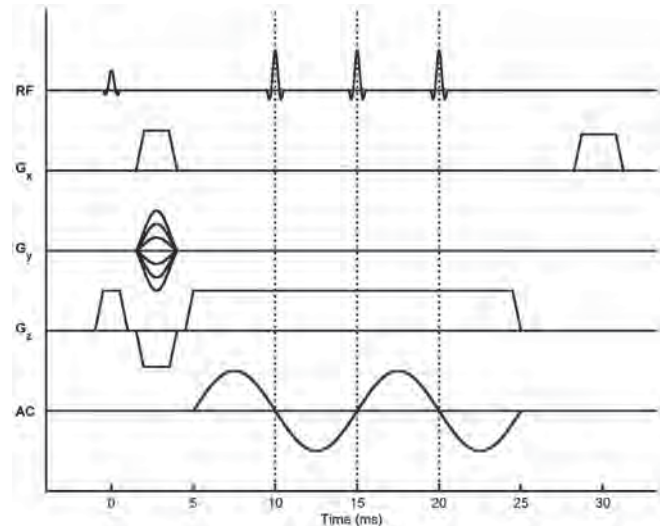


Figure 1: The MREIT pulse sequence for multi-slice conductivity imaging.

These currents flowing inside the animal's body generate a magnetic flux density. The component of the magnetic flux density that is parallel to the main static field (z-component) introduces a phase shift that accumulates over each half-cycle of the sine wave. The signal equation for MREIT is given as:

$$s(u,v) = \iint M(x,y) e^{j\theta(x,y)} e^{j(xu + yv)} e^{j\int_0^t (b(x,y)\cos(\omega t))dt} dx dy \quad [1]$$

Here, $M(x,y)$ is the magnetization of protons at (x,y) , and the T1, T2 decays are ignored to simplify the equation (they can be considered as constant weighting factors, thus $M(x,y)$ accounts for the proton density as well as the T1 and T2 weighting). The constant phase shifts due to various sources such as static field inhomogeneity and other hardware related phase delays are all summarized in the phase term $\theta_{(x,y)}$, γ is the gyromagnetic ratio, and u and v are the spatial frequencies given by $u = \gamma \cdot G_x \cdot T_{Gx}$ and $v = \gamma \cdot G_y \cdot T_{Gy}$, where T_{Gx} and T_{Gy} are the durations of the gradient pulses G_x and G_y , respectively. Therefore, in the MREIT image the total phase accumulated at a pixel at location (x,y) due to the magnetic flux density generated by injected currents is:

$$\varphi(x,y) = 4 \cdot \gamma \cdot N \cdot b(x,y) / \omega \quad [2]$$

where N is the number of cycles of injected current, ω is the angular frequency, and $b(x,y)$ is the amplitude of the magnetic flux density at point (x,y) (z-component only) generated by injected currents. This phase term in Equa-

tion [2] can be easily measured from the MREIT images. Therefore, the z-component of the magnetic flux density distribution can be calculated.

Since the constant phase term $\theta_{(x,y)}$ is unknown, the data has to be collected twice with the polarity of electric current reversed. When the phase of these two MREIT images are subtracted, static phase terms will be eliminated, leaving only the phase term introduced by $b(x,y)$.

MREIT Hardware: Several hardware components were interfaced to the MRI system to perform the experiments. The MRI console controls the whole experiment, which generates the pulse sequence, acquires the incoming data, and synchronizes the external units. The sine waves were produced by an HP ESG-4400B signal generator. These signals were synchronized to the pulse sequence by a TTL pulse generated by the scanner computer. A transconductance amplifier was designed and built using three LM741 OPAMP circuits to convert the voltage from the signal generator into a current output. This circuit is described in detail in (15), which was replicated from (16). The output current was calibrated to 1ma/2V and an independent measurement of current was not used. This experimental procedure was described in more detail in (13). After data collection, raw MRI data (k-space) was uploaded to another computer for off-line processing.

MREIT Conductivity Image Reconstruction

A relationship between the conductivity distribution inside an object and the measured magnetic flux density has to be established to be able to reconstruct images of conductivity. If all three orthogonal components of the magnetic field were known, Maxwell's equations could have been utilized to calculate the current density distribution. However, this is only possible by rotating the object in three orthogonal directions inside the MRI system which will not be practical with human subjects. Even with small animals, rotation would introduce problems with registration of measurements taken with different orientations of the body under investigation. The geometry of the soft tissues would deform due to gravity, complicating the registration further. Moreover, a larger RF coil would have to be used, which would reduce the SNR. Therefore, a method was adopted that uses only the z-component of the magnetic flux density to calculate the conductivity distribution (7, 8).

In order to calculate the relationship between the conductivity distribution of an object and the magnetic flux density generated by currents flowing inside that object, we first start with the calculation of the electric potential distribution $\phi(x,y,z)$ in the imaging slice. This is calculated by solving Poisson's equation with Neumann boundary conditions, which is given by:

$$\begin{aligned} \nabla \cdot (\sigma \nabla \phi)(x,y) &= 0 & (x,y) \in D \\ \sigma \frac{\partial \phi}{\partial n} &= \begin{cases} J \text{ on positive current electrode} \\ -J \text{ on negative current electrode} \\ 0 \text{ elsewhere} \end{cases} \end{aligned} \quad [3]$$

where σ is the electrical conductivity, ϕ is the electric potential, and D is the slice of object to be imaged. The above problem is a nonlinear equation since the electric potential itself is also conductivity dependent. It is difficult to obtain an analytic solution for Equation [3]; therefore, numerical methods should be used. In this study, the Finite Element Method (FEM) was used to calculate the distribution of the electric potential. Once ϕ is calculated, the electric field and current density distribution inside the imaging region may be found using the following equations:

$$\begin{aligned} \vec{E} &= -\nabla \phi \\ \vec{J} &= \sigma \vec{E} \end{aligned} \quad [4]$$

Finally, the magnetic flux density generated by this ohmic current can be calculated using the Biot-Savart law. The magnetic field can be written in terms of the differential current element $I d\vec{l}$ as,

$$\vec{B}(x,y,z) = \frac{\mu_0}{4\pi} \int \left(\frac{I d\vec{l} \times \vec{R}}{R^3} \right) \quad [5]$$

where μ_0 is the permeability constant and \vec{R} is the vector from the source point at (x', y', z') to the field point (x, y, z) . Using Equations [3]-[5], one can solve the *forward problem* where the magnetic field is calculated for an initial conductivity distribution. In order to solve the *inverse problem* of finding the conductivity image from the magnetic flux density measurements, the *sensitivity matrix method* (SMM) was employed, in which a linear relationship between the conductivity perturbations, $\Delta\sigma$, and magnetic flux density perturbations, $\Delta\mathbf{B}$, was assumed (8). This relationship is given as:

$$\begin{bmatrix} \Delta B_1 \\ \Delta B_2 \\ \vdots \\ \Delta B_m \end{bmatrix} = \begin{bmatrix} \frac{\partial B_1}{\partial \sigma_1} & \frac{\partial B_1}{\partial \sigma_2} & \dots & \frac{\partial B_1}{\partial \sigma_n} \\ \frac{\partial B_2}{\partial \sigma_1} & \frac{\partial B_2}{\partial \sigma_2} & \dots & \frac{\partial B_2}{\partial \sigma_n} \\ \dots & \dots & \ddots & \dots \\ \frac{\partial B_m}{\partial \sigma_1} & \frac{\partial B_m}{\partial \sigma_2} & \dots & \frac{\partial B_m}{\partial \sigma_n} \end{bmatrix} \cdot \begin{bmatrix} \Delta \sigma_1 \\ \Delta \sigma_2 \\ \vdots \\ \Delta \sigma_n \end{bmatrix} \quad [6]$$

$$\Delta \mathbf{B}_z = \mathbf{S} \cdot \Delta \sigma$$

Here, $\Delta \mathbf{B} = \mathbf{B}_{\text{meas}} - \mathbf{B}_i$ and $\Delta \sigma = \sigma_{\text{calc}} - \sigma_i$; where σ_i is the initial estimate of the conductivity distribution and \mathbf{B}_i is the field distribution corresponding to σ_i . For most cases, a uniform distribution is assumed for σ_i . \mathbf{B}_{meas} is the magnetic flux density measurements obtained from MRI. If there are n conductivity elements in the FEM and m measurement points from MREIT data, then $\Delta \sigma$ is an $n \times 1$ vector, $\Delta \mathbf{B}$ is

an $m \times 1$ vector and the *sensitivity matrix* \mathbf{S} is an $m \times n$ matrix. The entry of the sensitivity matrix at i^{th} row and j^{th} column denotes the change in the i^{th} field measurement due to a small change in conductivity of the j^{th} element. The sensitivity matrix can be calculated using either a numerical or a semi-analytical approach. In the numerical approach, each column of the sensitivity matrix is calculated separately by solving the forward problem by changing the conductivity of a single element. This approach requires the repetitive solution of the forward problem and increases the execution time. For faster reconstruction, the semi-analytical method was used for the calculation of the sensitivity matrix which was described in (8). Once \mathbf{S} is calculated, the conductivity distribution can be approximated by:

$$\Delta\sigma = \mathbf{S}^{-1} \cdot \Delta\mathbf{B} \quad [7]$$

Since SMM approximates the relationship between perturbations in conductivity and perturbations in B_z (z component of magnetic flux density) with a linear matrix equation, this reconstruction method provides accurate results only for small conductivity perturbations. On the other hand, several researchers reported substantial changes in conductivity between normal and malignant tissues (1, 2). Therefore, SMM will tend to underestimate the actual conductivity contrast. In this study, an iterated SMM with Tikhonov regularization was used to solve the nonlinear imaging problem and also to reduce the artifacts, especially near the boundaries close to the electrodes. The solution to Equation [7] is found by solving the least squares problem:

$$\min \|\mathbf{S}\Delta\sigma - \Delta\mathbf{b}\| \quad [8]$$

where $\|\cdot\|$ is the L_2 norm. For most cases, the problem above is ill-conditioned and a regularization method that computes an approximate solution through a regularization parameter is required. In this study, the linear equation was solved using the conjugate gradient method with Tikhonov regularization, where σ_{calc} was found by introducing an additional term to the cost function:

$$\min \{\|\mathbf{S}\Delta\sigma - \Delta\mathbf{b}\|^2 + \lambda \|\Delta\sigma\|^2\} \quad [9]$$

where λ is the regularization parameter. This approach attempts to minimize the residual norm while penalizing large perturbations in the solution ($\Delta\sigma$). The regularization parameter λ was chosen such that the calculated B_z generated by the reconstructed conductivity distribution was closest to the magnetic flux density measured by MREIT:

$$\min_{\lambda} \{\|B_{\text{final}} - [B(\sigma)]_{\sigma = \sigma_{\text{calc}}(\lambda)}\|\} \quad [10]$$

Once σ_{calc} is calculated, the change in conductivity $\Delta\sigma$ was checked against a predefined threshold, then this σ_{calc} was as-

signed as the new, updated σ_i , and the process was iterated.

The SMM reconstructs relative conductivities. Thus, the true conductivity distribution is related to the reconstructed conductivity distribution by a constant scaling factor. Determining the absolute conductivity distribution requires an additional constraint, such as a surface voltage measurement (17).

In Vivo Experiments

Ten rats bearing malignant tumors were imaged in this study. Data sets from two animals were discarded due to severe motion artifacts. The tumors were either R3230AC tumor grafts or induced by the carcinogen ENU (N-ethyl-N-nitrosourea) (18). Animals were anesthetized by IV injection of ketamine and xylazine prior to imaging. All procedures were approved by the IACUC.

An animal holder was prepared from acrylic sheets for *in vivo* MREIT experiments (Fig. 2). This holder helped keep the animal and the electrodes stationary during imaging. This structure also enabled placement of the electrodes in consistent positions across different animals as well as on the same animals for potential longitudinal studies. 5mm \times 5mm self-adhesive copper foil was taped over hollow acrylic tubes as electrodes. Those tubes were filled with CuSO₄ solution as an MRI marker to detect the electrode positions precisely in the images. Precise localization of electrode positions is essential to enter correct boundary conditions for accurate reconstruction of impedance images. Otherwise, artifacts were seen especially along the periphery, near the electrodes. Thin copper wires that carried the electrical current ran along these tubes, and the tubes were aligned in z-direction to minimize interference from the magnetic flux density generated by current in the wires. The electrodes were covered with a thin layer of conductive gel to provide good electrical contact. The skin areas where the electrodes would be placed were shaved for better conductance.

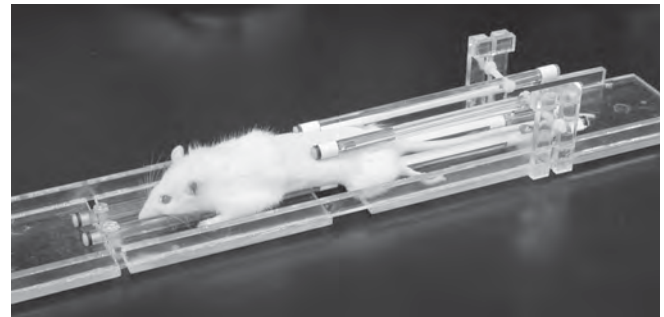


Figure 2: Animal holder with a rat is shown. The electrodes are placed on the tubes and current carrying wires run along those tubes.

Structural images were collected using a T2 weighted SE sequence. Scan parameters were: data matrix = 128 \times 128; FOV = 10 cm; slice thickness = 4 mm, with 2 mm gap. TR

= 3s, TE = 50 ms, and NEX = 2 were used. MREIT images were collected using the outlined pulse sequence with TR = 1000 ms, TE = 30 ms, and NEX = 2; 64×64 data matrix, FOV = 10 cm, slice thickness = 4 mm with 2 mm gap. Two cycles of 100Hz current with 1mA peak was applied for all studies. One set of MREIT data was collected by applying the current between one pair electrodes. Since there were four electrodes, subsequent MREIT data were collected by applying current from different pairs, generating six different current profiles (Fig. 3). As mentioned previously, data were collected with both \pm polarities of the currents to eliminate phase accumulation from other sources. In two of the rats, we have also collected MRIET data with current amplitudes of 0.5, 1, and 2mA.



Figure 3: Six different current injection profiles with four electrodes used in the experiments.

Magnetic flux density calculations and conductivity reconstruction algorithms utilizing the iterative SMM with Tikhonov regularization were developed using MATLAB. For reconstruction, the FEM mesh boundary was determined using a standard MR magnitude image. Between $n = 757$ to 1037 conductivity elements and $m = 280$ to 473 measurement points were utilized in reconstruction, with the exact values being specific to the geometry of the animal being analyzed.

Results

Figure 4 shows T2 weighted MRI and MREIT images of six rats. Tumor areas show increased conductivity depicted with yellow-red colors (see colorbar). On the MREIT images of the animals, separate ROIs (region of interest) were drawn over the tumor region and the rest of the body and the mean conductivity values in these ROIs were calculated. Since the SMM yields relative conductivity values, the ratio of mean conductivities $\sigma_{\text{tumor}}/\sigma_{\text{body}}$ was calculated for each animal and the graph is shown in Figure 5. It was found that the average of these conductivity ratios pooled over eight animals was 2.17. ROIs were drawn manually based on the tumor

observed in T2 weighted MRI images. We have also calculated the ratio of standard deviation to mean conductivity in each tumor region, which may be an indication of *conductivity heterogeneity* inside the tumor volume, rather than SNR (Figure 6). As seen from these figures, consistent results were obtained from these eight animals. Average conductivity increased by roughly 2.2 times in the tumor compared to the rest of the body. The conductivity varied typically between 10% and 20% within the tumor. In two of the rats, from which we have collected MRIET data with current amplitudes of 0.5, 1, and 2mA, highly consistent results were seen especially between 1 and 2mA cases. For example, when MREIT images of 1mA and 2mA cases were subtracted, the mean of the residual was only 1.3% of the mean conductivity in the whole slice. In the case of 0.5mA vs. 1mA, the mean of the residual was 12%. Since the SMM gives relative conductivity distributions, the reconstructed conductivity values have an arbitrary scaling; therefore, the mean of each MREIT image is scaled to the same value before subtraction.

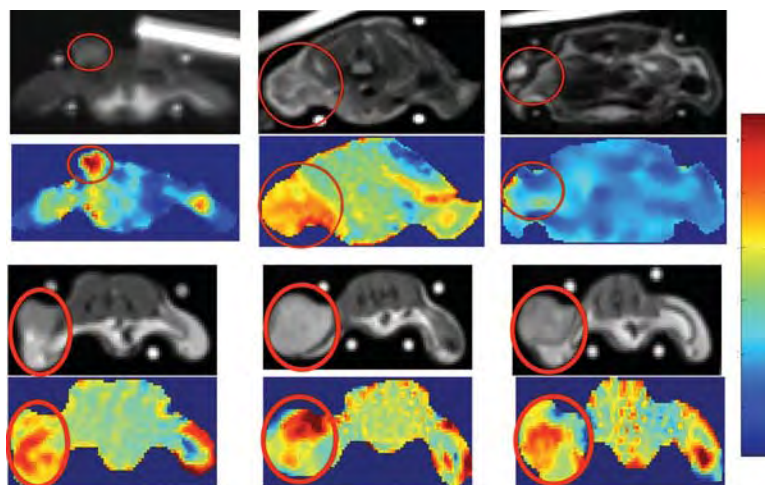


Figure 4: Structural and MREIT images of six animals are illustrated. Anatomic (T2 weighted) scans are displayed in gray levels and corresponding impedance (MREIT) images are depicted in color right below the T2 weighted images. Each image pair shows axial images from different animals. Tumor areas are circled with red lines. Bright objects outside the animals' body were markers to identify exact location of electrodes.

Discussion

In this study, it has been demonstrated that MRI based impedance imaging has the potential to investigate malignant tumors *in vivo*. This method can be used to identify and characterize neoplasticities, which are known to possess higher electrical conductivity with respect to healthy tissues and benign formations. In using the SMM, only relative conductivities can be found. However, only contrasts in conductivity were required to differentiate tumors from the surrounding background tissue. Higher conductivity inside the tumor was observed consistently in all the animals imaged. Moreover, it was observed that the method was sensitive enough to reveal conductivity heterogeneity in tumors. The same heter-

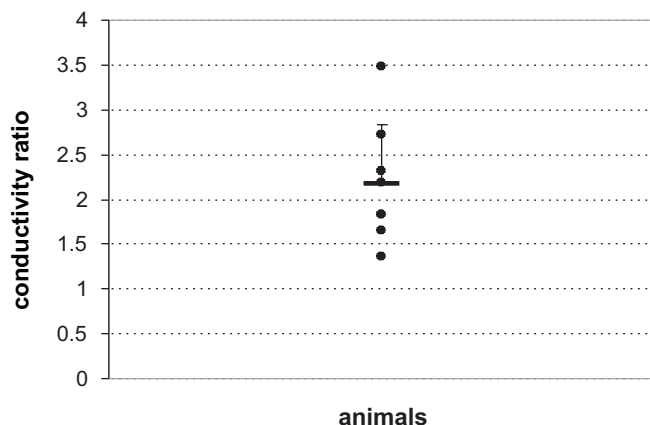


Figure 5: The ratio of mean conductivity in the tumor versus the rest of the body over eight *in vivo* studies. Mean and standard deviation of these measurements are indicated by the dash and the error bar, respectively.

ogenous structure was observed at different current levels in the same animal; therefore, the variations were not random noise. There is still possibility that some systematic errors in data acquisition or reconstruction might have caused such consistent variations. Even though such patterns were not observed in phantom studies, the much more complex structure of the animal might have amplified such systematic errors. This needs to be investigated further.

We have previously carried out extensive phantom studies to optimize the method and assess the spatial resolution, contrast, and linearity (13). More robust reconstruction with regularization was developed to minimize artifacts. Software correction algorithms were developed to minimize electrode localization errors, which helped reduce boundary artifacts.

Although the animal model of breast cancer used in this study is a suitable one to perform preliminary studies of *in vivo* MREIT, it also introduced motion artifact problems. This could be easily avoided in actual human studies. In breast imaging, the breasts are stationary and chest motion can be kept outside the breast images by selecting phase encoding in the left-right direction. However, in future tests with animal models, we plan to utilize motion correction schemes such as navigator echoes to minimize the errors caused by motion. Moreover, the abdominal region of a rat is a more complicated structure compared to a woman's breast, when all the internal organs and their inherent motion are considered. Therefore, we expect the MREIT images to be more accurate in potential applications of MREIT on human breast.

This study utilized a 2D FEM based reconstruction, where the electrodes were placed within the imaging plane and the current flow assumed restricted within this plane. While formulation of the SMM remains the same for 3D, the increase in the size of the matrices and added complexity of the 3D FEM presents additional challenges. For this study, a 2D simplifi-

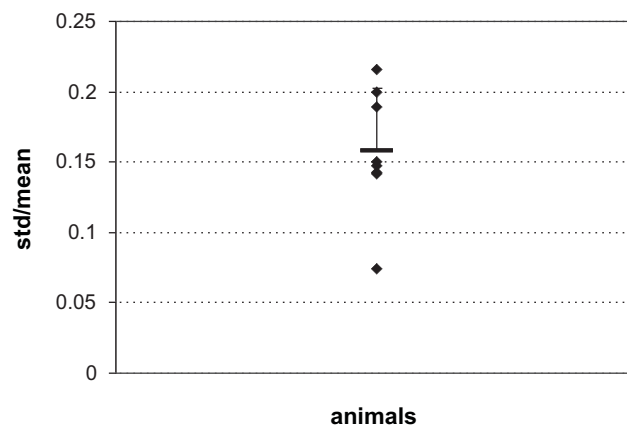


Figure 6: The ratio of standard deviation of conductivity versus its mean in the tumor in eight *in vivo* studies. Mean and standard deviation of these measurement are indicated by the dash and the error bar, respectively.

cation was implemented to reduce computation time. However, the quality and accuracy of conductivity images can be further improved by utilizing 3D FEM based reconstruction. Some of the residual noise or artifacts in the conductivity images could be due to the superposition of magnetic fields generated by currents flowing outside the imaging slice. This can only be modeled by 3D FEM and reconstructed accurately, which is currently being developed.

The positioning of the surface electrodes also plays a crucial role, since this directly affects the current density distribution. Conceivably, placing the electrodes in a certain arrangement may improve the reconstruction results in specific regions (*e.g.*, regions with higher current density) while reducing the sensitivity in others. In this study, the electrodes were arranged in a generic manner by placing them within the imaging plane and approximately equidistant around the animal. The reconstruction may be improved by using *a priori* information to determine specific regions of interest, and then placing the electrodes accordingly. Such optimization of electrode positioning needs to be investigated further.

At this stage the technique may not be used as a standalone diagnostic tool; but it could provide useful information in characterizing the tumor, once a suspicious lesion is detected by other methods. Physiological and structural changes in tumors that lead to such changes in conductivity will be investigated in future studies. Note that good quality MREIT images were collected with biologically safe electrical current levels. To the best of our knowledge, our research group is the only one to demonstrate potential use of MR based impedance imaging in diagnosing or characterizing tumors. The method is still in its early development stages. Further refinements of this technique could improve accuracy more and may reveal important information about the tumor characteristic that cannot be observed with other techniques.

Acknowledgements

This research was supported in part by grants NIH R01 CA114210, DOD DAMD17-02-1-0326 and DOD W81XWH-04-1-0446.

References

1. Surowiec, A. J., Stuchly, S. S., Barr, J. R., and Swarup, A. Dielectric Properties of Breast Carcinoma and the Surrounding Tissues. *IEEE Trans. on BME* 35, 257-263 (1988).
2. Jossinet, J. The Impedivity of Freshly Excised Human Breast Tissue. *Physiol. Meas.* 19, 61-75 (1998).
3. Barber, D. C., Brown, B. H. Applied Potential Tomography. *J. Phys. E.: Sci. Instrum.* 17, 723-733 (1984).
4. Seagar, A. D., Barber, D. C., and Brown, B. H. Theoretical Limits to Sensitivity and Resolution in Impedance Imaging. *Clin. Phys. Physiol. Meas.* 8, A13-31 (1987).
5. Cherepenin, V., Karpov, A., Korjnevsky, A., Kornienko, V., Mazaletskaya, A., Mazourov, D., and Meister, D. A 3D Electrical Impedance Tomography (EIT) System for Breast Cancer Detection. *Physiological Measurement* 22, 9-18 (2001).
6. Malich, A., Boehm, T., Facius, M., Freesmeyer, M. G., Fleck, M., Anderson, R., and Kaiser, W. A. Differentiation of Mammographically Suspicious Lesions: Evaluation of Breast Ultrasound, MRI Mammography and Electrical Impedance Scanning as Adjunctive Technologies in Breast Cancer Detection. *Clinical Radiology* 56, 278-283 (2001).
7. Ider, Y. Z. and Birgul, O. Use of the Magnetic Field Generated by the Internal Distribution of Injected Currents for Electrical Impedance Tomography (MR-EIT). *Elektrik, Turkish Journal of Electrical Engineering and Computer Sciences* 6, 215-225 (1998).
8. Birgul, O., Eyuboglu, B. M., and Ider, Y. Z. Experimental Results for 2D Magnetic Resonance-Electrical Impedance Tomography (MR-EIT) Using Magnetic Flux Density in One Direction. *Physics in Medicine and Biology* 48, 3485-3504 (2003).
9. Oh, S. H., Han, J. Y., Lee, S. Y., Cho, M. H., Lee, B. I., and Woo, E. J. Electrical Conductivity Imaging by Magnetic Resonance Electrical Impedance Tomography (MREIT). *Magnetic Resonance in Medicine* 50, 875-878 (2003).
10. Khang, H. S., Lee, B. I., Oh, S. H., Woo, E. J., Lee, S. Y., Cho, M. Y., Kwon, O., Yoon, J. R., and Seo, J. K. Jsubstitution Algorithm in Magnetic Resonance Electrical Impedance Tomography (MREIT): Phantom Experiments for Static Resistivity Images. *IEEE Trans. Med. Imaging* 21, 695-702 (2002).
11. Lee, B. I., Oh, S. H., Woo, E. J., Lee, S. Y., Cho, M. H., Kwon, O., Seo, J. K., and Baek, W. S. Static Resistivity Image of a Cubic Saline Phantom in Magnetic Resonance Electrical Impedance Tomography (MREIT). *Physiol. Meas.* 24, 579-589 (2003).
12. Oh, S. H., Lee, B. I., Woo, E. J., Lee, S. Y., Kim, T. S., Kwon, O., and Seo, J. K. Electrical Conductivity Images of Biological Tissue Phantoms in MREIT. *Physiol. Meas.* 26, S279-288 (2005).
13. Muftuler, L. T., Hamamura, M. J., Birgul, O., and Nalcioğlu, O. Resolution and Contrast in Magnetic Resonance Electrical Impedance Tomography (MREIT) and Its Application to Cancer Imaging. *Technology in Cancer Research and Treatment* 3, 599-609 (2004).
14. U. Mikac, F. Demsar, K. Beravs, and I. Sersa. Magnetic Resonance Imaging of Alternating Electric Currents. *Magnetic Resonance Imaging* 19, 845-856 (2001).
15. Baumann, B. B., Wozny, D. R., Kelly, S. K., Meno, F. M. The Electrical Conductivity of Human Cerebrospinal Fluid at Body Temperature. *IEEE Trans. BME* 44, 220-223 (1997).
16. Ackmann, J. J. Complex Bioelectric Impedance Measurement System for the Frequency Range from 5 Hz to 1MHz. *Annl. Biomed. Eng.*, 21, 135-146 (1993).
17. Birgul, O., Eyuboglu, B. M., and Ider, Y. Z. Current Constrained Voltaged Scaled Reconstruction (CCVSR) Algorithm for MR-EIT and Its Performance with Different Probing Current Patterns. *Physics in Medicine and Biology* 48, 653-671 (2003).
18. Stoica, G., Koestner, A., and Capen, C. C. Neoplasms Induced with High Single Doses of N-ethyl-N-nitrosourea in 30-day-old Sprague-Dawley Rats, with Special Emphasis on Mammary Neoplasia. *Anticancer Research* 4, 5-12 (1984).

Received: April 17, 2006; Revised: July 6, 2006;

Accepted: July 6, 2006

Measurement of ion diffusion using magnetic resonance electrical impedance tomography

Mark J Hamamura, L Tugan Muftuler, Ozlem Birgul
and Orhan Nalcioğlu

Tu & Yuen Center for Functional Onco-Imaging, University of California, 164 Irvine Hall, Irvine,
CA 92697-5020, USA

E-mail: markjham@uci.edu

Received 9 February 2006, in final form 10 February 2006

Published 9 May 2006

Online at stacks.iop.org/PMB/51/2753

Abstract

In magnetic resonance electrical impedance tomography (MREIT), currents are applied to an object, the resulting magnetic flux density measured using MRI and the conductivity distribution reconstructed using these MRI data. In this study, we assess the ability of MREIT to monitor changes in the conductivity distribution of an agarose gel phantom, using injected current pulses of 900 μA . The phantom initially contained a distinct region of high sodium chloride concentration which diffused into the background over time. MREIT data were collected over a 12 h span, and conductivity images were reconstructed using the iterative sensitivity matrix method with Tikhonov regularization. The results indicate that MREIT was able to monitor the changing conductivity and concentration distributions resulting from the diffusion of ions within the agarose gel phantom.

(Some figures in this article are in colour only in the electronic version)

1. Introduction

In vitro studies have shown that the electrical conductivity of malignancies may be 20 to 40 times higher than healthy tissues and benign formations (Surowiec *et al* 1988, Jossinet 1998). Therefore, *in vivo* conductivity imaging could aid in the diagnosis and characterization of suspicious lesions. Electrical impedance tomography (EIT) is a conductivity imaging modality that consists of three general steps. A current distribution is established within the object of interest, the effects of these currents are measured, and then these measurement data are used to reconstruct the conductivity distribution within the object. In conventional EIT, surface electrodes are used to inject current into the object and to acquire voltage measurements. This technique is constrained by the physically limited number of measurement electrodes and restriction to surface measurements. As a result, it suffers from poor, non-uniform spatial

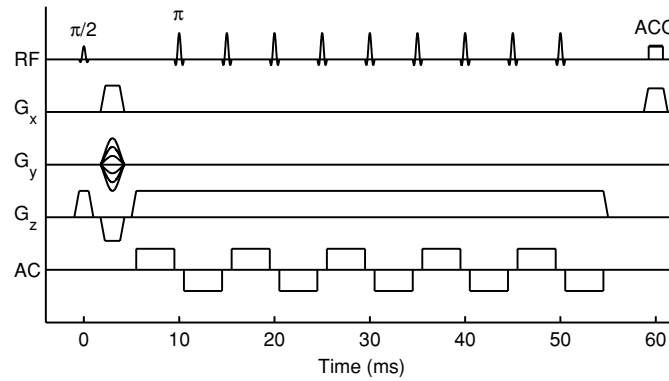


Figure 1. MREIT pulse sequence diagram.

resolution and low sensitivity of the voltages to conductivity changes in the interior regions (Seagar *et al* 1987).

In magnetic resonance electrical impedance tomography (MREIT), MRI is used to measure the effects of applied currents throughout the entire object. These applied currents generate a magnetic flux density, of which the component parallel to the main static field can be measured using an appropriate pulse sequence (Scott *et al* 1991, Ider and Muftuler 1997, Mikac *et al* 2001). Given this single component of current-generated magnetic flux density, several algorithms have been proposed to reconstruct the conductivity distribution. These include the sensitivity matrix method (Ider and Birgul 1998, Birgul *et al* 2003b), $\nabla^2 B_z$ algorithms (Seo *et al* 2003, Ider and Onart 2004) and ∇B_z algorithms (Park *et al* 2004a, 2004b). Several MREIT studies using biological tissue phantoms have been reported (Khang *et al* 2002, Lee *et al* 2003, Oh *et al* 2005). However, these studies focused on reconstructing static conductivity distributions using injected current levels of at least 12 mA. The ability to monitor changes in conductivity over time could provide additional diagnostic information, such as in monitoring tumour growth and treatment. In this study, we assessed the ability of MREIT to monitor changes in conductivity over time using sub-milliamp injected currents more appropriate for human use. Validating this ability is a necessary step towards the imaging and monitoring of human subjects using MREIT.

2. Methods

2.1. Theory

In MREIT, applied currents establish a conductivity-dependent current density distribution within an object, which in turn generates a magnetic flux density according to Ampere's Law. Thus, magnetic flux density measurements contain information about the conductivity distribution. In this study, current pulses of alternating polarity were applied to a test phantom using surface electrodes. For alternating currents, the component of magnetic flux density parallel to the main static field (z -component) can be measured by MRI using a modified spin-echo sequence (Mikac *et al* 2001). The pulse sequence used in this study is shown in figure 1. The current-generated magnetic flux density introduces a phase shift φ in the MR image, given as:

$$\varphi(\mathbf{r}) = 2\gamma NT_{\text{pulse}}B(\mathbf{r}) \quad (1)$$

where γ is the gyromagnetic ratio, N is the number of cycles of injected current such that each cycle consists of one positive and one negative pulse, T_{pulse} is the duration of each pulse, and $B(\mathbf{r})$ is the amplitude of z -component current-generated magnetic flux density at point \mathbf{r} . Measurement of this phase shift allows for calculation of $B(\mathbf{r})$.

For a given set of electrodes used for current injection, data were collected twice, each with opposite polarities in the applied current pulses. The resulting phase maps were subtracted then divided by two, so as to cancel out any additional phase contributions, such as those arising from small imperfections in the hardware timing. A given set of injecting electrodes forms an ‘injection profile’. Data from at least two different injection profiles are required to reconstruct a unique solution (Kwon *et al* 2002). Previous MREIT studies have shown that using just two profiles is sufficient for reconstructing accurate images. This is a significant advantage over conventional EIT, which typically requires the use of several (16 or more) electrodes.

For reconstructing the conductivity distribution from the z -component magnetic flux density data, this study utilized the sensitivity matrix method (SMM). The object domain was discretized into a mesh of first-order triangular elements, chosen for compatibility with the finite element method (Reddy 1993). A linear relationship between conductivity perturbations and z -component magnetic flux density perturbations was then assumed, such that:

$$\Delta B_z = \mathbf{S} \Delta \sigma \quad (2)$$

where \mathbf{S} is known as the ‘sensitivity’ matrix. Given m measurement points and n conductivity elements, ΔB_z is an $m \times 1$ vector, $\Delta \sigma$ is an $n \times 1$ vector, \mathbf{S} is an $m \times n$ matrix, and the matrix element S_{ij} is the change in the i th magnetic flux density measurement due to a small variation in the conductivity of the j th element. An initial conductivity distribution σ_{initial} was assumed (e.g. uniform conductivity), and the problem linearized around this initial condition:

$$B_{\text{final}} - B_{\text{initial}} = \mathbf{S}(\sigma_{\text{final}} - \sigma_{\text{initial}}) \quad (3)$$

where B_{initial} is the z -component magnetic flux density distribution given σ_{initial} and calculated using the finite element method and Biot-Savart law, B_{final} is the MRI measured z -component magnetic flux density, σ_{final} is the actual (unknown) conductivity distribution, and \mathbf{S} is the sensitivity matrix such that:

$$S_{ij} = \left[\frac{\partial B_i}{\partial \sigma_j} \right]_{\sigma=\sigma_{\text{initial}}} \quad (4)$$

In general, \mathbf{S} is an ill-conditioned matrix, so that a simple least-squares fit cannot be used to solve for σ_{final} . In this study, the linear equation was solved using the conjugate gradient method with Tikhonov regularization, where σ_{final} was found by:

$$\min_{\sigma_{\text{final}}} \{ \|\mathbf{S} \Delta \sigma - \Delta B_z\|^2 + \lambda \|\Delta \sigma\|^2 \} \quad (5)$$

where λ is a regularization parameter (Golub *et al* 1999). The regularization parameter λ was chosen such that the calculated z -component magnetic flux density generated by the reconstructed conductivity distribution was closest to the MRI-measured magnetic flux density.

$$\min_{\lambda} \{ \|B_{\text{final}} - [B(\sigma)]_{\sigma=\sigma_{\text{final}}(\lambda)}\| \}. \quad (6)$$

After finding σ_{final} , if the change in conductivity $\Delta \sigma$ was greater than some predefined threshold, then this σ_{final} was assigned as the new, updated σ_{initial} , and the process was iterated.

The SMM reconstructs relative conductivities. Thus, the true conductivity distribution σ_{true} is related to the reconstructed conductivity distribution σ_{final} by a constant scaling factor K :

$$\sigma_{\text{true}} = K \sigma_{\text{final}}. \quad (7)$$

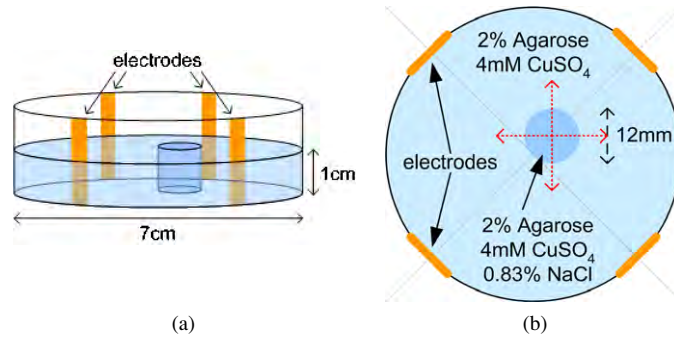


Figure 2. (a) Side view and (b) top view of the phantom used to monitor the diffusion of NaCl.

Determining the absolute conductivity distribution requires an additional constraint, such as a surface voltage measurement (Birgul *et al* 2003a).

2.2. Phantom

The previously outlined methods were used to monitor the conductivity distribution within an agarose gel phantom. The conductivities of several 4 mM CuSO₄ and 2% agarose mixtures with a range of NaCl concentrations from 0% to 1% were measured using the 4-electrode method (Baumann *et al* 1997). Within this range, a linear relationship was found:

$$\sigma = AC + E \quad (8)$$

where the conductivity σ is in units of S m⁻¹, the NaCl concentration C is in units of g/100 ml water, and the constants A and E are 1.7 and 0.074 respectively. For larger NaCl concentrations, the relationship becomes nonlinear (Fuoss and Onsanger 1957).

For the phantom, a hollow acrylic disc with an inner diameter of 7 cm was filled to a thickness of 1 cm with 4 mM CuSO₄ and 2% (g/100 ml water) agarose. Within this disc, a smaller cylindrical region of 12 mm diameter and 1 cm thickness was filled with 4 mM CuSO₄, 2% agarose and 0.83% NaCl. This NaCl concentration was selected using (8) to provide a conductivity contrast of 20 relative to the background. An actual conductivity contrast of 19.7 was found by measuring the prepared gels using the 4-electrode method. The initial mixtures within each of these two regions were assumed to be homogeneous. The phantom was constructed such that within the phantom, the overall concentration distribution did not vary along the z -direction. A schematic of the phantom is shown in figure 2.

To measure the conductivity distribution within the phantom using MREIT, four copper electrodes each 6.35 mm wide were placed equidistant along the inner wall of the acrylic disc and used to inject currents into the interior region (figure 2). Using (7) and (8), measurement of the conductivity distribution was used to map the NaCl concentration distribution. The scaling factor K was determined by applying the constraint that the total amount of NaCl in the phantom remained constant:

$$\int_{\text{phantom}} C \, dv = \text{constant}. \quad (9)$$

Measurements of the conductivity distribution over time were used to monitor the diffusion process occurring within the phantom.

In the phantom's initial state, there existed a distinct region containing NaCl and a background containing no NaCl. Over time, the NaCl diffused from the region of higher concentration to the region of lower concentration as governed by the diffusion equation:

$$\frac{\partial C}{\partial t} = \nabla \cdot D \nabla C \quad (10)$$

where C is the concentration of the diffusing substance and D is the diffusion constant. Due to the geometry of the phantom, there existed no concentration gradient along the z -direction within the phantom. Thus this diffusion process was independent of the z -direction and can be analysed in 2D. For a disc of radius a on an infinite plane surface, the concentration C at radius r and time t is given as:

$$C(r) = \frac{C_i}{2Dt} \exp\left(\frac{-r^2}{4Dt}\right) \int_0^a \exp\left(\frac{-r'^2}{4Dt}\right) I_0\left(\frac{rr'}{2Dt}\right) r' dr' \quad (11)$$

where C_i is the initial uniform concentration of the disc and I_0 is the modified Bessel function of the first kind of order zero (Crank 1975). For a given time $t > 0$, the peak concentration C is located at the centre of the disc, and is given as

$$C = C_i \left(1 - \exp\left(\frac{-a^2}{4Dt}\right)\right). \quad (12)$$

2.3. Experiment

The agarose gel phantom was placed within a 4T MRI scanner with the plane of the disc aligned perpendicular to the main static field. Currents within the phantom were constrained within this plane and the current density distribution contained a negligible z -component. As a result, the current-generated magnetic flux density within the phantom was primarily along the main static field axis. This was ideal since the pulse sequence only detects the z -component of any magnetic flux density. Currents were delivered to the electrodes using thin copper wires. These wires were aligned parallel to the main static field for up to 10 cm away from the phantom, such that the magnetic flux density they generated contained a negligible z -component in the phantom, and thus did not affect the MRI measurements. A current-source circuit was constructed and used to generate the injected currents (Baumann *et al* 1997). Synchronization of the circuit output with the pulse sequence was controlled by the scanner computer through a digital interface.

An MREIT measurement was acquired as soon as possible after preparation of the agarose gel phantom (30 min). Additional measurements were taken at 1 h intervals after phantom preparation for up to 8 h, followed by scans at 10 and 12 h. For each time point, data were collected for two injection profiles, using pairs of electrodes directly opposite of each other (figure 4). Both data sets were used simultaneously in the conductivity reconstruction algorithms. For each injection profile, data were collected using the previously outlined pulse sequence, injecting 5 cycles of current with an amplitude of 900 μA , a pulse length of 3567 μs and a cycle period of 10 ms (figure 1). Other scan parameters were: TR = 500 ms, TE = 60 ms, slice thickness = 5 mm, FOV = 100 mm, matrix = 64 \times 64, NEX = 8. Raw MRI data were exported to a separate computer for processing. Magnetic flux density calculations and reconstruction algorithms utilizing the iterative SMM with Tikhonov regularization were developed using MATLAB. For reconstruction, a circular finite element mesh with 1089 nodes and 2048 triangular elements was utilized, as shown in figure 3(a). For each timepoint, the reconstruction was iterated until successive iterations resulted in not more than a 1% change in the peak conductivity value.

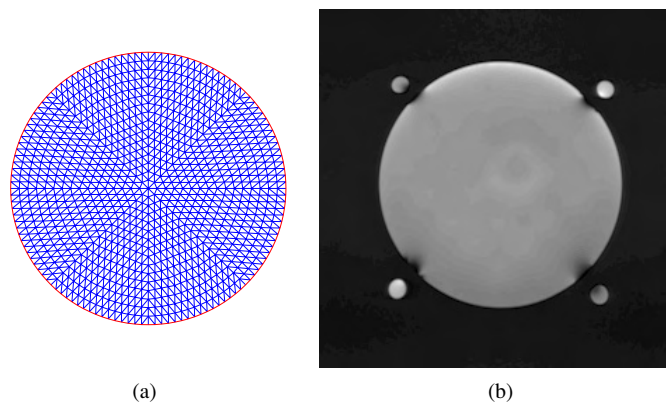


Figure 3. (a) Finite element mesh used for reconstruction. (b) Spin echo image of the phantom. The smaller circular markers around the periphery were used to locate the electrodes during reconstruction.

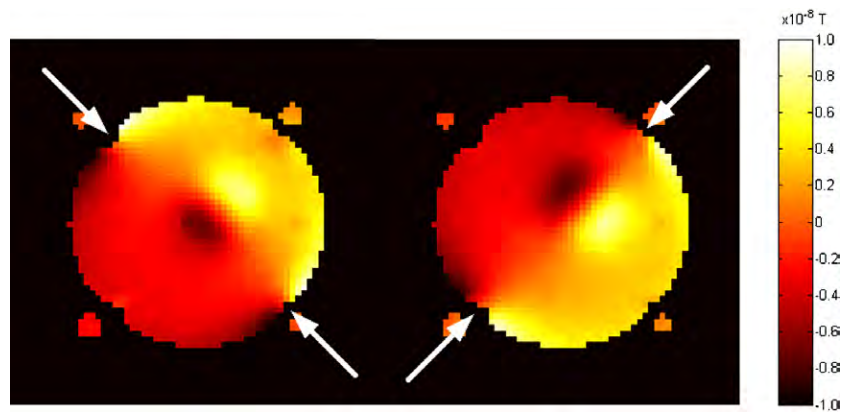


Figure 4. Reconstructed z -component magnetic flux density distributions at the first time point for the two injection profiles. The white arrows indicate the location of the current injecting electrodes.

3. Results

Figure 3(b) shows the MR magnitude image of the phantom taken using a standard spin-echo sequence just after at the first time point. The scan parameters were: $TR = 1$ s, $TE = 20$ ms, slice thickness = 5 mm, $FOV = 100$ mm, matrix = 256×256 , $NEX = 2$. Despite two distinct regions of different NaCl concentrations, there is little contrast in this image.

Figure 4 shows the calculated z -component magnetic flux density at the first time point for the two injection profiles. Figure 5 shows the reconstructed conductivity images, obtained by processing the magnetic flux density data with the iterative SMM with Tikhonov regularization. Unlike the MR magnitude image, these conductivity images show a clear contrast between regions of different NaCl concentrations. For each time point, the spatial profile centred on the initial high NaCl concentration region was calculated by averaging the radial profiles taken along four different directions as shown by the red dotted lines in figure 2(b). The resulting curves are plotted in figure 6. Over time, the higher conductivity region broadened

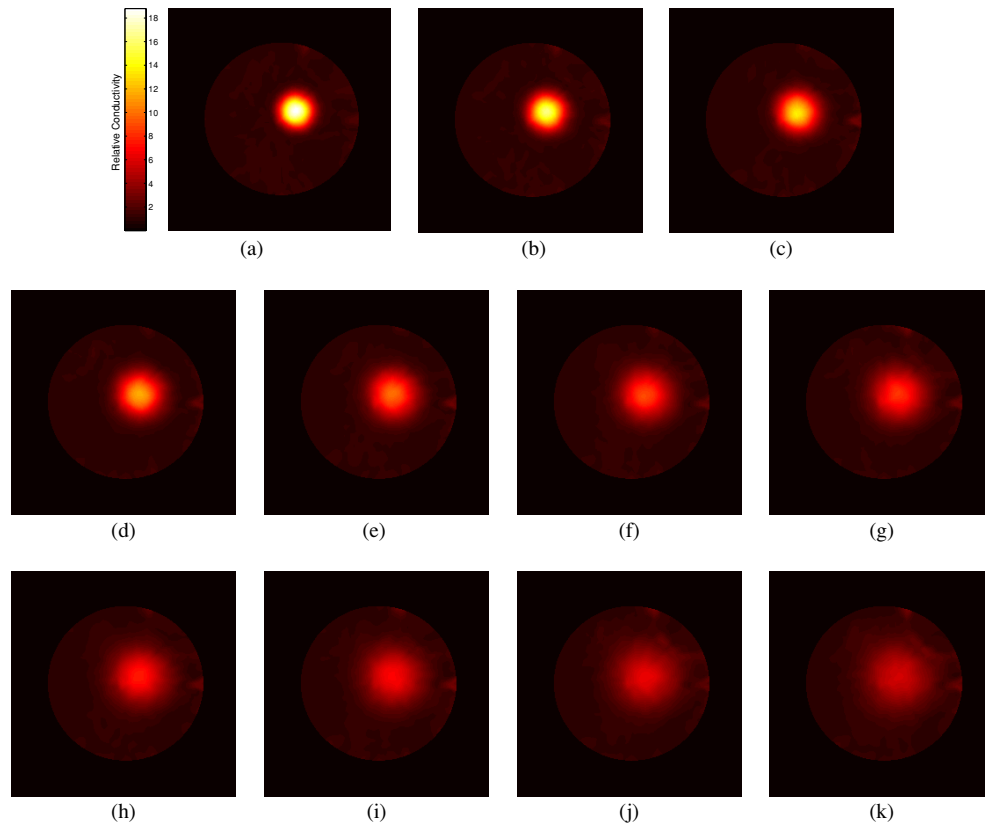


Figure 5. Reconstructed conductivity distribution (a) 30 min, (b) 1 h, (c) 2 h, (d) 3 h, (e) 4 h, (f) 5 h, (g) 6 h, (h) 7 h, (i) 8 h, (j) 10 h and (k) 12 h after phantom preparation.

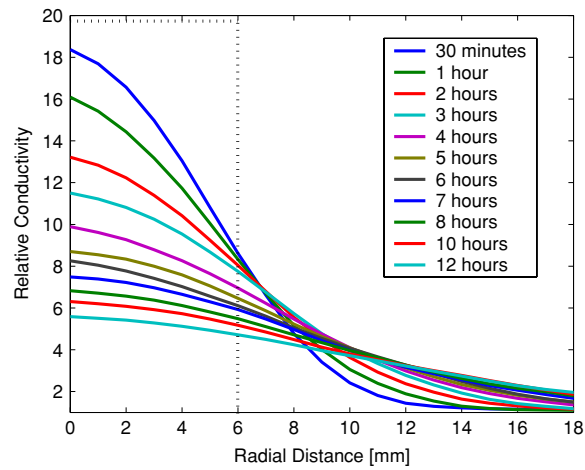


Figure 6. Comparison of the spatial profiles of the inner disc. The initial profile at $t = 0$ is denoted by the dotted line.

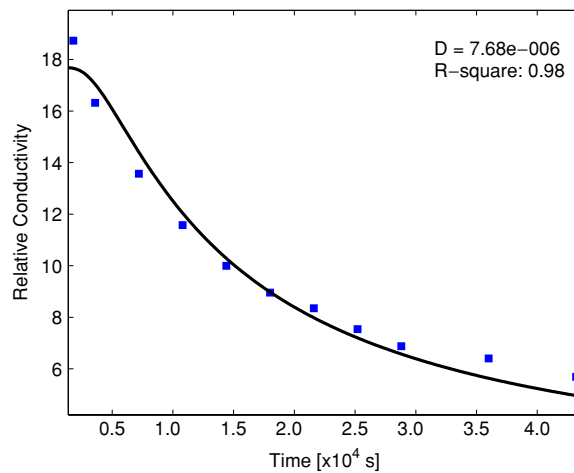


Figure 7. Decay of the peak conductivity. Reconstructed values denoted by the blue squares were fitted to (12) resulting in the black curve.

and decreased in magnitude, and the border between initial regions became less distinct. The change in the conductivity distribution is consistent with the diffusion of NaCl from the initial disc region into the background.

To quantify this diffusion, the peak conductivity value for each time point was scaled using (9) then fitted to (12) using the Curve Fitting Toolbox of MATLAB. The results are shown in figure 7. The peak values appear to coincide with the theoretical curve, indicating that the changing reconstructed conductivity distributions over time can be attributed to the diffusion process. An experimental diffusion constant of $D = 7.68 \times 10^{-6} \text{ cm}^2 \text{ s}^{-1}$ was obtained.

4. Discussion

The previous results indicate that MREIT was able to monitor the changing conductivity distribution resulting from the diffusion of ions within the agarose gel phantom. The experimentally determined diffusion constant is 45% smaller than the previously reported measurement of $1.4 \times 10^{-5} \text{ cm}^2 \text{ s}^{-1}$ by Schantz and Lauffer (1962). However, their study investigated NaCl in an estimated 1.5% agarose gel, which can in part explain their faster diffusion. The smaller diffusion constant for the MREIT phantom can also be attributed to its finite shape and confined volume. Equation (11) assumes that diffusion occurs on an infinite plane. In a restricted area, NaCl can accumulate, which decreases the apparent rate of diffusion.

In using the SMM, only relative changes in conductivity can be found. However, in monitoring the phantom, only contrasts in conductivity were required to observe the ion diffusion. In applications such as tumour characterization, differences in conductivity between suspicious lesions and surrounding background tissue may be more significant than absolute conductivity values.

While data were collected every hour, shorter time resolutions are possible and limited by the rate at which data can be acquired. For the scan parameters used in this study, data for one injection profile were collected in under 5 min. In addition to shorter time periods, MREIT should also be able to monitor changes in conductivity over periods much larger than

that used in this study. Such extended durations would be useful when monitoring tumour growth and assessing response to treatment. For example, MREIT could be used to evaluate a patient's response to chemotherapy by measuring the (changing) conductivity of a suspicious lesion over several weeks.

Application of MREIT to human studies has seemed unpractical due to the large amounts of injected currents utilized in previous studies. Lower current levels result in a decrease in the signal-to-noise ratio (SNR) of the acquired magnetic flux density maps used in the reconstruction process. Oh *et al* (2005) recently acquired conductivity images of a biological tissue phantom in a 3T MRI system using the harmonic B_z algorithm. Their results show significant degradation in the reconstruction at as high as 12 mA of injected current. This is largely due to the use of the derivative operator on the magnetic flux density measurements, which amplifies errors from noise. Other reported biological tissue phantom studies utilizing gradient-based reconstruction methods used currents in excess of 24 mA. The results of this study demonstrate that MREIT is possible for injected currents as low as 900 μ A. The SMM appears significantly more robust when reconstructing lower SNR data. Future work will search for the minimum levels of current needed for reconstructing accurate conductivity images.

Due to the geometry of the diffusion phantom, currents were restricted to flow within a slab of 1 cm thickness. In more intricate objects such as the human body, currents may flow throughout the entire object. Such 3D current flow will result in a decrease in the measurable magnetic flux density. The corresponding reduction in the SNR presents an additional challenge. To improve the SNR without increasing the injected current level, future work will optimize hardware and pulse sequence parameters. Use of a reconstruction algorithm capable of processing lower SNR data, such as the SMM, is also critical. The SMM has already been applied by Muftuler *et al* (2004) in reconstructing the conductivity distribution of an *in vivo* rat using 1 mA of injected current.

The maximum level of current that can safely be applied to humans depends on the frequency. In general, the safe current limit increases as the frequency increases. A majority of previously reported MREIT studies have utilized single cycle, long current pulses, essentially classifying them as dc with regards to safety standards. This study utilized alternating current in the form of multiple cycles of shorter alternating polarity pulses, with a cycle period of 10 ms (primary frequency component of 100 Hz). While safety levels at 100 Hz are only slightly higher than dc, the concept of using ac over dc has the advantage that future studies using higher frequencies will allow for safe application of larger current levels. Use of higher frequencies will also enhance the capacitive contributions to overall impedance, thus providing an additional source of information that may be of diagnostic relevance. Future work will test this pulse sequence and develop new pulse sequences for use in higher frequency MREIT.

5. Conclusions

By utilizing NaCl diffusion in an agarose gel phantom, we were able to demonstrate the ability of MREIT to monitor changes in an object's conductivity distribution over time. An injected current level of 900 μ A was found acceptable for reconstructing accurate images when utilizing the iterative sensitivity matrix method with Tikhonov regularization. This is approaching the safe current levels for application in humans. The results of this study indicate that human MREIT should be feasible in the near future, and that this modality can be used not only for acquiring static images, but also used for performing dynamic studies.

Acknowledgments

This study was supported in part by grants NIH/NCI R01 CA114210, DOD DAMD17-02-1-0326, and DOD W81XWH-04-1-0446a.

References

- Baumann S B, Wozny D R, Kelly S K and Meno F M 1997 The electrical conductivity of human cerebrospinal fluid at body temperature *IEEE Trans. Biomed. Eng.* **44** 220–3
- Birgul O, Eyuboglu B M and Ider Y Z 2003a Current constrained voltage scaled reconstruction (CCVSR) algorithm for MR-EIT and its performance with different probing current patterns *Phys. Med. Biol.* **48** 653–71
- Birgul O, Eyuboglu B M and Ider Y Z 2003b Experimental results for 2D magnetic resonance electrical impedance tomography (MR-EIT) using magnetic flux density in one direction *Phys. Med. Biol.* **48** 3485–504
- Crank J 1975 *The Mathematics of Diffusion* (New York: Oxford University Press)
- Fuoss R M and Onsager L 1957 Conductance of unassociated electrolytes *J. Phys. Chem.* **61** 668–82
- Golub G H, Hanse P C and O’Leary D P 1999 Tikhonov regularization and total least squares *SIAM J. Matrix Anal. Appl.* **21** 185–94
- Ider Y Z and Birgul O 1998 Use of the magnetic field generated by the internal distribution of injected currents for electrical impedance tomography (MR-EIT) *Elektrik* **6** 215–25
- Ider Y Z and Muftuler L T 1997 Measurement of AC magnetic field distribution using magnetic resonance imaging *IEEE Trans. Med. Imaging* **16** 617–22
- Ider Y Z and Onart S 2004 Algebraic reconstruction for 3D magnetic resonance-electrical impedance tomography (MREIT) using one component of magnetic flux density *Physiol. Meas.* **25** 281–94
- Jossinet J 1998 The impedivity of freshly excised human breast tissue *Physiol. Meas.* **19** 61–75
- Khang H S, Lee B I, Oh S H, Woo E J, Lee S Y, Cho M Y, Kwon O, Yoon J R and Seo J K 2002 J-substitution algorithm in magnetic resonance electrical impedance tomography (MREIT): phantom experiments for static resistivity images *IEEE Trans. Med. Imaging* **21** 695–702
- Kwon O, Woo E J, Yoon J R and Seo J K 2002 Magnetic resonance electrical impedance tomography (MREIT): simulation study of J-substitution algorithm *IEEE Trans. Biomed. Eng.* **49** 160–7
- Lee B I, Oh S H, Woo E J, Lee S Y, Cho M H, Kwon O, Seo J K and Baek W S 2003 Static resistivity image of a cubic saline phantom in magnetic resonance electrical impedance tomography (MREIT) *Physiol. Meas.* **24** 579–89
- Mikac U, Demsar F, Beravs K and Sersa I 2001 Magnetic resonance imaging of alternating electric currents *Magn. Reson. Imaging* **19** 845–56
- Muftuler L T, Hamamura M, Birgul O and Nalcioğlu O 2004 Resolution and contrast in magnetic resonance electrical impedance tomography (MREIT) and its application to cancer imaging *Technol. Cancer Res. Treat.* **3** 599–609
- Oh S H, Lee B I, Woo E J, Lee S Y, Kim T S, Kwon O and Seo J K 2005 Electrical conductivity images of biological tissue phantoms in MREIT *Physiol. Meas.* **26** S279–88
- Park C, Kwon O, Woo E J and Seo J K 2004a Electrical conductivity imaging using gradient B_z decomposition algorithm in magnetic resonance electrical impedance tomography (MREIT) *IEEE Trans. Med. Imaging* **23** 388–94
- Park C, Park E J, Woo E J, Kwon O and Seo J K 2004b Static conductivity imaging using variational gradient B_z algorithm in magnetic resonance electrical impedance tomography *Physiol. Meas.* **25** 257–69
- Reddy J N 1993 *An Introduction to the Finite Element Method* (New York: McGraw-Hill)
- Schantz E J and Lauffer M A 1962 Diffusion measurements in agar gel *Biochem.* **1** 658–63
- Scott G C, Joy M L G, Armstrong R L and Henkelman R M 1991 Measurement of nonuniform current density by magnetic resonance *IEEE Trans. Med. Imaging* **10** 362–74
- Seagar A D, Barber D C and Brown B H 1987 Theoretical limits to sensitivity and resolution in impedance imaging *Clin. Phys. Physiol. Meas.* **8** A13–31
- Seo J K, Yoon J R, Woo E J and Kwon O 2003 Reconstruction of conductivity and current density images using only one component of magnetic field measurements *IEEE Trans. Biomed. Eng.* **50** 1121–4
- Surowiec A J, Stuchly S S, Barr J R and Swarup A 1988 Dielectric properties of breast carcinoma and the surrounding tissues *IEEE Trans. Biomed. Eng.* **35** 257–63

Resolution And Contrast In Magnetic Resonance Electrical Impedance Tomography (MREIT) and its Application To Cancer Imaging

www.tcrt.org

It has been reported that the electrical impedance of malignancies could be 20-40 times lower than healthy tissues and benign formations. Therefore, *in vivo* impedance imaging of suspicious lesions may prove to be helpful in improving the sensitivity and specificity of detecting malignant tumors. Several systems have been developed to map the conductivity distribution inside a volume of tissue, however they suffer from poor spatial resolution because the measurements are taken only from surface electrodes. MRI based impedance imaging (MREIT) is a novel method, in which weak electrical currents are injected into the tissue and the resulting perturbations in the magnetic field are measured using MRI. This method has been shown to provide better resolution compared to previous techniques of impedance imaging because the measurements are taken from inside the object on a uniform grid. Thus, it has the potential to be a useful modality that may detect malignancies earlier. Several phantom imaging experiments were performed to investigate the spatial resolution and dynamic range of contrast of this technique. The method was also applied to a live rat bearing a R3230 AC tumor. Tumor location was identified by contrast enhanced imaging.

Key words: Electrical Impedance Tomography, MRI, Cancer imaging.

Introduction

Breast cancer is the leading cause of cancer deaths among women in many parts of the world and currently no single imaging modality has both high sensitivity and specificity for the diagnosis of breast cancer. At present, well-established breast screening methods have high sensitivity but suffer from poor specificity. X-ray mammography, which is accepted as the gold standard for breast cancer screening, provides high sensitivity but has a high rate of false-positives (2-4). Similarly, the sensitivity of breast MRI can be very high, however the specificity for the detection of abnormalities is variable (5, 6). In addition to the high rate of false positives, some of these techniques also fail to detect breast cancer in some cases, such as patients with dense breast tissue, which is common among younger patients, and patients undergoing hormone replacement therapy during post-menopausal period (7). New imaging modalities with better specificity may help reduce the rate of false positives, hence eliminate unnecessary biopsies.

L. Tugan Muftuler, Ph.D.*
Mark Hamamura, M.Sc.
Ozlem Birgul, Ph.D.
Orhan Nalcioglu, Ph.D.

Tu & Yuen Center for
Functional Onco-imaging
164 Irvine Hall
University of California
Irvine CA 92697

* Corresponding Author:
L. Tugan Muftuler
Email: muftuler@uci.edu

Abbreviations: MRI, Magnetic Resonance Imaging; EIT, Electrical Impedance Tomography; MREIT, Magnetic Resonance Electrical Impedance Tomography; FEM, Finite Element Method; EIS, Electrical Impedance Scanning; OPAMP, Operational Amplifier; SVD, Singular Value Decomposition; NEX, Number of Excitations; CE-MRI, Contrast Enhanced MRI.

It has been shown that electrical properties of malignant tissues are significantly different from those of normal and benign tissues. Surowiec *et al.* (1) have reported that the electrical impedance of malignant tumors decreases by a factor of 20 to 40 with respect to normal or benign tissues. This information may be used in tumor detection and characterization. Therefore, the spatial distribution of conductivity measurements (which is inversely related to impedance) can be used in conjunction with other imaging modalities to identify tumors and achieve higher specificity rates compared to the currently used techniques.

Electrical Impedance Scanning (EIS) is a new technique recently introduced to aid in the diagnosis of malignant breast tumors (12-15, 26). The device that uses this technique generates a map of the conductivity distribution inside the breast tissue. This device received FDA approval recently and has been introduced to the market (15). A probe that comprises of an array of electrodes is placed over the breast and small amounts of current are injected into the tissue through another electrode placed in the palm of the patient. The magnitude and phase of the current is measured at one electrode at a time and all electrodes are scanned sequentially. Using the distribution of electric currents in this electrode array, a conductivity map is reconstructed; but it does not provide tomographic images. Therefore, the conductivity maps reconstructed using this technique have poor spatial resolution and the spatial resolution is not uniform throughout the imaging region. The generated maps of conductivity are insensitive to tumors deep inside the breast, which are located 3-3.5cm away from the surface. Moreover, tumors just under the nipple are confounded by the high conductivity of the nipple.

Electrical Impedance Tomography (EIT) was developed in the 1980s to reconstruct the conductivity distribution inside a conducting volume. In this method, a current distribution is generated inside the object by injection or induction and peripheral voltage measurements are acquired using limited number of surface electrodes to find the internal conductivity distribution (8). This method also suffers from poor spatial resolution due to the limited number of voltage measurements taken only from the surface. This imaging technique is also less sensitive to conductivity changes deep inside the object. Cherepenin *et al.* (9) have recently investigated the potential of this technique in breast cancer detection. They have developed an improved EIT system with 256 electrodes placed on a planar surface for improved spatial resolution. They collected *in vivo*, multi-slice tomographic impedance images of healthy and cancerous breasts. Two remote electrodes were placed on patient's extremities for current injection and voltage reference. This allowed using the assumption of spherical equipotential surfaces near the electrode array. Filtered backprojection along these equipotential surfaces were used for fast 3D image reconstruction. This

device measured only the magnitude of voltage measurements, so the phase information was ignored. This setup helped improve image quality and they were able to detect high conductivity tumor formations of 3-5 cm in size. However, the system still lacks high resolution to detect tumors less than a few centimeters. Moreover, the electrodes with bad contacts cause significant image artifacts. They developed a thresholding technique to detect such electrodes and discard information from them.

Estrela *et al.* (10), and Kerner *et al.* (11) have studied electrical properties of breast tumors using an EIT system in which both the magnitude and phase of input current and surface voltage measurements were recorded. Sinusoidal input currents were applied where the frequency was changed between 10KHz up to about 1MHz in discrete steps. This allowed imaging both conductivity and permittivity of breast tissues. Typically, 16 surface electrodes were used that were placed on a circular ring, which resulted in lower spatial resolution compared to (9). However, it was noted that permittivity information was more useful compared to their conductivity counterparts in detecting malignancies.

MREIT is a recently developed method for conductivity imaging (16-21). It uses the magnetic flux density measurements acquired from MR phase images to reconstruct conductivity. Magnetic flux density generated by applied currents can be measured with high spatial resolution using MRI. Various techniques have been proposed for DC (22), AC (23, 24), and RF (25) currents. Unlike EIT, the spatial resolution in the MREIT is position independent. However, it should be noted that only the component of the magnetic flux density in the direction of the main field of the MRI system can be measured. Therefore, one must develop a technique to solve the inverse problem of finding the conductivity or current density from only one component of magnetic flux density. With this technique, only the relative conductivity values can be reconstructed from using only the magnetic flux density measurements. In order to find the absolute conductivity values, at least one voltage measurement from the boundary is required. The reconstruction algorithms can also be divided into two groups depending on the data type required. The first group uses magnetic flux density directly, whereas in the second one, the current density distribution is required in image reconstruction. Algorithms that use current density distribution requires the measurement of all three components of the magnetic flux density, thus rotation of the object inside the magnet is required. All three orthogonal components of the magnetic field have to be measured in order to calculate the current density or precise conductivity distribution. However, this is not a practical situation, especially for human subjects. Rotation would also introduce problems with registration of measurements taken at different orientations of any object under investigation.

Thus, a method that uses only the z-component of the magnetic field to calculate the conductivity distribution (16, 20) was adopted in this study. This method assumes a linear relationship between the measured magnetic fields and relative conductivity perturbations.

In the presented study, the MREIT technique was tested on various conductivity phantoms to investigate its spatial resolution, signal-to-noise ratio (SNR) and contrast-to-noise ratio (CNR). Various phantoms were built with agarose gels mixed with NaCl to create compartments with known conductivity distributions. Preliminary data was also collected *in vivo* from Sprague-Dawley rats inoculated with the R3230 AC tumor. Contrast Enhanced MRI images were also collected to localize the tumor and investigate the spatial correlation between the outcomes of the two techniques.

Materials and Methods

Data were collected by a 4T whole body MRI system that has a Magnex magnet (Magnex Scientific Inc., UK) equipped with a whole body gradient coil set (Tesla Eng. UK), which provides up to 3G/cm gradient fields. The clear bore size of the magnet with gradient assembly is 650mm. A 13 channel room-temperature high-order shim system with MXA-13-4 shim power supply (Resonance Research, Billerica, MA) is also available to minimize field inhomogeneities. This system is interfaced with a MRRS console (Magnetic Resonance Research Systems, Guildford, UK) that has broadband RF transmit and receive channels. A 16 leg, quadrature, high-pass birdcage coil with 10 cm diameter and 18 cm length was designed and built in-house for the MREIT experiments.

Pulse Sequence

The pulse sequence used for the MREIT experiments is similar to a fast spin echo sequence, where a train of 180° RF pulses is applied following a 90° RF pulse (Fig. 1). However, no phase encode or read-out gradients were applied between the 180° RF pulses and the data was collected with a single read-out gradient only after the last 180° RF pulse. Burst sine wave currents were injected into the object during the RF pulse train where each 180° RF pulse was applied at the zero crossing of the sine waves. The duration of each 180° RF pulse was 1.3ms. A similar sequence was proposed by Mikac *et al.* to obtain image of electric currents inside an object (24).

The z-component of magnetic field (parallel to the main static field) generated by the injected currents introduces a phase shift that accumulates over each half-cycle of the sine wave. The simplified MRI signal equation is given as:

$$s(u,v) = \iint M(x,y) e^{j\theta(x,y)} e^{j(xu + yv)} e^{j\gamma \int_0^t b(x,y) \cos(\omega t) dt} dx dy \quad [1]$$

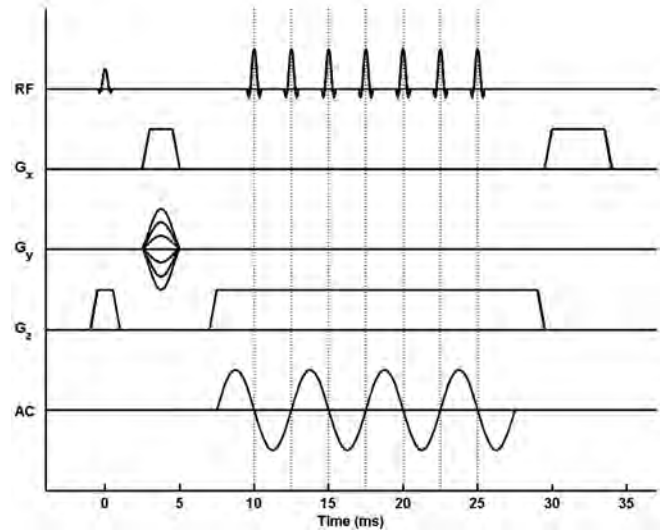


Figure 1: Timing diagram of the pulse sequence used in the MREIT experiments.

$M(x,y)$ is proportional to the density of protons within a voxel at coordinates (x,y) . The phase angle $\theta_{(x,y)}$ accounts for all the constant phase terms including static field inhomogeneity and other hardware related phase delays. The gyromagnetic ratio is shown by γ , and u and v in this equation are called the “spatial frequencies”. They are defined as $u=\gamma \cdot G_x \cdot T_{Gx}$ and $v=\gamma \cdot G_y \cdot T_{Gy}$, where T_{Gx} and T_{Gy} represent the duration of the gradient pulses G_x and G_y , respectively. Therefore, in the final image the accumulated total phase at a pixel at location (x,y) due to the magnetic field generated by injected currents is:

$$\varphi(x,y) = 4 \cdot \gamma \cdot N \cdot b(x,y) / \omega \quad [2]$$

where N is the number of cycles of injected current, $b(x,y)$ the amplitude of the z-component current-generated magnetic field at point (x,y) , and ω the angular frequency of the injected current. Hence, measurement of this phase shift allows for calculation of the (z-component) magnetic field distribution.

During the experiments, the data was collected twice with opposite polarities of electric current, hence changing the polarity of current-generated magnetic field distribution. When resulting phase terms were subtracted, those coming from the static field inhomogeneities and delays in MRI hardware were eliminated, leaving only the terms caused by $b(x,y)$. To obtain the magnetic field distribution $b(x,y)$ from the acquired data, the MRI images were first reconstructed using the FFT. The resulting phase terms from the two sets of images were subtracted. Then, the magnetic field term was calculated using the expression given in Equation [2].

Hardware: An HP ESG-4400B signal generator produced the sine waves. These signals were synchronized to the

Phantom Experiments

A series of phantom studies were conducted to test the spatial resolution and dynamic range of contrast for MREIT. Several agarose gel phantoms with different conductivity distributions were prepared for the tests. The gels were placed inside an acrylic cylinder with an inner diameter of 7cm and height of 1cm. The conductive gels consisted of 2% (g/100mL) agarose and varying concentrations of NaCl. During imaging, the axis of the cylinder was placed parallel to the z-axis (direction of the MRI magnetic field). Four electrodes made of copper foil, each 3mm wide, were placed at 0°, 90°, 180° and 270° along the inner wall and used to inject currents into the interior region. For each phantom, data were collected twice for two current injection schemes and used simultaneously in conductivity reconstruction. The first time, current was injected between the electrodes at 0° and 180°, and the second time between the ones at 90°, and 270°. In the preliminary studies conducted, it has been empirically verified that this scheme improves the sensitivity and spatial resolution compared to using a single pair of electrodes. In all phantom studies, current carrying wires were placed precisely in the z-direction to eliminate any contribution from the currents flowing in those wires. Wires were mounted on acrylic support beams for rigidity and several RF chokes and low pass filters were placed along these wires to suppress RF coupling.

For contrast studies, a 16mm diameter inner disk of gel surrounded by a background of 1% NaCl was used. Two experiments were carried out with two similar contrast phantoms, where the inner disk contained either 4% or 10% NaCl. In the preliminary tests, it has also been experimentally verified that conductance scales sufficiently linearly with NaCl concentration. Therefore, the conductivity contrast values were approximately 1:4 and 1:10, respectively.

To study spatial resolution, two different phantoms were imaged. The first phantom was prepared by placing two hollow nylon disks (each 16mm in diameter) inside the larger disk. They were separated by 17mm center to center. The nylon shells acted as insulators, and each small disk was filled with the same gel as the surrounding background. The second phantom was prepared with the same geometry as the first one but this time the inner disks were agar gels with a conductivity ten times higher than the background.

For each phantom configuration, two separate data sets were collected by injecting 6 cycles of 2mA or 4mA (rms) 200Hz current into the phantom. All data were collected using the previously outlined pulse sequence with the following parameters: TR=500ms, TE=40ms, slice thickness=1cm, FOV=10cm, data matrix 64 × 64 and NEX=8. A single slice was collected for each experiment. The z-component of cur-

rent-generated magnetic field distributions were calculated from the resulting data and the conductivity distributions computed using the method outlined above.

Effect of Initial Conductivity Estimate

As described in the methods section, conductivity reconstruction requires an initial estimate of conductivity distribution. We performed simulation studies to investigate the effect of this initial estimate on reconstructed conductivity and contrast. Four cylindrical phantoms were generated, each with a small disc inside, which was placed off-center. All four phantoms were generated with a background conductivity of 0.002S/cm and the conductivity of the small disk was assigned either 0.5, 2, 4 or 10 times the background conductivity.

Each of the four phantom data were reconstructed three times with uniformly distributed initial conductivity estimates of 0.001S/cm, 0.002S/cm and 0.004S/cm, respectively. Singular values below 1% were truncated and 1089 nodes and 2048 first order triangular elements were used in all finite element models used in reconstructions.

Animal Experiments

An MREIT experiment was also performed for *in vivo* impedance imaging of a tumor-bearing rat. For this purpose, a special animal holder was prepared from acrylic sheets. This holder helped keep the animal stationary during imaging. It also allowed for the placement of the electrodes in consistent positions for longitudinal studies. Electrodes were placed on acrylic hollow tubes filled with CuSO₄ solution to detect the electrode positions precisely in the images. Initial experience has shown that the precise localization of electrode positions is essential for accurate reconstruction of impedance images. Current carrying wires ran along these tubes, which were in z-direction. This is essential to minimize interference from the magnetic fields generated by current in the wires. Prior to imaging, the animal was anesthetized by IV injection of ketamine and xylazine and then placed inside the holder. The electrodes were covered with a thin layer of conductive gel to provide good electrical contact. The skin areas of contact were shaved for better conductance.

An anatomical image was collected using FSE sequence prior to the MREIT images. A single slice with 6mm thickness was collected from the same anatomical location as the MREIT image. The data matrix was 256 × 256, FOV=10cm, TR=4s, TE=20ms/100ms NEX=4. MR-EIT images were collected using the previously outlined pulse sequence with TR=500ms, TE=30ms, NEX=8 (signal averages), 64 × 64 data matrix, FOV=10cm, slice thickness=6mm, with an AC current of 1mA peak, 200Hz, 4 cycles.

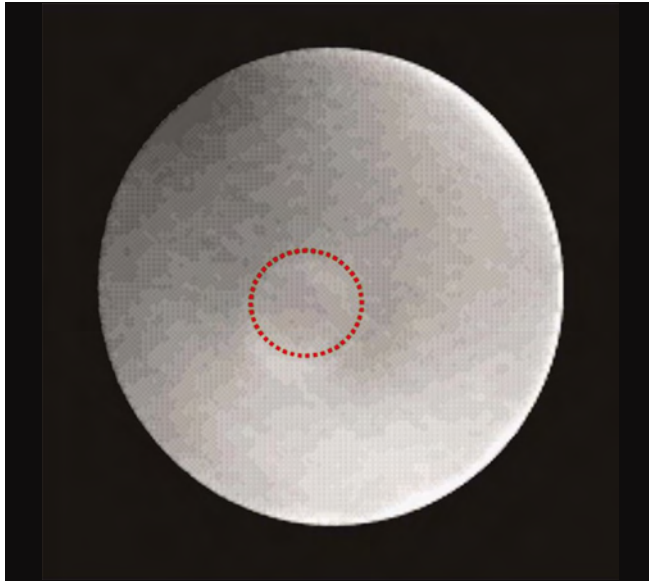


Figure 3a: Spin-Echo image of 1:4 contrast phantom. The higher conductivity region is marked with red dashed lines and it is barely distinguishable in the MR image.

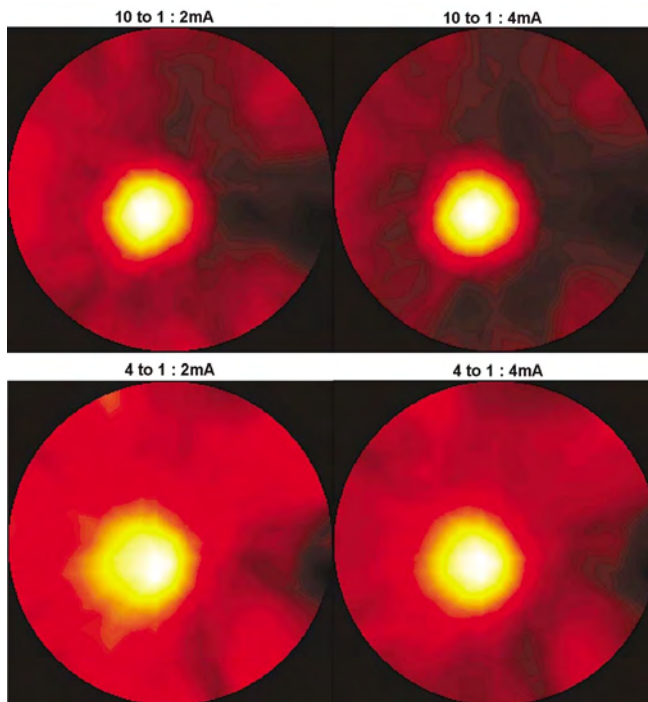


Figure 3b: Conductivity images of 1:10 contrast (top row) and 1:4 contrast (bottom row) with 2mA and 4mA current injection cases.

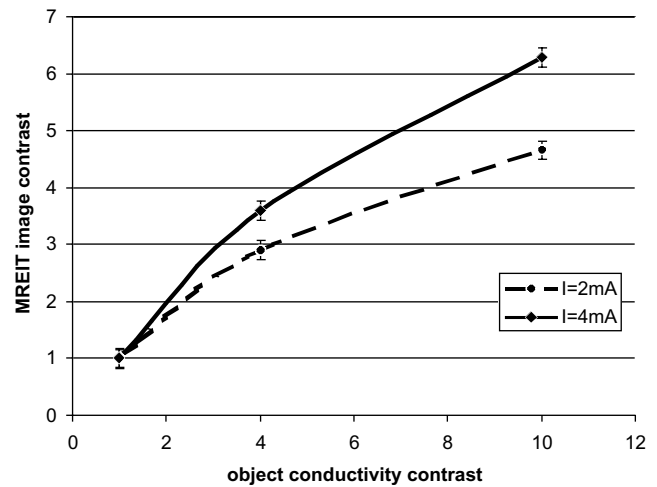


Figure 3c: Plots of *reconstructed conductivity ratio* versus *actual conductivity ratio* obtained from MREIT images. Plots are given for both of the injected current amplitudes. Error bars are also included in these plots.

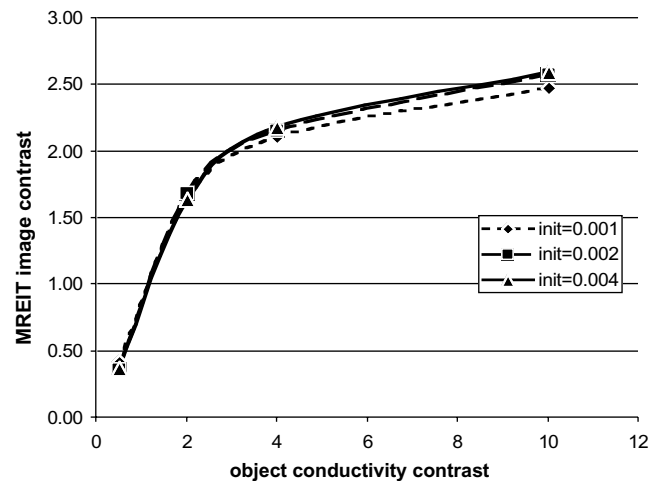


Figure 3d: Plots of *reconstructed conductivity ratio* versus *actual conductivity ratio* in the phantom data used in MREIT simulations. Three plots are given for three different initial conductivity estimates of 0.001, 0.002 and 0.004S/cm. Actual background conductivity was given as 0.002S/cm.

Table I

Mean and standard deviation of relative conductivity (σ_{ir} , σ_{or}) values in contrast phantoms calculated by the MREIT method. Results are reported for both injected current amplitudes.

	$\sigma_o:\sigma_i = 1:4$ phantom (m \pm std)		$\sigma_o:\sigma_i = 1:10$ phantom (m \pm std)	
	I=2mA	I=4mA	I=2mA	I=4mA
Inside small disk (σ_{ir})	235.4 \pm 10.5	229.6 \pm 18.4	233.4 \pm 15.4	226.6 \pm 21.2
Background (σ_{or})	81.2 \pm 18.3	63.8 \pm 14.7	50.1 \pm 17.9	36.1 \pm 12.3

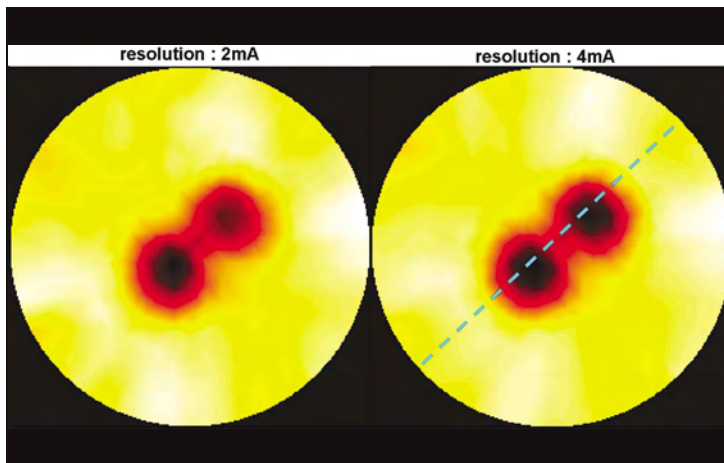


Figure 4a: Conductivity images of resolution phantom with insulating discs. Both, 2mA and 4mA current injection cases were shown. Small, dark circular areas show high resistance compartments (insulating discs).

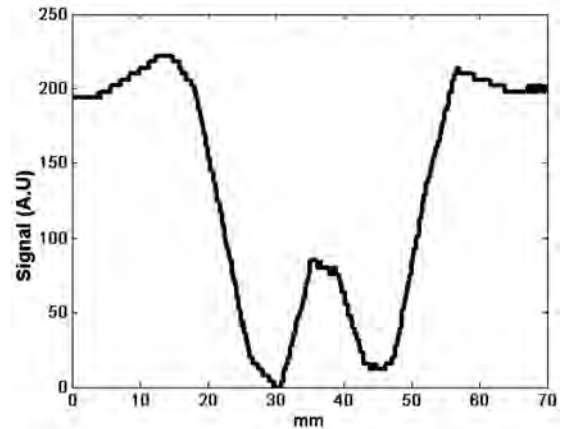


Figure 4b: A profile taken diagonally from the conductivity image of the first resolution phantom going through the centers of the small disks. This profile is given for the 4mA current injection case and the location is shown with blue dashed line in Figure 4a.

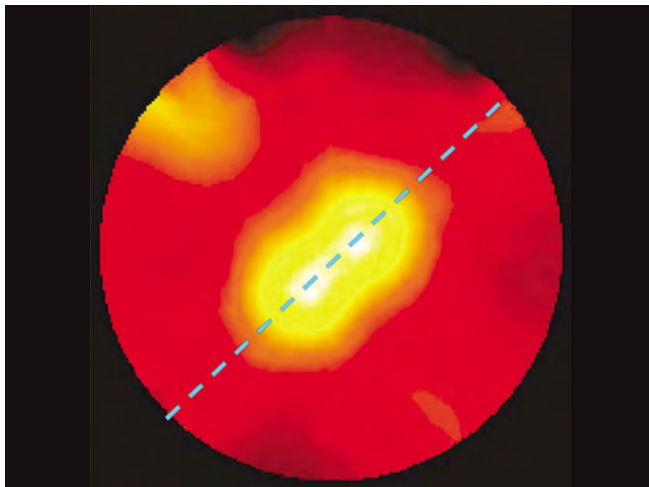


Figure 4c: Conductivity images of resolution phantom with high conductivity discs. Only the 4mA current injection case is shown. Yellow-white circular areas show low resistance compartments.

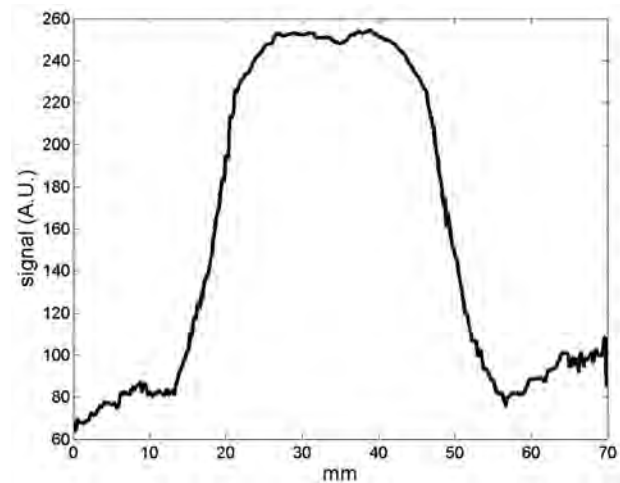


Figure 4d: A profile taken diagonally from the conductivity image of the second resolution phantom shown in Figure 4c.

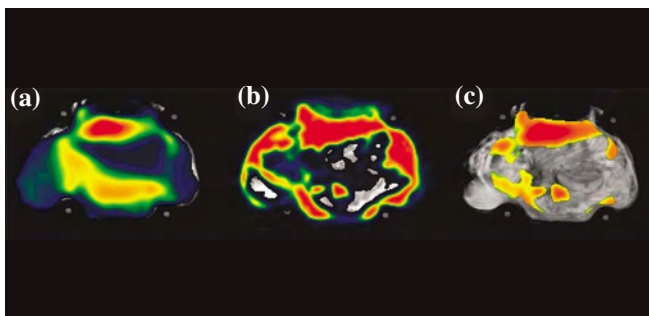


Figure 5: Axial slices from an SD rat inoculated with a R3230 AC tumor showing: (a) Conductivity; (b) CE-MRI; and (c) spatial correlation of CE-MRI and MREIT. The tumor had spread to multiple foci surrounding the body. In (a), red shows high conductivity and blue shows low conductivity regions; whereas red regions in (b) shows enhancement by Gd-DTPA. Areas that have both high conductivity and also enhanced by contrast agent are shown in hot colors in (c).

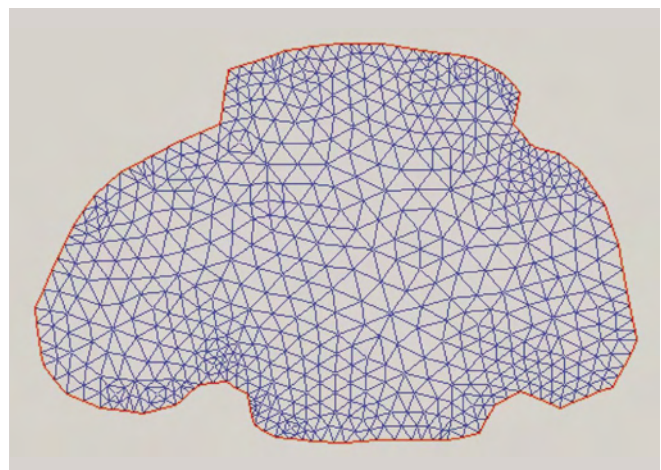


Figure 5d: FEM mesh constructed from the anatomical MR image.

Contrast enhanced MR images were also collected (CE-MRI) using Gd-DTPA, which is a well-established method to detect malignant tissues. Since vascular growth is greatly enhanced in tumor structures, contrast agent uptake of tumor sites increases with respect to normal tissues. In addition to that, interstitial compartment in tumors are large compared to normal structures, so the wash-out of contrast agent is also slower in tumors. Therefore, if two images are collected, one pre-contrast and the other post-contrast, the difference image yields enhanced pixel intensity in the areas of tumor growth. In this study, the goal was to verify the potential of MR-EIT to detect tumors. Contrast enhanced images were collected using a GE sequence with a 64×64 data matrix, FOV=10cm, 6mm slice thickness, TR=150ms, TE=5ms, and 45° flip angle. One pre-contrast image was acquired before Gd-DTPA injection and a post-contrast image was collected 3 minutes after injection.

Results

Conductivity images were reconstructed using the method outlined in the **Methods** section. In the calculation of the inverse of **S** using SVD, the highest 200 singular values were used and the rest were truncated to minimize noise while preserving essential information. This value was also determined experimentally to be an optimum level for truncation. In the FEM mesh, 512 triangular elements were used.

Impedance Contrast Phantoms

Figure 3a illustrates the standard spin-echo MRI image acquired from the contrast phantom (with 1:4 conductivity contrast). As seen in the Figure, it is difficult to distinguish the two compartments in the MRI image. The top row in Figure 3b shows conductivity images obtained from the 1:10 contrast phantom with two separate current amplitudes. Similarly, the bottom row of Figure 3b shows conductivity image of the 1:4 contrast phantom. Higher conductivity regions are greatly enhanced in the resulting images. The means of the reconstructed relative conductivity values in the two compartments inside the contrast phantoms were calculated and given in Table I.

Figure 3c shows the relationship between relative object conductivity values and relative MREIT image conductivity values as measured from the images given in Figure 3b (and Table I). Since the background conductivity is kept the same for 1:4 and 1:10 contrast phantoms, all conductivity values reported in Table I were normalized by their corresponding background values (σ_{or}) for this graph. Thus, the conductivity image contrast is obtained by dividing the mean conductivity in small disk (σ_{ir}) by the background mean value (σ_{or}). Using these measurements, the relative changes in object conductivity and corresponding conductivity contrast

in the MREIT images were plotted. The plots are given for both 2mA and 4mA injected current cases. A non-linear relationship is observed in these plots. Moreover, the difference between the two curves was statistically significant.

Effect of Initial Conductivity Estimate on Contrast

The reconstructed images in simulation studies were analyzed to assess the effect of initial estimate in conductivity image contrast. Mean values in the background and inner disc were calculated for each of the generated 1:0.5, 1:2, 1:4 and 1:10 contrast phantoms. Those values are calculated for each of the three different initial estimates of 0.001, 0.002 and 0.004S/cm. *Reconstructed conductivity ratio* is defined as the mean value of the inner disk divided by the mean value of the background in the reconstructed images. For each of the three initial estimates, a graph of *actual conductivity ratio* versus *reconstructed conductivity ratio* was plotted in Figure 3d.

Spatial Resolution Phantoms

Figure 4a shows the conductivity image of the “spatial resolution phantom” with two identical nylon disks. The results of two experiments with 2mA and 4mA current injections are given in this Figure. The gradually decreasing distance between the two small disks was used to assess the spatial resolution capability of conductivity images. A cross sectional profile taken diagonally from Figure 4a is shown in Figure 4b. This profile was taken from a cut that passed through the centers of the small disks. Even though the contrast was somewhat reduced due to low-pass filtering of the point-spread function, the 1mm separation could still be observed. On the other hand, the conductivity phantom with ten times higher conductivity does not provide the same precision of detection capability (Figure 4c). The 1mm separation is hardly distinguishable in this figure.

In vivo Imaging

The first step in animal imaging is the construction of the finite element mesh using an anatomical high resolution MRI image. The FEM mesh shown in Figure 5d consists of 702 nodes and 1268 first order triangular elements. Exact electrode locations are found using the markers in the animal setup and used for the boundary condition determination. The relative conductivity distribution was computed as described above and overlaid on the anatomical image (Figure 5a). The resulting images show the higher conductivity regions with high contrast. Similarly, the contrast enhancement by Gd-DTPA is illustrated in Figure 5b. To investigate how the two images spatially correlate, another image was generated by masking the CE-MRI image with the MREIT image regions that have conductivity values in the upper one-thirds of the full range. Figure 5c shows regions that have high conductivity and also enhanced by Gd-DTPA.

Discussion

In this preliminary study, the potential of the MREIT method for obtaining *in vivo* conductivity information with good spatial resolution and sensitivity was demonstrated, which may be helpful in identifying malignant tumors.

In the results presented here, a fixed frequency of 200Hz was used for the applied electrical currents. This choice was based on previous studies that investigated electrical properties of tumors (7). Those studies have reported that a higher conductivity contrast was obtained with the application of 200Hz currents.

In contrast phantom tests, conductivity ratios of 1:4 and 1:10 were used. The method presented here clearly detected these conductivity perturbations in the objects. Based on the range of conductivity changes of malignancies compared to those of benign or healthy tissues that were reported in the literature (1), MREIT should offer sufficient sensitivity for the detection of malignancies. Although the minimum detectable conductivity perturbation by MREIT has not been tested, from the results presented, it may be anticipated that much smaller changes could also be detected.

Since the reconstruction method used here is based on the linearity assumption between conductivity perturbations and measured magnetic fields, it only gives precise relative conductivity measurements for small conductivity perturbations within the object (or body). In the results presented here, the ratio of conductivity values measured in various compartments in the reconstructed images did not reflect the actual conductivity contrast. Since relatively large conductivity changes were used in the phantoms, it was observed that the conductivity contrast in the images was lower than the actual ratios due to the nonlinear nature of the actual relationship. The non-linear relationship between conductivity perturbations in the object versus perturbations in reconstructed EIT images was studied in detail by Ider *et al.* (27). These problems, arising from the nonlinearity of reconstruction method, can be minimized by using iterative reconstruction techniques with regularization. One such technique called the *weighted regularized least square method* (WRLSM) was used by Oh *et al.* (30) to reconstruct conductivity images using MRI. Although they applied this method to *harmonic Bz algorithm*, it can be easily adopted to our reconstruction technique. *Harmonic Bz algorithm* requires the second partial derivatives of the magnetic field B_z ($\nabla^2 B_z$), therefore, it is vulnerable to the noise in the B_z measurements. Spatial dependence of accuracy was observed in Oh's study, where the two profiles from different sections of conductivity images revealed different accuracy with respect to the true conductivity profiles. Moreover, they have used significantly higher current amplitude of 26mA, compared to the val-

ues of 2 and 4mA used in the presented study. One advantage of our reconstruction technique is that it is less vulnerable to noise compared to the *harmonic Bz algorithm*, because of the fact that it does not require derivatives of B_z . Therefore, an iterative WRLSM technique is expected to improve accuracy of relative conductivity images obtained in our studies. Our group is currently working on the implementation of such a technique. In addition to that, it can also be observed that the contrast in the conductivity images decreased when the amplitude of the current was decreased from 4 to 2mA. Since the non-linear relationship between magnetic field distribution and conductivity values is assumed to be linear in the sensitivity matrix method, the degree of deviation from linearity will vary with changing current amplitude. As seen in the Figure, the curve with 2mA current amplitude is slightly more linear compared to the 4mA current injection case but with reduced slope, *i.e.*, reduced contrast. This aspect could be an important consideration in longitudinal studies where the change in conductivity in a tumor is investigated over time.

Simulation studies have shown that the relative conductivity contrast in reconstructed images is also dependent on the initial conductivity estimate. Slight deviations in curves shown in Figure 3d were observed within the range of initial values tested. Therefore, the initial estimate of conductivity in sensitivity matrix reconstruction will have an impact on the resultant image contrast.

Two simple phantoms were prepared, where the separation between two closely separated non-conductive or highly conductive disks were used to assess resolution. It was found that the closest distance of 1mm was still detectable in the images where non-conducting disks were used. On the other hand, the 1mm separation was hardly distinguishable in the phantom with highly conductive disks. Therefore, the relative conductivity of inner structures plays an important role in the resolution, as expected. Current density is an important factor that determines sensitivity in this imaging technique. High current density in a particular area will increase sensitivity in that area. Thus, in the non-conducting object case, there will be high current density between the two insulators, whereas, in the high-conductivity object case, most of the current density will be concentrated inside the relatively large objects and suppress the perturbation of small separation. Moreover, a certain amount of diffusion between the high-conductivity objects and the low-conductivity separation can be expected, which will adversely affect the resolution. To minimize that effect, images are collected immediately after the phantom preparation. For better assessment of resolution, diffusion has to be taken into account. Similarly, it may be expected that the detectability of the object separation will also be affected by the size of the inner disks. Construction of

sophisticated high-resolution phantoms with agarose gel is a mechanically challenging task due to the lack of rigidity in the gel structure. Small structures can easily melt and blend into each other making boundaries somewhat ambiguous. Although more complicated phantoms could be built with different materials to investigate the spatial resolution of the method, these two simple phantoms illustrate how well the separation between objects of different conductivity could be resolved. Generally, a high contrast object is required to assess the spatial resolution of an imaging technique, since it is affected less by noise; therefore, the test with insulators appears to be a better assessment of the resolution in the presented study.

Similarly, conductivity images collected from animals *in vivo* showed significantly increased conductivity in tumor areas. Tumor location was identified by contrast enhanced MRI. It is seen from these results that there is high correlation between the conductivity images and contrast enhanced MR images. Although they do not completely overlap, this is expected because the two methods emphasize different properties of tumors. For example, edema will most likely show high conductivity but will not show signal enhancement with the CE-MRI. To exclude edematous regions from the conductivity images, one can use T2 weighted sequences that highlights edema. In this preliminary experiment, an animal with a large tumor size was imaged, which was available at the time. As seen in the CE-MRI images, the tumor had spread into several foci that encircled the animal's trunk. In large tumors, various compartments like edema, necrosis and viable tumor cells exist and their conductivity and contrast agent enhancement will be different. Currently, a longitudinal study is planned to observe changes in conductivity as well as Gd-DTPA based contrast enhancement in tumor structures as the tumor grows. The CE-MRI will be used to verify the MREIT results *in vivo*. At the end of the study, tumors will be excised and undergo histologic analysis. Contrast enhanced and T2 weighted images together with the MREIT maps will allow for the assessment of how conductivity correlates with different compartments in tumors. The positions and numbers of electrodes could be another factor that may confound the detection of some low conductivity structures close to surface. The effects of electrode placement will also be investigated in future studies.

In all phantom studies, as well as *in vivo* experiments, the current carrying wires were placed precisely in the z-direction with acrylic support beams. Those wires were attached to the electrodes without any bends. Therefore, the magnetic fields generated by the currents in these lead wires would have mainly B_x and B_y components and B_z will be negligible. Therefore, any significant contribution from the currents in the lead wires to the B_z measurements is not expected.

In general, currents flowing in an object generate a 3D magnetic field. The currents flowing inside an imaging slice generate a magnetic field that has only a component, which is perpendicular to the plane of the slice. In this preliminary study, the magnetic fields generated by currents outside the imaging slice were ignored, reducing the reconstruction to 2D. Since most of the current flow will be concentrated between the electrodes, this approximation was deemed to be adequate for the pilot studies. Currently, 3D reconstruction methods are being developed in our laboratory that will account for such out-of-slice effects.

Acknowledgements

This research is supported by Department of Defense DAMD17-02-1-0326 and NIH P20-CA86182 grants.

References

1. Surowiec, A. J., Stuchly, S. S., Barr, J. R., and Swarup, A. Dielectric Properties of Breast Carcinoma and the Surrounding Tissues. *IEEE Trans. on BME* 35 257-263 (1988).
2. Elmore, J. G., Barton, M. B., Mocer, V. M., Polk, S., Arena, P. J., and Fletcher, S. W. Ten-year Risk of False Positive Screening Mammograms and Clinical Breast Examinations. *The New England Journal of Medicine* 338, 1089-1096 (1998).
3. Christiansen, C. L., Wang, F., Barton, M. B., Kreuter, W., Elmore, J. G., Gelfand, A. E., and Fletcher, W. Predicting the Cumulative Risk of False-Positive Mammograms. *Journal of the National Cancer Institute* 92, 1657-1666 (2000).
4. Elmore, J. G., Miglioretti, D. L., Reisch, L. M., Barton, M. B., Kreuter, W., Christiansen, C. L., and Fletcher, S. W. Screening Mammograms by Community Radiologists: Variability in False-Positive Rates. *Journal of the National Cancer Institute* 94, 1373-1380 (2002).
5. Moore, S. K. Better Breast Cancer Detection. *IEEE Spectrum* 38, 50-54 (2001).
6. Coons, T. A. MRI's Role in Assessing and Managing Breast Disease. *Radiological Technology* 67, 311-336 (1996).
7. Malich, A., Boehm, T., Facius, M., Freesmeyer, M. G., Fleck, M., Anderson, R., and Kaiser, W. A. Differentiation of Mammographically Suspicious Lesions: Evaluation of Breast Ultrasound, MRI Mammography and Electrical Impedance Scanning as Adjunctive Technologies in Breast Cancer Detection. *Clinical Radiology* 56, 278-283 (2001).
8. Boone, K., Barber, D. and Brown, B. Imaging with Electricity: Report of the European Concerted Action on Impedance Tomography. *Journal of Medical Engineering and Technology* 21, 201-232 (1997).
9. Cherepenin, V., Karpov, A., Korjensky, A., Kornienko, V., Mazaletskaya, A., Mazourov, D., and Meister, D. A 3D Electrical Impedance Tomography (EIT) System for Breast Cancer Detection. *Physiological Measurement* 22, 9-18 (2001).
10. Estrela da Silva, J., Marques de Sá, J. P., and Jossinet, J., Classification of Breast Tissue by Electrical Impedance Spectroscopy. *Medical and Biological Engineering and Computing* 38, 26-30 (2000).
11. Kerner, T. E., Paulsen, K. D., Hartov, A., Soho, S. K., and Poplack, S. P. Electrical Impedance Spectroscopy of the Breast: Clinical Imaging Results in 26 Subjects. *IEEE Trans. on Medical Imaging* 21, 638-645 (2002).
12. Malich, A., Fritsch, T., Anderson, R., Boehm, T., Freesmeyer, M. G., Fleck, M., and Kaiser, W. A. Electrical Impedance Scanning for Classifying Suspicious Breast Lesions: First Results. *Eur. Radiol.* 10, 1555-1561 (2000).

13. Malich, A., Fritsch, T., Mauch, C., Boehm, T., Freesmeyer, M., Fleck, M., Anderson, R., and Kaiser, W. A. Electrical Impedance Scanning: A New Technique in the Diagnosis of Lymph Nodes in Which Malignancy Suspected on Ultrasound. *The British Journal of Radiology* 74, 42-47 (2001).
14. Malich, A., Boehm, T., Facius, M., Freesmeyer, M., Fleck, M., Anderson, R., and Kaiser, W. A. Additional Value of Electrical Impedance Scanning: Experience of 240 Histologically-proven Breast Lesions. *European Journal of Cancer* 37, 2324-2330 (2001).
15. Assenheimer, M., Laver-Mokovitz, O., Malonek, D., Manor, D., Nahaliel, U., Nitzan, R., and Saad, A. The T-SCAN™ Technology: Electrical Impedance as a Diagnostic Tool for Breast Cancer Detection. *Physiological Measurement* 22, 1-8 (2001).
16. Ider Y. Z. and Birgul, O. Use of the Magnetic Field Generated by the Internal Distribution of Injected Currents for Electrical Impedance Tomography (MR-EIT). *Elektrik, Turkish Journal of Electrical Engineering and Computer Sciences* 6, 215-225 (1998).
17. Birgul, O., Eyuboglu, M., and Ider, Y. Z. A New Technique for High Resolution Absolute Conductivity Imaging Using Magnetic Resonance-Electrical Impedance Tomography (MR-EIT). *Proceedings of SPIE – The International Society for Optical Engineering, Medical Imaging* 4320, 880-888 (2001).
18. Khang, H. S., Lee, B. I., Oh, S. H., Woo, E. J., Lee, S. Y., Cho, M. H., Kwon, O., Yoon, J. R., and Seo, J. K. J-Substitution Algorithm in Magnetic Resonance Electrical Impedance Tomography (MREIT): Phantom Experiment for Static Resistivity Images. *IEEE Trans. on Medical Imaging* 21, 695-702 (2002).
19. Birgul, O., Eyuboglu, B. M., and Ider, Y. Z. Current Constrained Voltage Scaled Reconstruction (CCVSR) Algorithm for MR-EIT and its Performance with Different Probing Current Patterns. *Physics in Medicine and Biology* 48, 653-671 (2003).
20. Birgul, O., Eyuboglu, B. M., and Ider, Y. Z. Experimental Results for 2D Magnetic Resonance-electrical Impedance Tomography (MR-EIT) Using Magnetic Flux Density in One Direction. *Physics in Medicine and Biology* 48, 3485-3504 (2003).
21. Oh, S. H., Han, J. Y., Lee, S. Y., Cho, M. H., Lee, B. I., and Woo, E. J. Electrical Conductivity Imaging by Magnetic Resonance Electrical Impedance Tomography (MREIT). *Magnetic Resonance in Medicine* 50, 875-878 (2003).
22. Scott, G. C., Joy, M. L. G., Armstrong, R. L., and Henkelman, R. M. Measurement of Non-uniform Current Density by Magnetic Resonance. *IEEE Trans on Medical Imaging* 10, 362-374 (1991).
23. Ider, Y. Z. and Muftuler, L. M. Measurement of AC Magnetic Field Distribution using Magnetic Resonance Imaging. *IEEE Trans. on Medical Imaging* 16, 617-622 (1997).
24. Mikac, U., Demsar, F., Beravs, K., and Sersa, I. Magnetic Resonance Imaging of Alternating Electric Currents. *Magnetic Resonance Imaging* 19, 845-856 (2001).
25. Scott, G. C., Joy, M. L. G., Armstrong, R. L., and Henkelman, R. M. Electromagnetic Considerations for RF Current Density Imaging. *IEEE Trans. on Medical Imaging* 14, 515-524 (1995).
26. Glickman, Y. A., Filo, O., Nachaliel, U., Lenington, S., Amin-Spector, S., Ginor, R. Novel EIS Postprocessing Algorithm for Breast Cancer Diagnosis. *IEEE Trans. on Medical Imaging* 21, 710-712 (2002).
27. Ider, Y. Z., Eyuboglu, B. M., Kuzuoglu, M., Leblebicioglu, K., Baysal, U., Caglar, B. K., and Birgul, O. A Method for Comparative Evaluation of EIT Algorithms Using a Standard Data Set. *Physiol. Meas.* 16, A227-A236 (1995).
28. Baumann, B. B., Wozny, D. R., Kelly, S. K., Meno, F. M. The Electrical Conductivity of Human Cerebrospinal Fluid at Body Temperature. *IEEE Trans. BME* 44, 220-223 (1997).
29. Ackmann, J. J. Complex Bioelectric Impedance Measurement System for the Frequency Range from 5 Hz to 1MHz. *Annl. Biomed. Eng.* 21, 135-146 (1993).
30. Oh, S. H., Lee, B. I., Woo, E. J., Lee, S. Y., Cho, M. H., Kwon, O., Seo, J. K. Conductivity and Current Density Image Reconstruction using *Harmonic Bz Algorithm* in Magnetic Resonance Electrical Impedance Tomography. *Phys. Med. Biol.* 48, 3101-3116 (2003).

Date Received: April 26, 2004

3D Magnetic Resonance Electrical Impedance Tomography at 4T using Sensivity Matrix based Reconstruction

O. Birgul¹, L. T. Muftuler¹, M. J. Hamamura¹, and O. Nalciglu¹

¹Tu and Yuen Center for Functional Onco Imaging, University of California, Irvine, CA, United States

Purpose

The difference between the conductivity of malignant tumors and the surrounding normal tissue provides a possible way to detect and specify different tumor types. The conductivity distribution can be found using magnetic resonance-electrical impedance tomography (MREIT) with a resolution higher than other conductivity imaging techniques [1]. In MREIT a current distribution is created within the object, resulting magnetic flux density is measured using MRI, and an inverse problem is solved to find the conductivity distribution using magnetic flux density measurements. MREIT reconstruction algorithms can be grouped into three: (1) current density based algorithms (that calculates current density from magnetic field during reconstruction), (2) gradient Bz algorithms (that uses first or second order derivative of magnetic flux density) and (3) sensitivity matrix based algorithms (that uses magnetic field directly). First group of algorithms requires rotation of the object inside the magnet, which is unpractical. Second group of algorithms are very sensitive to noise in the phase due to the derivative operator used. Sensitivity matrix approach is shown to perform better in noise; however, it requires storage and processing of large matrices. Several results have been presented for phantom and animal experiments using 2D sensitivity approach [1,2]. In 2D approximation, it is assumed that injected current is confined to the slice of interest and magnetic flux density measured from the same slice is used for reconstruction. In most experiments, however, injected currents will be distributed in all directions. Depending on the conductivity values of the adjacent slices, off-slice currents will contribute to the magnetic flux measurement and must be included in modeling. In this study, we conducted experiments with 3D phantoms and implemented a 3D sensitivity matrix reconstruction algorithm.

Methods

When low amplitude sinusoidal current is injected into an object, the resulting magnetic field accumulates additional phase in the MR images. A modified fast spin-echo sequence [3], where a 90° RF pulse is followed by a number of 180° (π) RF pulses, is used to measure the magnetic field. Phase induced in positive and negative current cycles would cancel out each other unless multiple π are used. By synchronizing successive π pulses to half cycles of the current, this phase shift accumulates and is given in the final image as $\phi(\mathbf{r}) = 4\gamma N \cdot \mathbf{b}(\mathbf{r}) / \omega$, where γ is the gyromagnetic ratio, N the number of cycles of injected current, $\mathbf{b}(\mathbf{r})$ the amplitude of z-component current-generated magnetic field at point \mathbf{r} , and ω the angular frequency of the injected current.

Once the magnetic field is measured, the inverse problem of calculating the internal conductivity distribution from these measurements is solved. Sensitivity based reconstruction algorithm is implemented in 3D. Uniform conductivity distribution is assumed and sensitivity matrix (\mathbf{S}) is calculated using a 3D finite element method (FEM). Sensitivity matrix gives the relation between $\Delta \mathbf{b}$ (the difference between measured magnetic flux density and the magnetic flux density corresponding to initial distribution) and $\Delta \sigma$ (the change with respect to initial) as $\Delta \mathbf{b} = \mathbf{S} \Delta \sigma$. Including Tikhonov regularization parameter, λ , the matrix equation becomes $(\mathbf{S}^T \mathbf{S} + \lambda \mathbf{I}) \Delta \sigma = \mathbf{S}^T \Delta \mathbf{b}$ where \mathbf{I} is the identity matrix. The matrix equation is solved for different values of λ using conjugate gradient method and the optimum regularization value is selected as the one minimizing the difference between measured and calculated magnetic flux densities.

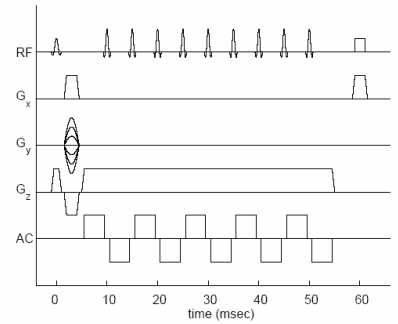


Fig 1. Pulse Sequence

Results

A 3D phantom was prepared using agarose powder (1gr/100mL) as background and a spherical shell filled with the same agarose gel. Due to insulator shell, the whole sphere acted as a nonconducting object. Four electrodes of size 0.5cm x 0.5cm were placed at the center of the cylinder every 90° as shown in Fig 2. Opposite pairs were used, giving two current injection profiles. A FEM mesh with 2399 nodes and 11781 tetrahedral elements was constructed. The magnetic flux density is calculated at a rectangular grid of $24 \times 24 \times 5$, where 2300 of grid points falling into the cylindrical region. A total of 4600 measurements were used in image reconstruction. MR structural images for the 5 slices used are given in Fig. 3 (top row). Corresponding reconstructed conductivity images are presented in bottom row, dark region corresponding to insulating object.

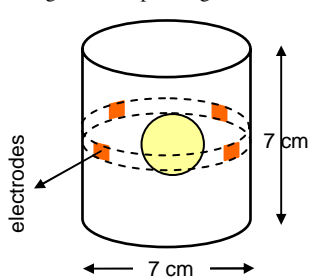


Fig 2. Phantom Definition

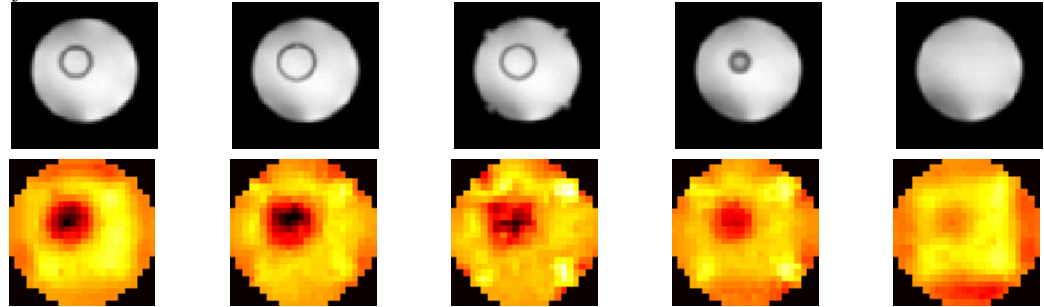


Fig 3. MR anatomical images (top row) and corresponding reconstructed conductivity images (bottom row)

Discussion

In this study, we demonstrated the feasibility of using 3D sensitivity matrix reconstruction in multi-slice magnetic resonance electrical impedance imaging. Although sensitivity matrix based reconstruction methods are computationally expensive, they perform well in the presence of noise. Previously, we used sensitivity matrix based reconstruction using 2D FEM. That approach ignores the contributions of currents in off-center slices leading to various artifacts in the conductivity images; conductivity values in the reconstructed slice could be under or overestimated, spatial resolution and point spread function could be compromised. In some cases the 'ghosts' of objects in other slices may even appear in the reconstructed slice depending on how the conductivity and resulting 3D current density is distributed in the object.

References

[1] Birgul O, et al. PMB, **51**, 5035-5049 (2006), [2] Muftuler L T, et al., TCRT **5** (4) 381-387 (2006). [3] Malich A, et al., Eur. Radiol, **10**, 1555-1561 (2000)

Acknowledgments

This research is supported in part by Department of Defense Award W81XWH-04-1-0446 and NIH/NCI Award R01 CA114210.

Comparison of Magnetic Resonance Electrical Impedance Tomography at 4T and 7T Field Strengths

O. Birgul¹, M. J. Hamamura¹, L. T. Muftuler¹, and O. Nalcioğlu¹

¹Tu and Yuen Center for Functional Onco Imaging, University of California, Irvine, CA, United States

Purpose

Low level injected currents generate a magnetic field within a body that can be measured using MRI. Magnetic resonance-electrical impedance tomography (MREIT) utilizes these measurements due to injected currents to construct the conductivity distribution within an object. Electrical conductivities of tissues are different among normal, malignant, and benign tissues. In-vivo impedance imaging of suspicious lesions could aid in the diagnosis and specification of malignant tumors. Several studies using phantoms and small animal bearing tumors demonstrated the efficacy of the algorithm [1, 2]. The magnetic flux density is extracted from MRI phase images and one of the challenges in MREIT is acquiring phase information with sufficient SNR while maintaining the injected currents at safe levels. Sadleir et. al. carried out noise analysis in magnetic flux density measurements at 3T and 11T and they suggest that the noise level in magnetic flux density is reduced as field strength is increased by a factor approximately proportional to the increase in the field strength [3]. In this study, we carried out experiments at 4T and 7T field strengths to compare the effect of increased magnetic flux density SNR in the final reconstructed conductivity images.

Methods

For the test phantom, a hollow acrylic tube and agarose gels with different NaCl concentrations were used. 2gr/100mL agarose powder and 4mM CuSO₄ were kept the same for all regions. Amount of NaCl was set to 1gr/100mL and 4gr/100mL for background and objects (O1,O2), respectively. The conductivity values were measured in an independent system as 5.68Sm⁻¹ and 1.61Sm⁻¹ (3.3:1 contrast). The diameter of the both objects were 6mm and their centers were located 1cm apart giving 4mm gap between their boundaries. The thickness of the phantom was 1cm and in-slice dimensions of the phantom are defined in Fig 1. Four copper electrodes each 3mm wide were placed equidistantly along the inner acrylic wall and used to probe the interior region. Bipolar current injection scheme was used the resulting magnetic flux density distribution measured using a modified spin-echo pulse sequence as shown in Fig 2. [4]. Opposite electrode pairs were used to get two current injection profiles. Iterated sensitivity matrix method (SMM) with Tikhonov regularization was used for conductivity reconstruction [1].

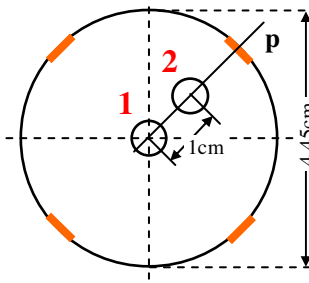


Fig 1. Phantom definitions

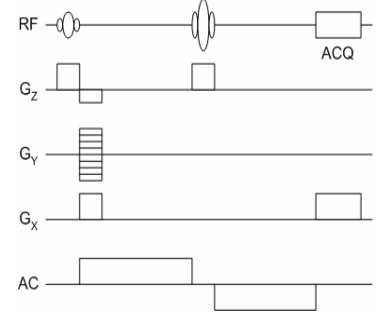


Fig 2. MREIT Pulse Sequence

Results

MREIT experiments were carried out using two phantoms with the same distribution in 4T and 7T systems. Since ion diffusion alters the initial conductivity distribution [5], we prepared the phantom immediately before each experiment to minimize these effects in the comparison. The pulse sequence parameters for both experiments were as: TR = 500ms, TE = 60ms FOV = 7cm, slice thickness = 2mm, field image matrix = 64x64, NEX = 4. The sampling bandwidth was set to 33.3KHz and 1.25MHz for 4T and 7T systems, respectively. The amplitude of the injected current was 1mA and the duration of the positive and negative cycles were 27.3ms and 27.7ms. Reconstructed conductivity images and profiles along p-line (as defined in Fig 1) at both field strengths are given in Fig 3. Although the phantom is slightly rotated between two cases, this does not affect the relative positions of the objects with respect to each other. We calculated full-width-at-half-maximum (FWHM) for both objects through x and y cross-sections and also we looked at peak contrast in the object. Note that the SMM reconstructs relative conductivity values if magnetic flux density measurements are used alone and the values presented here are normalized to the background conductivity. The peak reconstructed contrast and FWHM values are summarized in Table 1 for both field strengths and objects. The objects were not fully resolved in the p-line profile for 4T case but more separable in the 7T case. For all cases, the constructed contrasts are lower than the expected ones, especially for the object located at the center.

Table 1. Comparison of reconstructed peak contrast and FWHM

	peak contrast		FWHM-x (cm)		FWHM-y (cm)	
	O1	O2	O1	O2	O1	O2
True	3.3	3.3	0.6	0.6	0.6	0.6
4T	1.6	1.8	1.3	1.0	1.4	0.9
7T	1.8	2.2	1.0	0.8	1.1	0.8

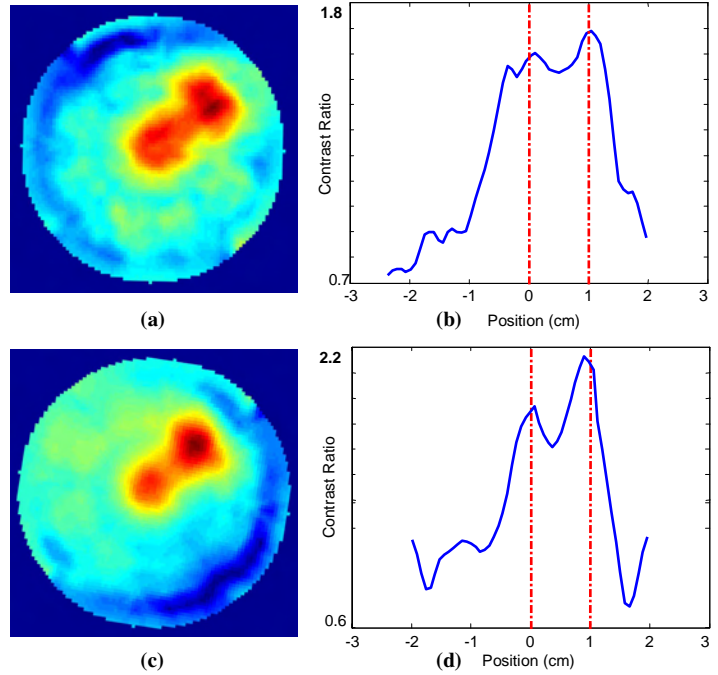


Fig 3.(a) image at 4T (b) 4T profile (along p-line) (c) image at 7T (d) 7T profile (along p-line)

Discussion

In this study, we carried out MREIT experiments at two different field strengths to understand how the improvement in magnetic flux density SNR affects the reconstructed conductivity values and target detection. When the reconstructed images are compared, it is seen that given the same amount of experimentation time, the accuracy and the spatial resolution of the conductivity images at 7T is better compared to 4T. Although the reconstructed contrast values are lower than the expected values due to ion diffusion in all cases, the comparison between different field strengths shows 13%-22% improvement at 7T compared to the 4T case. Major improvement is noticeable in the resolution of the objects, especially for the one at the center, when higher field strength is used.

References

- [1] Birgul O, et. al. PMB, **51**, 5035-5049 (2006), [2] Muftuler L T, et. al.,TCRT **5** (4) 381-387 (2006). [3] Sadleir R, et. al.Physiol. Meas, **26**, 875-884, (2006) [4] Scott et al, IEEE TMI, **10**, 362-374 (1991) [5] Hamamura et al, PMB, **51**, 2753-2762 (2006)

Acknowledgments

This research is supported in part by Department of Defense Award W81XWH-04-1-0446 and NIH/NCI Award R01 CA114210.

Fast Imaging for Magnetic Resonance Electrical Impedance Tomography

M. J. Hamamura¹, L. T. Muftuler¹, O. Birgul¹, and O. Nalcioglu¹

¹Tu & Yuen Center for Functional Onco-Imaging, University of California, Irvine, CA, United States

Purpose

In Magnetic Resonance Electrical Impedance Tomography (MREIT), electrical currents are injected into an object and the resulting magnetic flux density distribution measured using MRI. Various spin echo based pulse sequences have been proposed to perform this measurement, where a single line of k-space data is collected per excitation. In this study, we investigate the use of a single shot, spin echo, echo planar imaging (SS-SEPI) pulse sequence for acquiring MREIT data.

Methods

For the test phantom, a hollow acrylic disk with an inner diameter of 7cm and thickness of 1cm was filled with 2% agarose and 4mM CuSO₄. Within this disk, a smaller cylindrical region of 13mm diameter was filled with 1% NaCl, 2% agarose, and 4mM CuSO₄ to generate a high conductivity region (Figure 1). The plane of the disk was placed perpendicular to the main static MRI field. Two copper electrodes each 6mm wide were placed opposite of each other along the inner acrylic wall and used to inject currents into the interior region.

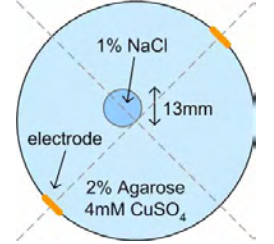


Fig. 1. Phantom Schematic

A 4mA bipolar current pulse was injected into the phantom and the resulting magnetic flux density distribution measured using a modified SS-SEPI pulse sequence (Figure 2). The component of current-generated magnetic flux density parallel to the main static MRI field (z-component) introduced a phase shift in the MR image given as: $\phi(\mathbf{r}) = \gamma(T_A + T_B) \cdot B_z(\mathbf{r})$.

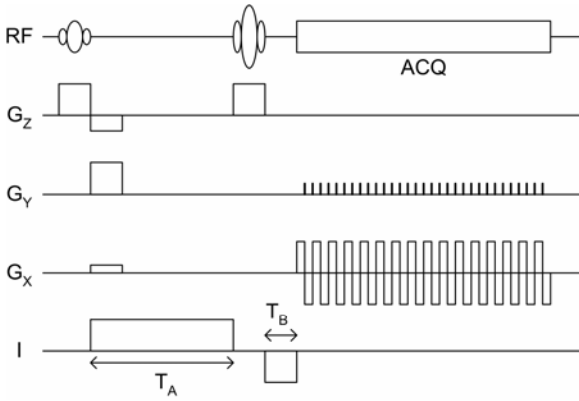


Fig. 2. SS-SEPI pulse sequence for MREIT

The scan parameters were: $T_A = 35\text{ms}$, $T_B = 10\text{ms}$, $TR = 3\text{ms}$, $TE = 60\text{ms}$, matrix = 64×64 , $FOV = 20\text{cm}$, and single slice thickness = 5mm . Data was collected twice, each with opposite polarities in the applied current waveform. The resulting phase maps were subtracted then divided by two, so as to cancel out any additional phase contributions, such as those arising from small imperfections in the hardware timing.

To reconstruct the conductivity distribution using the MRI measurements, the Sensitivity Matrix Method was utilized [Birgul et al, *Phys Med Biol* 51: 5035-5049 (2006)] in which the relationship between conductivity and z-component magnetic flux density is linearized around an initial conductivity (i.e. uniform distribution) and formulated as a matrix equation. This equation is then solved for the true conductivity distribution using Tikhonov regularization. The resulting conductivity can then be substituted back into the linearized equation as the new, updated initial condition, and the process iterated to improve the reconstruction.

Results

Data was collected using a 4T MRI system. For comparison, data was also acquired using no injected current, and also using the original SE-based measurement sequence [Scott et al, *IEEE TMI* 10: 362-374 (1991)]. Relative conductivities were reconstructed for the various data using 5 iterations of the Sensitivity Matrix Method (Figure 3). As part of the reconstruction process, a Finite Element Method mesh was aligned to the MR image, and the resulting conductivity map linearly transformed back into a circular geometry.

Discussion

Comparison of the 0mA and 4mA cases shows that the SS-SEPI pulse sequence was able to detect the magnetic flux density generated by the injected current. Comparison with the SE results shows that the SS-SEPI pulse sequence was also able to map out the general variation in the

magnetic flux density due to the high conductivity perturbation. However, the SS-SEPI images suffer from geometric distortions resulting from the low sampling bandwidth in the phase encode direction inherent in EPI-based pulse sequences. As a result, the reconstructed conductivity distribution also suffers from some geometric distortion. Never the less, the high conductivity perturbation could still be reconstructed from the SS-SEPI data. We could further improve reconstruction by applying some sort of geometric correction to the MRI data.

An advantage of the SS-SEPI pulse sequence is the significant reduction in data acquisition time. This could allow for increased signal averaging in an allotted study time, which may be required for improving the SNR when using low amplitude injected currents. Single shot pulse sequences are also less susceptible to motion artifacts, which may be of significance when applying MREIT to *in vivo* studies.

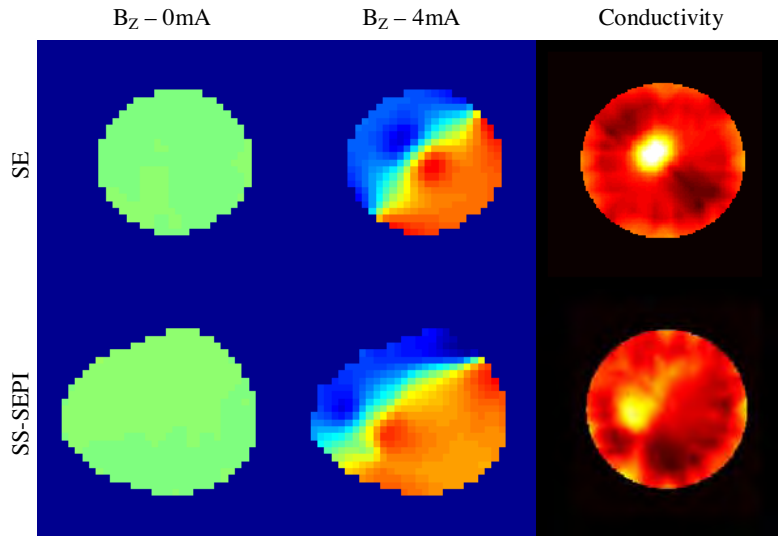


Fig. 3. Magnetic flux density and reconstructed conductivity distributions

Acknowledgements

This research is supported in part by NIH R01 CA114210-01 and DOD W81XH-04-1-0446.

Magnetic Resonance Electrical Impedance Tomography Using Biologically Safe Injected Current Levels

M. J. Hamamura¹, L. T. Muftuler¹, O. Birgul¹, and O. Nalcioglu¹

¹Tu & Yuen Center for Functional Onco-Imaging, University of California, Irvine, CA, United States

Purpose

In Magnetic Resonance Electrical Impedance Tomography (MREIT), electrical currents are injected into an object and the resulting magnetic flux density distribution measured using MRI. These MRI measurements are then used to reconstruct the conductivity distribution within the object. We have recently reported on the measurement of ion diffusion with MREIT using injected current pulses of 900 μ A [Hamamura *et al*, *Phys Med Biol* 51: 2753-2762 (2006)]. To our knowledge, this is the lowest level of current successfully used in MREIT to date. However, this level still remains above the required safety limits for application in human studies. The IEC 601 standard limits “patient auxiliary currents” to 100 μ A at low frequencies. In this study, we assess the efficacy of MREIT using such biologically safe injected current levels.

Methods

Lower injected current levels reduce the SNR of the acquired magnetic flux density maps used in the reconstruction process. To improve the SNR, we utilized a 7T high field system with increased signal averaging to acquire our MRI measurements. For the test phantom, a hollow acrylic disk with an inner diameter of 4.445cm and thickness of 1cm was filled with 2% agarose and 4mM CuSO₄. Within this disk, a smaller plastic shell of 6mm diameter was placed slightly off-center to simulate a low conductivity region (Fig. 1). The plane of the disk was placed perpendicular to the main static MRI field. Four copper electrodes each 3mm wide were placed equidistant along the inner acrylic wall and used to inject currents into the interior region.

A bipolar current pulse was injected into the phantom and the resulting magnetic flux density distribution measured using a modified spin-echo pulse sequence (Fig. 2) [Scott *et al*, *IEEE TMI* 10: 362-374 (1991)]. The scan parameters were: TR = 500ms, TE = 60ms, matrix = 128X128, FOV = 14cm, and single slice thickness = 1mm. Data was

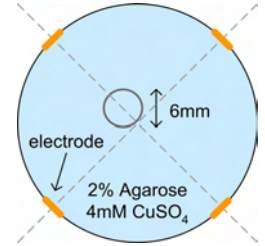


Fig. 1. Phantom Schematic

collected for two different current injection schemes (in pairs of electrodes directly opposite of each other) and used simultaneously in conductivity reconstruction. To reconstruct the conductivity distribution using the MRI measurements, the Sensitivity Matrix Method was utilized [Birgul *et al*, *Phys Med Biol* 51: 5035-5049 (2006)] in which the relationship between conductivity and magnetic flux density is linearized around an initial conductivity (i.e. uniform distribution) and formulated as a matrix equation. This equation is then solved for the true conductivity distribution using Tikhonov regularization. The resulting conductivity can then be substituted back into the linearized equation as the new, updated initial condition, and the process iterated to improve the reconstruction.

Results

Data was collected with various amounts of signal averaging using a current amplitude of 100 μ A. For comparison, high SNR data was collected by using 5mA of injected current. Relative conductivities were reconstructed for the various data using 5 iterations of the Sensitivity Matrix Method (Fig. 3).

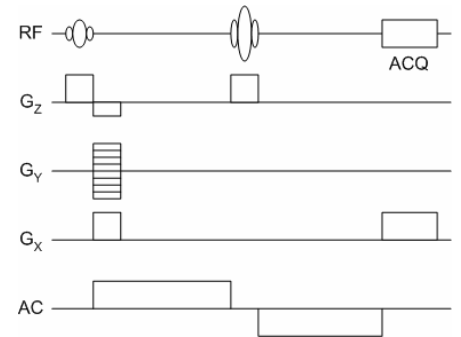


Fig. 2. MREIT Pulse Sequence

Discussion

The results of this study demonstrate that MREIT is capable of reconstructing conductivities using biologically safe injected current levels. Even with a single average, we can observe the lower conductivity perturbation within our test phantom. However, lower SNR data generated considerable variation in the (uniform) background. Improving the SNR through increased signal averaging reduced these artifacts.

When applying MREIT to human studies, the larger object size and 3D current flow will result in a decrease in the measurable magnetic flux density. This study illustrates that increased signal averaging can compensate for this corresponding decrease in SNR. In practice, the presence of correlated noise decreases the efficiency of additional averaging, and places an upper bound on SNR gain. This limitation must be investigated further, as well as other techniques to improve SNR when using low amplitude injected currents.

Acknowledgements

This research is supported in part by NIH R01 CA114210-01 and DOD W81XHX-04-1-0446.

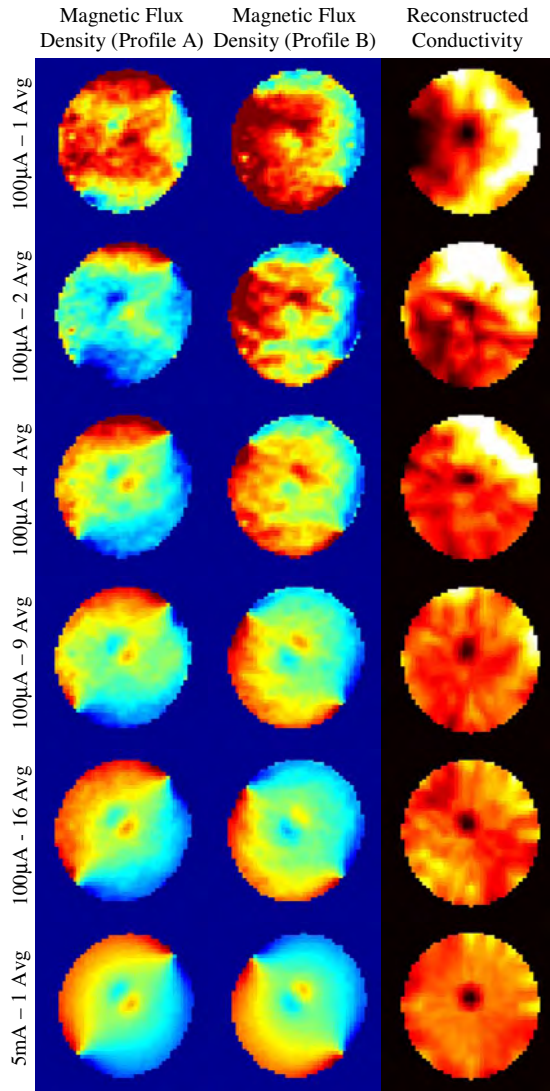


Fig. 3. Magnetic flux density and reconstructed conductivity distributions for various experiments.

Mutual Information Based MREIT Reconstruction Using MR Anatomical Data

G. Chen¹, L. T. Muftuler¹, O. Birgul¹, M. J. Hamamura¹, and O. Nalcioglu¹

¹Tu & Yuen Center for Functional Onco-Imaging, University of California, Irvine, CA, United States

Introduction:

As an adjunct to existing cancer detection techniques such as x-ray and MRI, Magnetic Resonance-Electrical Impedance Tomography (MREIT) has the potential to improve the specificity of current techniques because it is an imaging modality that measures tissue conductivity and it has been shown that the conductivity differs significantly among malignant, benign and normal tissues. A sensitivity based reconstruction algorithm with Tikhonov regularization has been successfully employed to resolve a complex and nested conductivity distributions [1]. In this work a mutual information based MREIT reconstruction algorithm was investigated to reconstruct the irregular conductivity distributions with improved accuracy.

Methods:

The injected currents inside an object will generate magnetic flux density; the component of the magnetic flux density in the main static field direction (\mathbf{b}_z) can be calculated from the MRI phase images using a modified spin echo pulse sequence [2]. To solve the conductivity distribution from the magnetic field measurement, the relationship between the perturbation of conductivity distribution ($\Delta\sigma$) around an initial estimate (σ_i) and the resultant perturbation of the magnetic flux density ($\Delta\mathbf{b}_z$) can be linearized ($\Delta\mathbf{b}_z = \mathbf{S}\Delta\sigma$) for a given current injection scheme. Here \mathbf{S} is the sensitivity matrix that can be calculated analytically [3]. Due to the ill-posed nature of the sensitivity matrix \mathbf{S} and noise in the data, regularization is required to solve the inverse problem of calculating $\Delta\sigma$ from $\Delta\mathbf{b}_z$ and \mathbf{S} . Including the Tikhonov regularization parameter λ , the matrix equations becomes $(\mathbf{S}^T\mathbf{S} + \lambda\mathbf{I})\Delta\sigma = \mathbf{S}^T\Delta\mathbf{b}_z$, where \mathbf{I} is the identity matrix, and the equation can then be solved using the conjugate gradient method. Previously λ was chosen to be the value that minimizing the difference between the measured magnetic flux density and the magnetic flux density calculated from the reconstructed conductivity. In this study we investigated mutual information based reconstruction methods [4] for MREIT. In the first approach, the λ value that maximized the mutual information between the calculated conductivity distribution image and the MR image was found. This is valid because mutual information is the measurement of nonlinear statistical dependency of two systems, and since both the MR image and conductivity image contain structural information about the tumor and the normal tissue, the mutual information between the two images should be maximized when the conductivity image is reconstructed most accurately.

Since the location and shape of the suspected lesions can be detected by MRI, one can generate an initial conductivity distribution with a two-compartment model that separates the suspected lesion and the normal tissue. This model will be a better approximation of the initial conductivity distribution (σ_i) instead of the standard approach of using a uniform σ_i . For the second approach, we first solve the inverse problem to find the conductivity values in these two compartments only, so a single conductivity value is calculated for each compartment. The resulting two-compartment conductivity map is used as the initial conductivity distribution in the second step and the equation above is solved to find the conductivity value for each pixel. Since this two-compartment σ_i is a better approximation, starting the iterative reconstruction from an initial condition closer to the actual values should yield more accurate conductivity maps and converge to the solution faster.

Results and discussion:

The same data acquired in the experiment described in [1] were used in the new reconstruction method. The reconstructed conductivity distribution using the original method in [1], the mutual information based reconstruction method with optimum λ (uniform initial conductivity), and the mutual information based reconstruction method with two-compartment initial conductivity distribution are shown in Fig.1. The two compartments were defined from the MR images that provide the contrast between compartments I and II in Fig.2. The reconstructed conductivities in the three cases were similar in general except in the regions marked by the red circles where substantial improvement was seen. Moreover, calculated conductivities from the mutual information based reconstructions were much closer to the actual values compared to the one calculated from the original method, where conductivity values turned out higher. Also note that the third compartment was successfully recovered although the σ_i was modeled with only two compartments. Therefore, it can be concluded that maximization of mutual information can be used as a criterion to reduce the uncertainty (such as estimation of the regularization parameter) in the MREIT conductivity reconstruction, thus the accuracy of the conductivity measurement can be improved by using the MR images as *a priori* information.

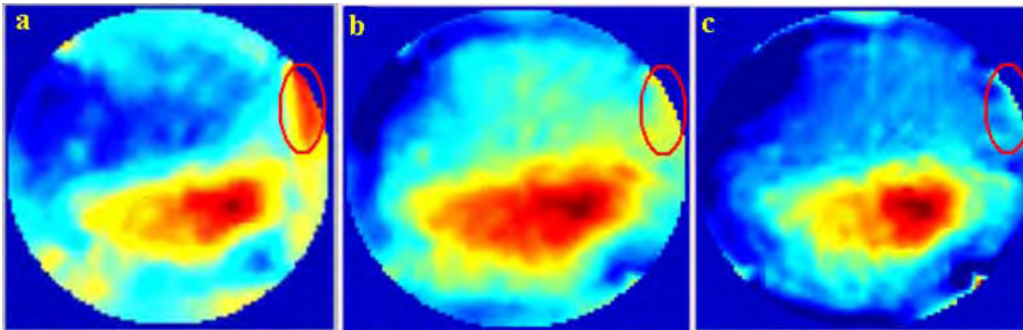


Fig1. The reconstructed conductivity distribution using the original method a), the mutual information based reconstruction method with optimum λ and uniform initial conductivity distribution b), and the mutual information based reconstruction method with two compartment averaged initial conductivity distribution c).

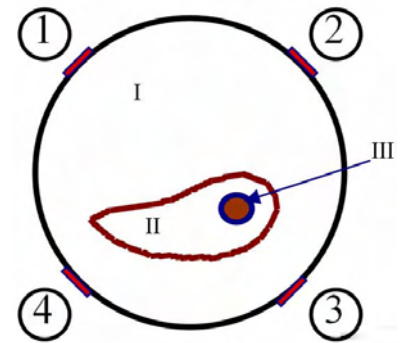


Fig 2. The schematic of the phantom with three nested conductivity compartments labeled I, II and III

References:

1. Birgul O, et al., Proc. ISMRM p.331, 2006.
2. Muftuler LT, et al., TCRT 3(6): 599-609, 2004.
3. Birgul O, et al., PMB 48:653-671, 2003.
4. Pluim JP, et al., IEEE Trans. Med. Imag 19:809-814, 2000.

Acknowledgements: This research is supported in part by NIH R01 CA114210

Effects of Limited Volume Coverage on Accuracy of MR-Electrical Impedance Tomography

L. T. Muftuler¹, O. Birgul¹, M. J. Hamamura¹, and O. Nalcioglu¹

¹Tu & Yuen Center for Functional Onco-Imaging, University of California, Irvine, CA, United States

Introduction: The goal of this study was to investigate the effects of limited volume coverage on the accuracy of conductivity reconstruction in MR-Electrical Impedance Tomography (MREIT). Since the currents injected into an object will be distributed in the whole volume, limited volume coverage in data acquisition or reconstruction will impact the accuracy of resulting conductivity maps. On the other hand, the magnitude of current density will decrease rapidly as the distance from the injecting electrodes increases. Moreover, if one is interested in a particular volume of interest (VOI), the magnetic fields generated by currents away from the VOI could be negligible. Therefore, we investigated the decrease in magnitude of current density as the distance from the electrodes increases. We also investigated the contribution of these weaker currents to the magnitude of the magnetic fields generated within the VOI.

Methods: In MREIT, weak electrical currents are injected into an object that generate magnetic fields, the z-component of which induces additional phase information in MR images. A modified spin-echo sequence was used with several π pulses applied during the zero-crossings of an alternating current and a phase shift accumulates, which is given in the final image as $\phi(r) = 4\gamma N b_z(r)/\omega$ (γ : gyromagnetic ratio; N : # cycles of injected current; $b_z(r)$: the current-generated magnetic field at point r ; ω : angular frequency of the injected current). Once $b_z(r)$ is calculated from the phase $\phi(r)$ measurements, one can devise a method to calculate the conductivity map [Muftuler LT et al TCRT v 3, 599-610, 2004]. Since only the z-component of the magnetic field is used in MREIT, the transverse components of the current density, $J_x(r)$ and $J_y(r)$ are of interest. We performed several simulation studies to calculate the current density and magnetic fields inside a cylindrical volume ($d=4.5\text{cm}$ $h=7\text{cm}$) with uniform conductivity distribution. Two electrodes were placed at 135° and 315° around the central transaxial slice (slice 0). First, the electric potential distribution was determined by solving the Poisson's equation with Neumann boundary value problem (Eq.1) using Finite Element Method (FEM). Here, σ is the 3D conductivity distribution and ϕ is the electric potential. The current density and the magnetic flux density are calculated using equations 2 and 3, respectively. In 3D FEM model 13773 nodes and 73452 of tetrahedral elements were used.

Results: Fig.1a shows the magnitude of the transverse current density ($J_x(r)^2 + J_y(r)^2$)^{1/2} across 15 slices for regions labeled 13-19 in Fig.1b. $b_z(r)$ was calculated for five cases on these 15 transverse planes that were 5mm apart. For each case, the current density only within a transverse slab of various thicknesses was used for $b_z(r)$ calculations: **case1**: 4.2cm, **case2**: 3cm, **case3**: 2.4cm, **case4**: 1.8cm and **case5**: 1.2cm. Fig.2 shows the $b_z(r)$ contour maps in slice 0. Fig. 2a is the resulting magnetic field when the transverse current density in 4.2cm thick slab was used (**case1**). Similarly, Fig.2b is the $b_z(r)$ for **case5**. Fig.2c is the difference field when 2b is subtracted from 2a. When **case1** is taken as the reference, the field difference maps ($\Delta b_z(r)$) between **case1** and others give us a measure of the errors made in the calculation of $b_z(r)$ when the current density outside the selected slab is ignored. Therefore, we defined a region of interest (ROI) that encompassed the white contour band in the upper right hand corner of Fig.2c. The mean $b_z(r)$ inside the ROI for **case1** is taken as the reference and the mean of $\Delta b_z(r)$ for each case is calculated and divided by this reference mean. Results are summarized in table 1.

Discussion: The result in Fig 1a shows that the current density in the plane that is 21mm away from the electrodes has significant magnitude. (e.g. in region 19, the magnitude of the current is roughly 40% of that of slice 0). Moreover, the magnetic field in the ROI in slice 0 is underestimated by almost 30% if only currents within a 12mm slab are taken into account. This will lead to underestimation of conductivity maps in this slice. Therefore, one has to acquire MREIT data that covers sufficiently large volume to obtain accurate conductivity maps. On the other hand, reconstruction of conductivity maps from large data sets may require 18-20 hours of computing time. Therefore, optimum volume coverage has to be found to obtain a balance between acceptable accuracy and computational efficiency by carrying out simulations and experiments. The preliminary results presented here were obtained from a uniform conductivity phantom. The results from objects of nonuniform conductivity will be different and models should be developed accordingly to find the optimum volume coverage for studies such as *in vivo* experiments.

Acknowledgements: This research is supported in part by NIH R01 CA114210 and DOD W81XWH-04-1-0446 grants.

$$\nabla \cdot (\sigma \cdot \nabla \phi) = 0$$

$$\sigma \frac{\partial \phi}{\partial n} = \begin{cases} J \text{ on (+) electrode} \\ -J \text{ on (-) electrode} \\ 0 \text{ elsewhere} \end{cases} \quad (1)$$

$$\vec{E} = -\nabla \phi \quad \vec{J} = \sigma \cdot \vec{E} \quad (2)$$

$$d\vec{B} = \frac{\mu_0 I}{4\pi} \left(\frac{d\vec{l} \times \vec{R}}{R^3} \right) \quad (3)$$

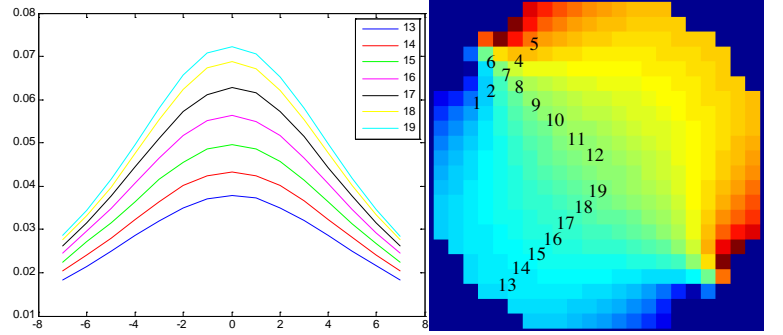


Fig.1. (a) magnitude of current density across slices in selected regions shown in the field map (b).

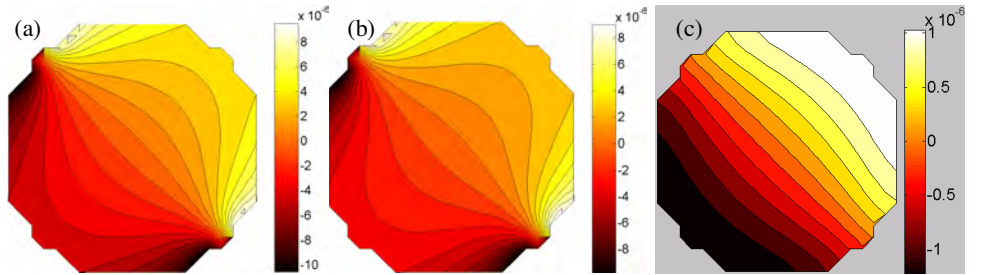


Fig.2. $b_z(r)$ contour maps for case 1 (a), case 5 (b) are illustrated. The difference of the two $b_z(r)$ maps is shown in (c). Current was injected between electrodes placed at 135° and 315° .

	case5	case4	case3	case2
$100 * \frac{\text{mean}(\Delta b_z(r))}{\text{mean}(\text{case1})}$	29	17	9	4.8

Table 1. Mean of $\Delta b_z(r)$ for each case divided by the reference mean

Reconstruction of Irregular Conductivity Distributions using MREIT at Low Current Levels

O. Birgul¹, L. T. Muftuler¹, M. J. Hamamura¹, O. Nalcioglu¹

¹Tu & Yuen Center for Functional Onco Imaging, University of California, Irvine, CA, United States

Purpose

It is possible to detect locations of lesions in breast cancer using techniques such as x-ray mammography or MRI accurately, however, the specificity of current techniques is low [1]. Since the conductivity values of malignant, benign, and normal tissues are significantly different, this information can be used in classification to improve specificity. Magnetic resonance-electrical impedance tomography (MREIT) is an imaging modality that reconstructs conductivity images from magnetic field measurements generated due to a current distribution in a volume conductor. In MREIT low amplitude sinusoidal current is injected into an object and the resulting magnetic field accumulated additional phase in MR images. A modified fast spin-echo sequence is used to measure this magnetic field. These measurements are used to solve the inverse problem of finding the conductivity distribution inside the object using an iterated sensitivity reconstruction algorithm. In most cases, the conductivity distribution is expected to vary within the tumor. There are several phantom studies in literature that assess the performance of MREIT using simple cases but none investigates whether it is capable of detecting complex and nested conductivity distributions, which models the real life cases more accurately. In this study, we used a new criterion for selection of optimum regularization parameter in image reconstruction and showed that it is possible to resolve a 6mm inhomogeneity within an irregular region using 1mA peak current.

Methods

Reconstruction of conductivity involves two basic steps. The first step is the measurement of magnetic flux density using magnetic resonance imaging. This step involves MRI data acquisition using a modified spin echo pulse sequence [2] and generation of magnetic flux density images from MRI phase images using scaling. The component of the magnetic flux density in the direction of the main static field of MRI is sufficient in image reconstruction. In the second step, these images are used as input data in the inverse problem of finding conductivity from magnetic field information. Sensitivity based reconstruction algorithm is implemented for the solution of the inverse problem. Uniform conductivity distribution is assumed and sensitivity matrix is calculated analytically [3]. Resulting matrix equation is given as $\Delta \mathbf{b} = \mathbf{S} \Delta \sigma$ where $\Delta \mathbf{b}$ is the difference between measured magnetic flux density and the magnetic flux density corresponding to initial distribution, $\Delta \sigma$ is the change with respect to initial and \mathbf{S} is the sensitivity matrix that gives the relation between changes in magnetic field and conductivity. Including Tikhonov regularization parameter, λ , the matrix equation becomes $(\mathbf{S}^T \mathbf{S} + \lambda \mathbf{I}) \Delta \sigma = \mathbf{S}^T \Delta \mathbf{b}$ where \mathbf{I} is the identity matrix. The matrix equation is solved for different values of λ using conjugate gradient method and the optimum regularization value is selected as the one minimizing the difference

$$\min_{\lambda} \sum_{i=1}^m \|B_{meas,i} - B_{calc,i}(\lambda)\|$$

where m is the total number of measurement points, B_{meas} is the measured magnetic flux density, and B_{calc} is the flux density calculated using reconstructed conductivity. Calculated conductivity distribution is assigned as the initial value and the steps starting with sensitivity matrix calculation are repeated until the change in conductivity two consecutive iterations are below a defined threshold.

Results

A three region conductivity phantom is generated using agarose and different concentrations of NaCl (Fig 1a). For the background, 1% (g/100mL) agarose and 1% NaCl is used. Agarose amount is kept constant in all regions but NaCl is increased to 2% and 4% for regions II and III respectively. Corresponding conductivity values are measured using a 4 electrode conductivity cell and the true values are found to be 1.54, 2.94, and 5.92mS/cm. Four electrodes are placed around the object giving 6 different current injection profiles. First, high-resolution anatomical images are acquired to determine the exact locations of the electrodes to be used in the image reconstruction (Fig 1b). Since the water content is same in all regions, the irregular region and the 6mm inclusion cannot be seen in the MR image. Then 4 cycles of 1mA (peak) 100Hz current were injected with TR = 1000ms, TE = 50ms, and NEX = 4 and field is measured for 6 cases (Fig 1c). Measurements around the outer ring are masked out to eliminate spurious boundary effects in images reconstruction. Reconstructed conductivity image is given in Fig 1d, where the 6mm region inside the irregular image is resolved. Peak reconstructed values for each region are 1.23, 2.55, and 4.93mS/cm for each region.

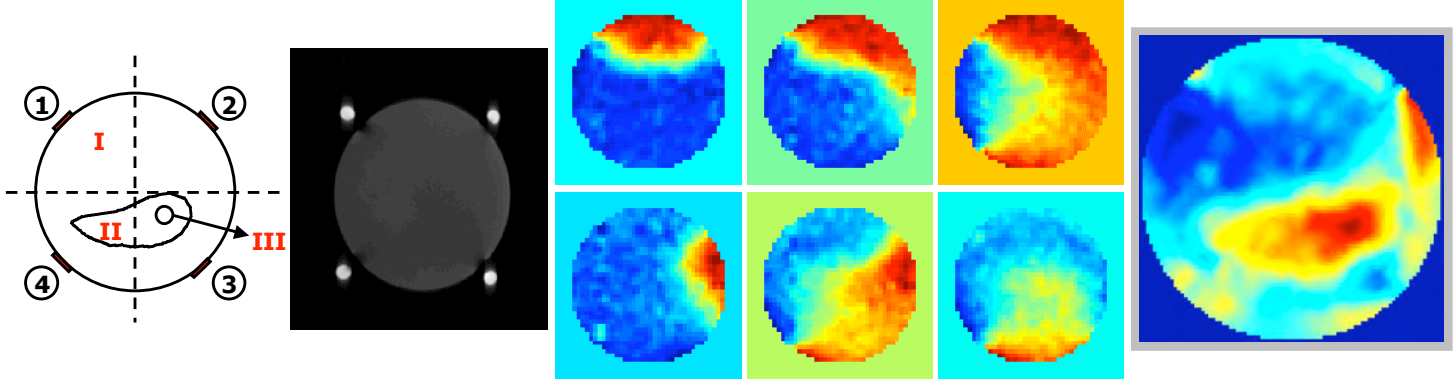


Figure 1a

Figure 1b

Figure 1c

Figure 1d

Figure 1 (a) Schematic of the multi-compartment conductivity phantom (b) MR magnitude images (c) Scaled and masked MR phase images for 6 different current injection case (d) reconstructed conductivity image (red indicating higher conductivity and blue indicating lower conductivity)

Discussion

In this study, we have shown that it is possible to reconstruct complex conductivity distributions within an object using MREIT technique and iterated sensitivity reconstruction algorithm. The irregular object and 6mm inclusion, which cannot be seen in the anatomical MR images, are clearly resolved in the conductivity image with 16.7% peak error at current levels which are acceptable for human imaging applications.

References

[1] Malich A, et. al., *Eur. Radiol*, 10: 1555-1561 (2000), [2] Muftuler L T, et. al., *TCRT* December 2004 [3] Birgul O, et. al. *PMB*, 48: 3485-2504 (2003)

Acknowledgments

This research is supported in part by Department of Defense Award W81XWH-04-1-0446 and NIH/NCI Award R01 CA114210.

Dynamic MREIT Using Sub-Milliamp Currents

M. J. Hamamura¹, L. T. Muftuler¹, O. Birgul¹, O. Nalcioğlu¹

¹Tu & Yuen Center for Functional Onco-Imaging, University of California, Irvine, CA, United States

Purpose

In Magnetic Resonance Electrical Impedance Tomography (MREIT), electrical currents are injected into an object and the resulting magnetic flux density distribution measured using MRI. These MRI measurements are then used to reconstruct the conductivity distribution within the object. Previous MREIT studies have focused primarily on reconstructing static conductivity distributions. However, the ability to detect changes in conductivity over time could provide additional diagnostic information. We previously reported on the qualitative monitoring of ion diffusion in agarose gel over four time points using MREIT with 10mA injected currents. In this study, we perform a more thorough monitoring using sub-milliamp injected currents more appropriate for human use.

Methods

For the test phantom, a hollow acrylic disk with an inner diameter of 7cm and thickness of 1cm was filled with 2% agarose and 4mM CuSO₄. Within this disk, a smaller circular region of 12mm diameter was filled with 2% agarose, 1% NaCl, and 4mM CuSO₄ (Figure 2a). Over time, the NaCl diffused from the smaller region into the background, and the conductivity distribution changed. A linear relationship between conductivity and NaCl concentration (of 1% or less) was found after performing a range of conductivity measurements using the 4-electrode technique. The plane of the disk was placed perpendicular to the main static MRI field. Four copper electrodes each 6mm wide were placed equidistantly along the inner acrylic wall and used to inject currents into the interior region.

A finite alternating current pulse waveform with an amplitude of 900uA was injected into the phantom and the resulting magnetic flux density distribution measured using a modified spin-echo pulse sequence (Figure 2) [Mikac et al, MRI 19: 845-856 (2001)]. The scan parameters were TR=500ms, TE=60ms, NEX=4, Matrix=64X64, FOV=10cm, and single slice thickness = 5mm. Data was collected for two different current injection schemes (in pairs of electrodes directly opposite of each other) and used simultaneously in conductivity reconstruction. To reconstruct the conductivity distribution using the MRI measurements, the Sensitivity Matrix Method was utilized [Birgul et al, Phys Med Bio 48: 3485-3504 (2003)] in which the relationship between conductivity and magnetic flux density is linearized around an initial conductivity (i.e. uniform distribution) and formulated as a matrix equation. This equation is then solved for the true conductivity distribution using Tikhonov regularization. The resulting conductivity can then be substituted back into the linearized equation as the new, updated initial condition, and the process iterated to improve the reconstruction.

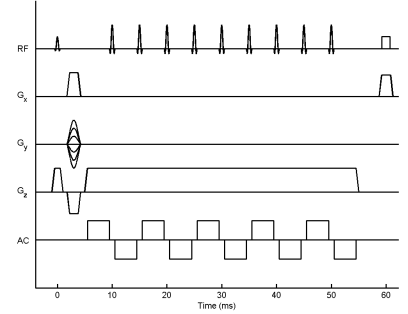


Figure 1. Pulse sequence used in MREIT

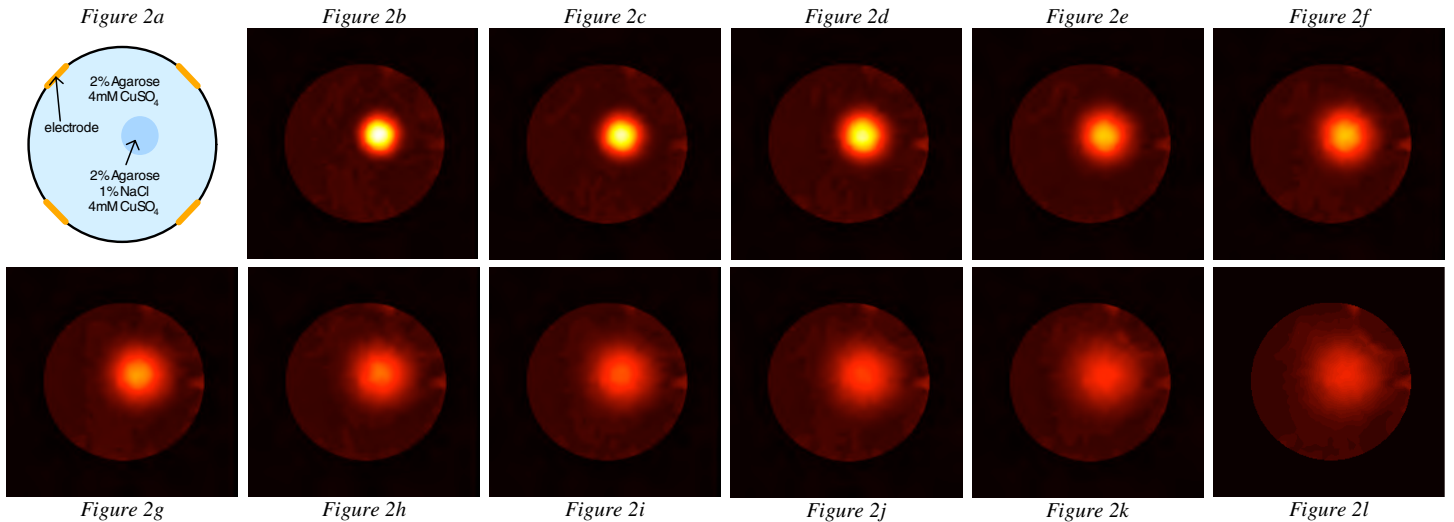


Figure 2. (a) Schematic of the phantom; (b) Conductivity after 20 minutes; (c) 1 hour; (d) 2 hours; (e) 3 hours; (f) 4 hours; (g) 5 hours; (h) 6 hours; (i) 7 hours; (j) 8 hours; (k) 10 hours; (l) 12 hours

Results

Data was collected at various time points, and the conductivity distributions reconstructed (Figures 2b-l). The resulting images clearly show a change in the conductivity distribution consistent with the diffusion of NaCl from the higher concentration region to the lower concentration region. For a disk of radius a on an infinite plane surface, the theoretical concentration C at the center of the disk is given as $C = C_0(1 - \exp(-a^2/4Dt))$. The peak conductivity values were fitted to this equation, and an experimental diffusion constant of $D = 5.8 \times 10^{-6} \text{ cm}^2 \text{ sec}^{-1}$ obtained (Figure 3). This value is smaller than the previously reported measurement of $1.4 \times 10^{-5} \text{ cm}^2 \text{ sec}^{-1}$ [Schantz et al, Biochem J: 658-663 (1962)]. The slower apparent diffusion in this phantom can in part be attributed to its finite shape and confined volume.

Discussion

The results of this study demonstrate that MREIT can monitor changes in conductivity over time using sub-milliamp injected currents. Validating this ability is a necessary step towards the imaging and monitoring of *in vivo* subjects using MREIT.

Acknowledgement

This research is supported in part by NIH/NCI R01 CA114210, DOD DAMD17-02-1-0326, and DOD W81XWH-04-1-0446a.

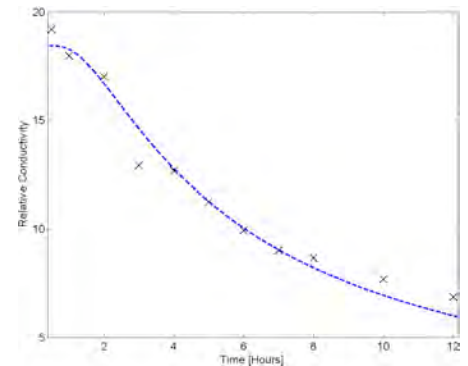


Figure 3. Peak conductivity values

Electrode Misalignment Correction Algorithms In Magnetic Resonance Electrical Impedance Tomography

M. J. Hamamura¹, L. T. Muftuler¹, O. Birgul¹, O. Nalciglu¹

¹Tu & Yuen Center for Functional Onco-Imaging, University of California, Irvine, CA, United States

Purpose

In Magnetic Resonance Electrical Impedance Tomography (MREIT) electrical currents are injected into an object and the resulting magnetic flux density distribution measured using MRI. These MRI measurements are then used to reconstruct the conductivity distribution within the object. Many of the reported MREIT reconstruction algorithms utilize numerical calculation of the magnetic flux density for a given conductivity distribution using the boundary conditions applied to the real object. This corresponds to matching the position of the electrodes in the numerical computation to that of the actual position of the electrodes on the object. Near an injecting electrode, there exists a large variation in the magnetic flux density. As a result, any misalignment in the position of an electrode can result in significant errors when calculating the difference between the computed magnetic flux density distribution and the MRI-measured magnetic flux density distribution. Such errors may generate artifacts in the final reconstructed conductivity distribution. In this study, we investigate various correction algorithms to reduce these artifacts.

Method

For the test phantom, a hollow acrylic disk with an inner diameter of 7cm and thickness of 1cm was filled with 2% agarose, 0.1% NaCl, and 4mM CuSO₄. Within this disk, a smaller circular region of 12mm diameter was filled with 2% agarose, 1% NaCl, and 4mM CuSO₄ (Figure 1). The conductivities of the different regions were measured using the 4-electrode method and found to yield a contrast ratio of 1 to 7.4. The plane of the disk was placed perpendicular to the main static MRI field. Four copper electrodes each 6mm wide were placed equidistant along the inner acrylic wall and used to inject currents into the interior region.

A finite alternating current pulse waveform with an amplitude of 900uA was injected into the phantom and the resulting magnetic flux density distribution measured using a modified spin-echo pulse sequence (Figure 2) [Mikac et al, MRI 19: 845-856 (2001)]. The scan parameters were TR=500ms, TE=60ms, NEX=4, Matrix=64X64, FOV=10cm, and single slice thickness = 5mm. Data was

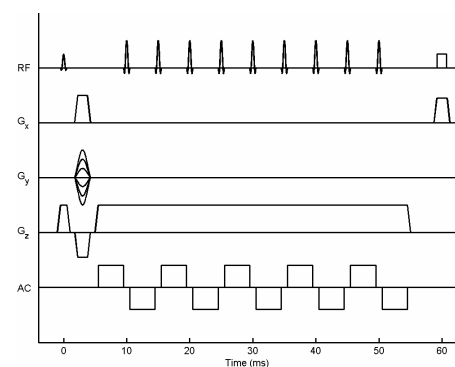


Figure 2. Pulse sequence used in MREIT

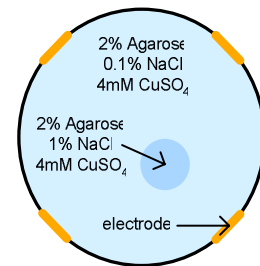


Figure 1. Schematic of the phantom

collected for two different current injection schemes (in pairs of electrodes directly opposite of each other) and used simultaneously in conductivity reconstruction. To reconstruct the conductivity distribution using the MRI measurements, the Sensitivity Matrix Method was utilized [Birgul et al, Phys Med Bio 48: 3485-3504 (2003)] in which the relationship between conductivity and magnetic flux density is linearized around an initial conductivity (i.e. uniform distribution) and formulated as a matrix equation. This equation is then solved for the true conductivity distribution using Tikhonov regularization. The resulting conductivity can then be substituted back into the linearized equation as the new, updated initial condition, and the process iterated to improve the reconstruction.

Three different electrode misalignment correction algorithms can be implemented during reconstruction. For the first algorithm (MASK), magnetic flux density measurements within 1cm of the electrodes were discarded and not used during reconstruction. For the second algorithm (SHIFT), the position of each electrode assigned during numerical computation was perturbed to find the best location. The difference between the MRI-measured magnetic flux density and the calculated magnetic flux density given the initial condition was minimized as a function of electrode position. For the third algorithm (REG), conductivity perturbations within 1cm of the electrodes were suppressed by a factor of 2 when compared to the rest of the phantom through increased weighting in the Tikhonov regularization.

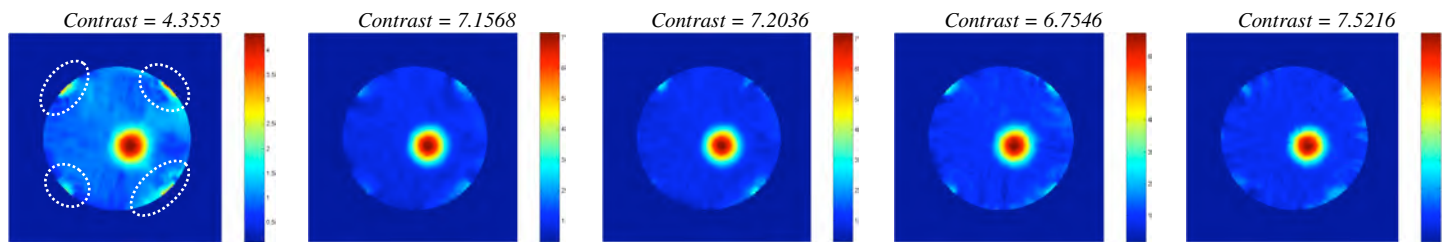


Figure 3a

Figure 3b

Figure 3c

Figure 3d

Figure 3e

Figure 3. (a) Reconstructed conductivity distribution using no correction; (b) MASK; (c) SHIFT; (d) REG; (e) all 3 algorithms

Results

Data was collected using a 4T MRI system. Conductivity distributions were reconstructed for various combinations of electrode correction algorithms using 5 iterations of the Sensitivity Matrix Method (Figures 3a-e). For each reconstructed image, the contrast between the high and low conductivity regions was calculated by finding the maximum conductivity value and dividing it by the mean conductivity of the background. The background conductivity was calculated by finding the average conductivity of the phantom excluding a 2cm diameter disk centered on the high conductivity region.

Discussion

The results of this study indicate that electrode misalignment affects the reconstructed conductivity distribution throughout the phantom. Regions next to the electrodes contain artifacts as circled in Figure 3a, while objects in the interior region suffer from diminished contrast. Each of the proposed correction algorithms improves the reconstruction, with the best result occurring when all three methods are applied.

Acknowledgement

This research is supported in part by NIH/NCI R01 CA114210, DOD DAMD17-02-1-0326, and DOD W81XWH-04-1-0446a.

Multiple Current Injection Schemes In Magnetic Resonance Electrical Impedance Tomography

M. J. Hamamura¹, L. T. Muftuler¹, O. Birgul¹, O. Nalcioğlu¹

¹Tu & Yuen Center for Functional Onco-Imaging, University of California, Irvine, CA, United States

Purpose

In Magnetic Resonance Electrical Impedance Tomography (MREIT) electrical currents are injected into an object and the resulting magnetic flux density distribution measured using MRI. These MRI measurements are then used to reconstruct the conductivity distribution within the object. In order to determine the conductivity distribution uniquely, data from at least two different current distributions satisfying $\|J_1(x,y)\| \neq 0$ must be acquired [Kwon O. *et al*, *IEEE Trans on BME* 49: 160-167 (2002)]. Typically, two electrodes are used to provide one current distribution, and two additional electrodes are used to provide a second current distribution, for a total of four electrodes and two current injection schemes. However, with four electrodes, one can apply up to six different current injection schemes using different pairs of electrodes (Figure 1). In this study, we assess the effects of utilizing these additional current injection schemes.

Method

For the test phantom, a hollow acrylic disk with an inner diameter of 7cm and thickness of 1cm was filled with 2% agarose, 0.1% NaCl, and 4mM CuSO₄. Within this disk, a three smaller circular regions each 1cm in diameter were filled with 2% agarose, 1% NaCl, and 4mM CuSO₄ (Figure 3). The conductivities of the different regions were measured using the 4-electrode method and found to yield a contrast ratio of 1 to 7.4. The plane of the disk was placed perpendicular to the main static MRI field. Four copper electrodes each 6mm wide were placed equidistant along the inner acrylic wall and used to inject currents into the interior region.

A finite alternating current pulse waveform with an amplitude of 900uA was injected into the phantom and the resulting magnetic flux density distribution measured using a modified spin-echo pulse sequence (Figure 2) [Mikac *et al*, *MRI* 19: 845-856 (2001)]. The scan parameters were TR=500ms, TE=60ms, NEX=4, Matrix=64X64, FOV=10cm, and single slice thickness = 5mm. To reconstruct the conductivity distribution using the MRI measurements, the Sensitivity Matrix Method was utilized [Birgul *et al*, *Phys Med Bio* 48: 3485-3504 (2003)] in which the relationship between conductivity and magnetic flux density is linearized around an initial conductivity (i.e. uniform distribution) and formulated as a matrix equation. A separate equation is generated for each current injection scheme, and various combinations of these equations can be combined to solve for the conductivity distribution. The solution is obtained using Tikhonov regularization. The resulting conductivity can then be substituted back into the linearized equation(s) as the new, updated initial condition, and the process iterated to improve the reconstruction.

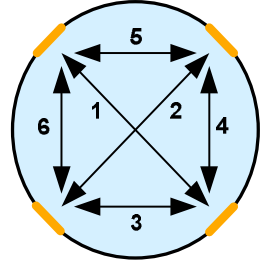


Figure 1. Multiple Current Injection Schemes

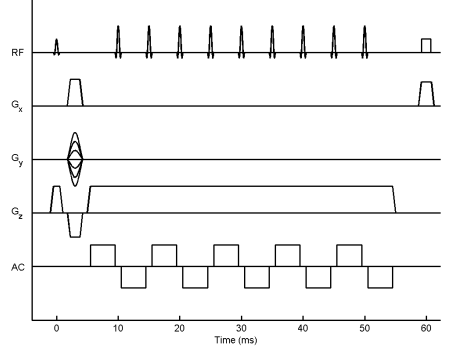


Figure 2. Pulse sequence used in MREIT

Results

Data was collected for each of the 6 current injection schemes. Conductivity distributions were reconstructed for different combinations of data sets using 5 iterations of the Sensitivity Matrix Method (Figures 4a-c). For each reconstructed image, the peak conductivity in each of the three inner regions A, B, and C was found (relative to the background conductivity of 1), and the results compiled in Table 1. A closer view of region C was also extracted (Figures 5a-c).

Discussion

The results indicate that reconstructing periphery regions away from the injecting electrodes presents difficulties, regardless of the current injection schemes used. From inspection of Figure 5, including data from the periphery injection schemes (3-6 in Figure 1) improves the overall shape of object C. In particular, adding scheme 3 provides the largest current density to the region of interest and appears to best improve the spatial distribution. However, overall contrast is best when using only the standard orthogonal injection schemes (1 and 2). Using additional injection schemes further reduces contrast throughout the object.

Selecting which current injection schemes to use requires balancing overall contrast with improved spatial resolution in the periphery regions, and will thus depend on the object to be imaged and the desired information. The increased scan time required to collect data from addition current injection schemes must also be considered.

Acknowledgement

This research is supported in part by NIH/NCI R01 CA114210, DOD DAMD17-02-1-0326, and DOD W81XWH-04-1-0446a.

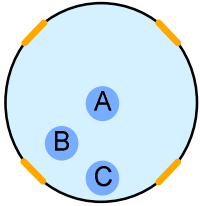


Figure 2. Schematic of phantom

Schemes	1,2	1,2,3	1-6
Region A	6.3398	5.6022	5.2355
Region B	6.3299	5.7407	5.3522
Region C	3.6669	3.6327	3.6439

Table 1. Peak conductivities

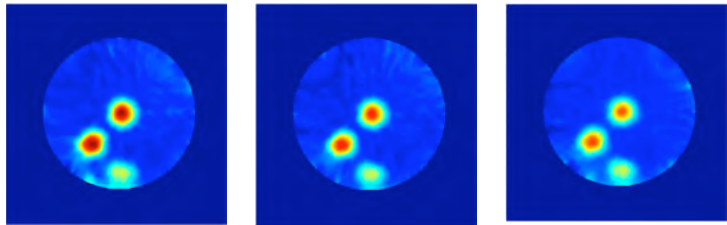


Figure 4. Reconstructed conductivity using injection schemes: (a) 1,2; (b) 1,2,3; (c) 1-6

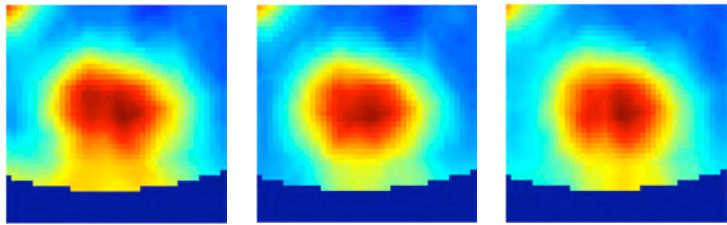


Figure 5. Conductivity of Region C for injection schemes: (a) 1,2; (b) 1,2,3; (c) 1-6

In Vivo MRI Based Electrical Impedance Tomography of Malignant Tumors

L. T. Muftuler¹, M. Hamamura¹, O. Birgul¹, O. Nalcioğlu¹

¹John Tu & Thomas Yuen Center for Functional Onco-Imaging, University of California, Irvine, CA, United States

Purpose

Several studies have shown that the electrical impedance of malignant tissues is significantly different from those of normal and benign tissues [1,2]. Therefore, in-vivo impedance imaging of suspicious lesions has the potential to improve the sensitivity and specificity of detecting malignant tumors. MR-Electrical Impedance Tomography (MREIT) has been recently introduced, in which weak electrical currents are injected into the tissue and the resulting perturbations in magnetic field were measured using phase information in MR images. We have reported our preliminary studies with phantoms as well as two *in vivo* experiments [3]. Here, we present the results of MREIT done on eleven animals. Parameters like variance and mean in the tumor versus the rest of the body were investigated. The goal is to verify potential of MR-EIT to aid in the diagnosis of tumors.

Methods

Weak electrical currents that are injected into an object generate magnetic fields, the z-component of which induces additional phase information in MR images. If a modified spin-echo sequence was used with several π pulses applied during the zero-crossings of the alternating current, the phase shift accumulates across these π pulses and is given in the final image as $\phi(\mathbf{r}) = 4 \cdot \gamma \cdot N \cdot b_z(\mathbf{r}) / \omega$, (γ : gyromagnetic ratio; N : the number of cycles of injected current; $b_z(\mathbf{r})$: the amplitude of current-generated magnetic field at point \mathbf{r} ; ω : angular frequency of the injected current). Here $b_z(\mathbf{r})$ is calculated from the phase $\phi(\mathbf{r})$ measurements. We have implemented an iterative reconstruction with Tikhonov regularization to reconstruct the conductivity images from $b_z(\mathbf{r})$: $\mathbf{S}^T \Delta \mathbf{b}_z(\mathbf{r}) = (\mathbf{S}^T \mathbf{S} + \lambda \mathbf{I}) \Delta \sigma(\mathbf{r}')$. Here the *sensitivity matrix* \mathbf{S} is calculated using Finite Element Method; $\Delta \mathbf{b}_z(\mathbf{r})$ is the change in magnetic field at point \mathbf{r} for a given current injection scheme resulting from a change $\Delta \sigma(\mathbf{r}')$ in the conductivity at point \mathbf{r}' , λ is the *regularization parameter* and \mathbf{I} is the identity matrix. The details were given in [4].

Data were collected in a whole body 4T MRI system with a MRRS console. Eleven rats were imaged, ten of which were bearing malignant tumors that were either R3230AC tumor grafts or induced by the carcinogen ENU. Animals were anesthetized prior to imaging and all procedures were approved by the IACUC. Two data sets were discarded due to severe motion artifacts. Structural images were collected using T2 weighted SE sequence prior to MREIT images. The data matrix was 128X128, FOV = 10cm, slice thickness = 4mm, with 2mm gap. TR = 3s, TE = 50ms and NEX = 2 were used. MREIT images were collected using the outlined pulse sequence with TR=1000ms, TE=30ms, and NEX=2, 64X64 data matrix, FOV = 10cm, slice thickness = 4mm with 2mm gap. Two cycles of 100Hz current with 1mA rms was applied sequentially through different pairs of four electrodes, generating six different current profiles. Data were collected with both \pm polarities of the currents to eliminate phase accumulation from other sources.

Results and Discussion

Fig.1 shows T2 weighted MRI and MREIT images of two rats. Tumor areas show increased conductivity depicted with yellow-red colors. On the MREIT images of the animals, separate ROIs (region of interest) were drawn over the tumor region and the rest of the body and the mean conductivity values in these ROIs were calculated. Since MREIT yields relative conductivity values, the conductivity ratio $\sigma_{\text{tumor}}/\sigma_{\text{body}}$ was calculated for each animal and the graph is shown in Fig.2. It was found that the average of these conductivity ratios was 2.17. ROIs were drawn manually based on the tumor seen in MRI T2 images. We have also calculated the ratio of standard deviation to mean conductivity in each tumor region, which may be an indication of *conductivity heterogeneity* inside the tumor volume, rather than SNR (Fig.3). As seen from these figures, consistent results were obtained from these eight animals. Average conductivity increased by roughly 2.2 times in the tumor compared to the rest of the body. The conductivity varied typically between 10% and 20% within the tumor. In two of the rats, we have also collected MRIET data with rms currents of 0.5, 1 and 2mA. Highly consistent results were seen especially between 1 and 2mA cases. For example, when MREIT images of 1mA and 2mA cases were subtracted, the mean of the residual was only 1.3% of the mean conductivity in the whole slice. In the case of 0.5mA vs 1mA, the mean of the residual was 12%.

In this study, it has been demonstrated that MRI based impedance imaging has the potential to investigate malignant tumors *in vivo*. At this stage the technique may not be used as a standalone diagnostic tool; but it could provide useful information in characterizing the tumor, once a suspicious lesion is detected by other methods to improve specificity. Physiological and structural changes in tumors that lead to such changes in conductivity will be investigated in future studies. Note that good quality MREIT images were collected with biologically safe electrical current levels.

References: [1] Malich A. *et al*, *Clinical Radiology*,56:278-283, 2001; [2] Silva J.E.D *et al*.*Med. Biol. Eng. and Comp.*, 38:26-30, 2000; [3] Muftuler LT *et al* *TCRT v 3* (2), 599-610, (2004); [4] Muftuler LT *et al* *Proceedings of ISMRM* 2005, p 2356.

Acknowledgements: This research was supported in part by grants NIH R01 CA114210 and DOD DAMD17-02-1-0326

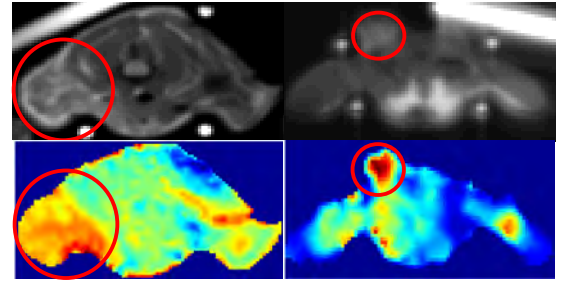


Fig.1. Results from two animals are illustrated. T2 weighted scans are displayed above and corresponding impedance (MREIT) images are depicted in color right below. Tumor areas are marked with red circles.

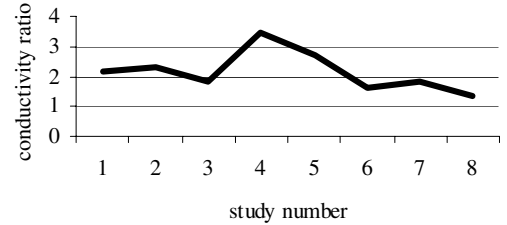


Fig.2. The ratio of mean conductivity in the tumor versus the rest of the body over eight *in vivo* studies.

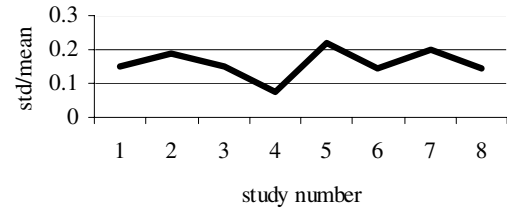


Fig.3. The ratio of standard deviation of conductivity versus its mean in the tumor in eight *in vivo* studies.

MRI Based Electrical Impedance Imaging of Tumors with Iterated Sensitivity Reconstruction Using Regularization

L. T. Muftuler¹, M. J. Hamamura¹, O. Birgul¹, O. Nalcioğlu¹

¹Tu & Yuen Center for Functional Onco-Imaging, University of California, Irvine, CA, United States

Purpose

Several researchers have demonstrated that the electrical properties, specifically the impedance of malignant tissues is significantly different from those of normal and benign tissues [Malich *et al. Clin.Rad.*,56:278-283, 2001; Silva *et al. Med. Biol. Eng. and Comp.*, 38:26-30, 2000]. Therefore, *in vivo* impedance imaging of suspicious lesions could aid in improving the sensitivity and specificity of detecting malignant tumors. MRI based impedance imaging is a novel method, in which weak electrical currents are injected into the tissue and the resulting perturbations in magnetic field were measured using phase information in MR images. We have reported our preliminary studies with phantoms as well as some *in vivo* experiments. However, in those studies, reconstruction was done with the non-iterative sensitivity matrix approach, which assumed a linear relationship between the measured field perturbations and relative conductivity distribution. For large conductivity variations, this linearity assumption failed and the resulting images underestimated the conductivity variations. This resulted in poorer spatial specificity and sensitivity. We refined our reconstruction technique with an iterative approach to account for the nonlinearities. The goal is to verify potential of MR-EIT to aid in the diagnosis of tumors.

Methods

When a sinusoidal current is injected into an object, the z-component of the resulting magnetic fields induce additional phase information in MR images. A modified spin-echo sequence was used, where several π pulses were applied during the zero-crossings of the sinusoidal current (Fig.1) [Mikac *et al. MRI* 19: 845 856 (2001)]. This phase shift accumulates across these π pulses and is given in the final image as $\phi(\mathbf{r}) = 4 \cdot \gamma \cdot N \cdot b_z(\mathbf{r}) / \omega$, where γ is the gyromagnetic ratio, N the number of cycles of injected current, $b_z(\mathbf{r})$ the amplitude of z-component of current-generated magnetic field at point \mathbf{r} , and ω the angular frequency of the injected current. Therefore, once the phase, $\phi(\mathbf{r})$ is measured, $b_z(\mathbf{r})$ can be calculated. In the original approach, a linear approximation $\Delta B(\mathbf{r}) = S(\mathbf{r}, \mathbf{r}') \Delta \sigma(\mathbf{r}')$ was assumed to reconstruct conductivity image. Here $\Delta B(\mathbf{r})$ is the change in magnetic field at point \mathbf{r} for a given current injection scheme resulting from a change $\Delta \sigma(\mathbf{r}')$ in the conductivity at point \mathbf{r}' . S is calculated using Finite Element Method (FEM). Recently, we have adopted an iterative reconstruction with Tikhonov regularization, which improved the accuracy as well as spatial specificity of the MREIT images. Details of this method and its assessment with phantom studies were presented in another manuscript that is being submitted concurrently. In summary, the matrix equation was modified with the addition of a regularization parameter, λ , and became $(S^T \Delta B = (S^T S + \lambda I) \Delta \sigma)$, where I is the identity matrix. This equation was solved for different values of λ using conjugate gradient method and the optimum value of λ was found. The conductivity distribution that is calculated after each iteration was assigned as the initial value for the next iteration and the iterations are repeated until the difference between the results of two consecutive iterations are below a predefined threshold. Current was injected from four electrodes placed across the animal's body and six different current distributions were generated by using different combinations of electrode pairs. This scheme also improved the uniformity and sensitivity of the MREIT images.

Results

Data were collected in a whole body 4T MRI system with a MRRS console. Two rats were imaged, which were bearing malignant tumors induced by the carcinogen ENU. Animals were anesthetized prior to imaging. All procedures were approved by the IACUC. Structural images were collected using SE sequence prior to MREIT images. The data matrix was 128X128, FOV = 10cm, slice thickness = 4mm, with 2mm gap. TR = 3s, TE = 50ms and NEX = 2 were used. MREIT images were collected using the previously outlined pulse sequence with TR=500ms, TE=30ms, and NEX=12, 64X64 data matrix, FOV = 10cm, slice thickness = 4mm with 2mm gap. 2 cycles of 100Hz current with 2mA rms was applied through different pairs of four electrodes. The resulting images clearly show the higher conductivity regions. Especially in animal-1, higher conductivity map of the tumor precisely overlaps with the one seen in the structural image. The mean conductivity in the tumor region was 2.8 times higher than the mean conductivity in the rest of the body for animal-1.

Discussion

In this study, it has been demonstrated that MRI based impedance imaging has the potential to investigate malignant tumors *in vivo*. Improvements in current injection and utilization of iterative reconstruction with regularization significantly improved the accuracy and spatial specificity of MREIT. In our experiments it was also observed that precise localization of electrode placement was critical to define boundary conditions accurately, which in turn affected the quality of MREIT images. In the presented study, 2D FEM formulation was used. Currently 3D FEM is being developed to improve the accuracy of MREIT images further.

Acknowledgements:

This research is supported by Department of Defense DAMD17-02-1-0326.

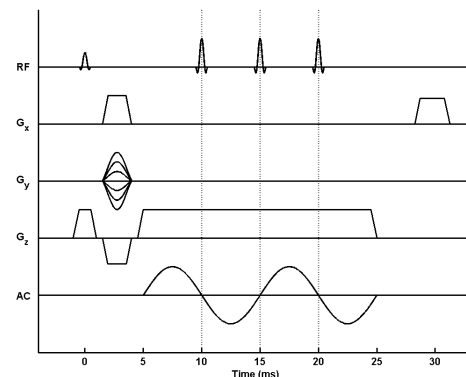


Fig. 1. Pulse sequence used in MR-EIT

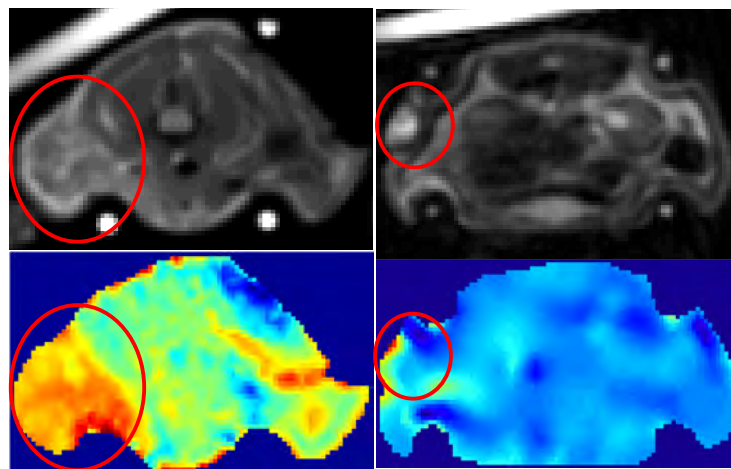


Fig.2. Structural (top) and MREIT (bottom) images of two animals. Left and right columns show the images of animal-1 and animal-2, respectively. Tumor areas are circled with red lines. Bright objects outside the animals were markers to identify exact location of electrodes.

Tracking of Sodium Diffusion in Agarose Using MR-EIT

M. J. Hamamura¹, L. T. Muftuler¹, O. Birgul¹, O. Nalcioğlu¹

¹Tu & Yuen Center for Functional Onco-Imaging, University of California, Irvine, CA, United States

Purpose

It has been reported that the electrical impedance of malignancies is 20-40 times lower than healthy tissues and benign formations [Malich A. *et al*, *Eur. Radiol.* 10: 1555-1561 (2000)]. Therefore, *in vivo* impedance imaging of suspicious lesions could aid in the diagnosis of malignant tumors. In MR-EIT, electrical currents are injected into an object and the resulting magnetic field perturbations are measured using MRI. These measurements are then used to reconstruct the conductivity distribution within the object. Previous studies on MR-EIT have focused on reconstructing static conductivity distributions. However, the ability to detect changes in conductivity over time could provide additional diagnostic information, such as in monitoring tumor growth. In this study, we assess the ability of MR-EIT to detect these changes.

Methods

Sinusoidal current is injected into an object and the resulting magnetic fields are measured using a modified spin-echo sequence (Figure 1) [Mikac U. *et al*, *MRI* 19: 845-856 (2001)]. The component of current-generated magnetic field parallel to the main static field (z-component) introduces a phase shift. By synchronizing successive π pulses to half cycles of the current, this phase shift accumulates and is given in the final image as $\phi(\mathbf{r}) = 4\gamma N b(\mathbf{r}) / \omega$, where γ is the gyromagnetic ratio, N the number of cycles of injected current, $b(\mathbf{r})$ the amplitude of z-component current-generated magnetic field at point \mathbf{r} , and ω the angular frequency of the injected current. Hence, measurement of this phase shift allows for calculation of the (z-component) magnetic field distribution.

To reconstruct the conductivity distribution from the magnetic field distribution, a linear approximation $\Delta B(\mathbf{r}) = S(\mathbf{r}, \mathbf{r}') \Delta \sigma(\mathbf{r}')$ is assumed, where $\Delta B(\mathbf{r})$ is the change in magnetic field at point \mathbf{r} for a given current injection scheme resulting from a change $\Delta \sigma(\mathbf{r}')$ in the conductivity at point \mathbf{r}' . The matrix component S_{ij} is the change in magnetic field ∂B_i of element i with respect to a change in the conductivity $\partial \sigma_j$ of element j . An initial conductivity distribution σ_{initial} is assumed (e.g. uniform conductivity), the conductivity of a given element j perturbed by $\Delta \sigma_j$, the resulting ΔB calculated using the Finite Element Method (FEM), and the matrix components approximated as $S_{ij} = \Delta B_i / \Delta \sigma_j$. The linear approximation can be rewritten as $(\mathbf{B}_{\text{final}} - \mathbf{B}_{\text{initial}}) = \mathbf{S} (\sigma_{\text{final}} - \sigma_{\text{initial}})$, where σ_{initial} is the assumed initial (uniform) conductivity distribution, $\mathbf{B}_{\text{initial}}$ the FEM calculated magnetic field distribution given σ_{initial} , $\mathbf{B}_{\text{final}}$ the MRI measured magnetic field distribution, and σ_{final} the actual conductivity distribution. The equation is solved for σ_{final} using Tikhonov regularization. This σ_{final} then substituted back into the linear approximation as the new, updated σ_{initial} , and the process is iterated until the change in conductivity between successive iterations is below some predefined threshold. Details of this reconstruction method can be found in another abstract submitted concurrently.

The previously outlined method was used to measure the conductivity distribution of an agarose gel phantom. For the phantom, a hollow acrylic disk with an inner diameter of 7cm and thickness of 1cm was filled with 1% (g/100mL) agarose and 1% NaCl. Within this disk, a smaller circular region of 12mm diameter was filled with 1% agarose and 20% NaCl (Figure 2a). Over time, NaCl diffused from the region of higher concentration to the region of lower concentration. Conductivity is assumed proportional to NaCl concentration, hence the conductivity distribution changed as a result of this diffusion. The plane of the disk was placed perpendicular to the z-axis. Four recessed electrodes each 3mm wide were placed equidistant along the circular acrylic wall and used to inject currents into the interior region. Data was collected for two different current injection schemes (in pairs of electrodes directly opposite of each other) and used simultaneously in conductivity reconstruction.

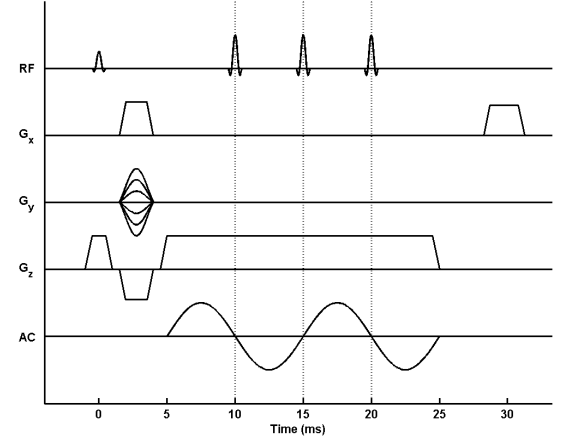


Figure 1. Pulse sequence used in MR-EIT

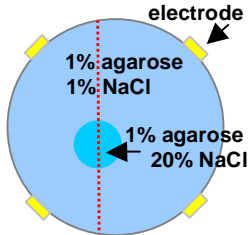


Figure 2a

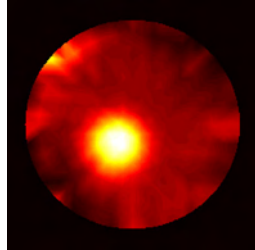


Figure 2b

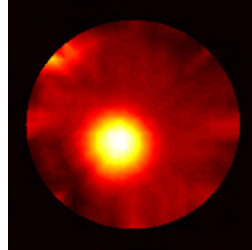


Figure 2c

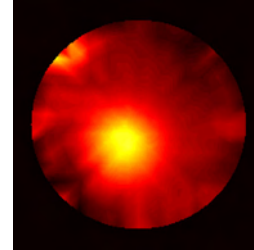


Figure 2d

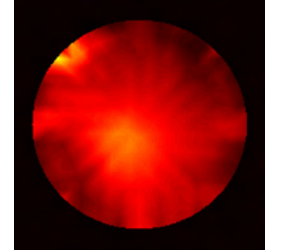


Figure 2e

Figure 2. (a) Schematic of the phantom; (b) Conductivity after 20 minutes; (c) 1 hour; (d) 6 hours; (e) 24 hours

Results

2 cycles of 10mA (rms) 100Hz current were injected into the phantom using the previously outlined pulse sequence with the parameters $TR=500\text{ms}$, $TE=30\text{ms}$, and $NEX = 4$. Scans were taken 20 minutes, 1 hour, 6 hours, and 24 hours after the creation of the phantom. The z-component current-generated magnetic field distributions were calculated from the resulting data and the conductivity distributions computed (Figures 2d-e). The resulting images clearly show a change in the conductivity distribution consistent with the diffusion of NaCl from the higher concentration region to the lower concentration region. Over time, the higher conductivity region broadens, and the border between the initial regions becomes less distinct (Figure 3).

Discussion

In this study, we have shown that MR-EIT can be used to monitor changes in conductivity over time. While we assume that conductivity is directly proportional to NaCl concentration for this phantom, future studies will verify this by correlating this method with Sodium MRI. We also plan to monitor malignancies in live animals by performing MR-EIT measurements over the span of several weeks.

Acknowledgement

This research is supported by the Department of Defense DAMD17-02-1-0326.

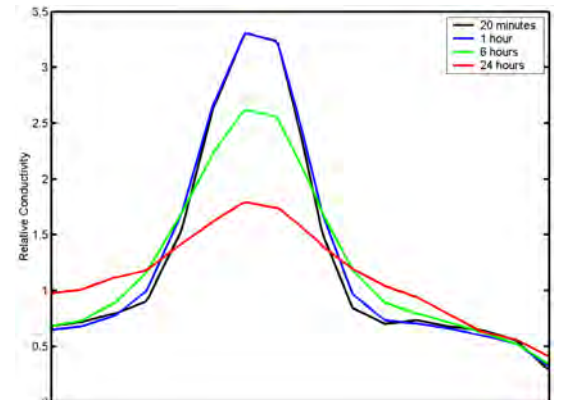


Figure 3. Profile taken across the dotted red line of Figure 2a